Fall 12-2020

Measurement of Pion-Pion Final State Interactions in $\eta \to \pi^+\pi^-\gamma$ with CLAS at Jefferson Lab

Torri C. Jeske
Old Dominion University, torricjeske@gmail.com

Recommended Citation

Jeske, Torri C.. "Measurement of Pion-Pion Final State Interactions in $\eta \to \pi^+\pi^-\gamma$ with CLAS at Jefferson Lab" (2020). Doctor of Philosophy (PhD), Dissertation, Physics, Old Dominion University, DOI: 10.25777/g03a-tz27
https://digitalcommons.odu.edu/physics_etds/128

MEASUREMENT OF PION-PION FINAL STATE INTERACTIONS IN $\eta \rightarrow \pi^+\pi^-\gamma$ WITH CLAS AT JEFFERSON LAB

by

Torri C. Jeske

A Dissertation Submitted to the Faculty of
Old Dominion University in Partial Fulfillment of the
Requirements for the Degree of

DOCTOR OF PHILOSOPHY

PHYSICS

OLD DOMINION UNIVERSITY
December 2020

Approved by:

Moskov Amaryan (Director)

Alexander Gurevich (Member)

Sebastian Kuhn (Member)

Anatoly Radyushkin (Member)

Richard Zimmerman (Member)

ABSTRACT

MEASUREMENT OF PION-PION FINAL STATE INTERACTIONS IN $\eta \to \pi^+\pi^-\gamma$ WITH CLAS AT JEFFERSON LAB

Torri C. Jeske
Old Dominion University, 2020
Director: Dr. Moskov Amaryan

Decays of pseudoscalar mesons proceed from the chiral anomaly, which arises from spontaneous chiral symmetry breaking. In the limit of massless quarks (chiral limit), the $\eta \to \pi^+\pi^-\gamma$ decay width is determined solely by the box anomaly term in the Wess Zumino Witten Lagrangian. Since the physical quarks are not massless, the decay region of the η meson is far from the chiral limit and thus proper inclusion of the momentum dependence is essential to reproduce the measured decay width. Several theoretical frameworks have been proposed to describe these interactions. We report a new measurement of the α parameter which measures the contribution of pion-pion final state interactions to the differential decay width.

The data was collected during the g11a run period using the CEBAF Large Acceptance Spectrometer located in Hall B at the Thomas Jefferson National Accelerator Facility in 2004. The data was collected using a tagged photon beam with energy range of 1.5-3.5 GeV incident on a liquid Hydrogen target. Our results are in agreement with the latest experimental measurement and theoretical calculations.

ACKNOWLEDGMENTS

I could not have been successful in the pursuit of this thesis without my friends and family. To my parents; Tina, Kevin, and Chastity, and my brothers; Adrian, Julian, and Kevin, I hope this work makes you proud. To my husband Aaron, who has been on this journey with me while home and away. Although we have vastly different careers, you tried to understand my struggles and always gave me a shoulder to lean on. To Kendal and Erin, for years of friendship no matter what life throws at us.

I cannot express enough gratitude to David Payette. The first year of graduate school was possible because of you. Most importantly, your guidance and patience with teaching me how to code is something I am forever thankful for. You are a phenomenal teacher. To Dr. Jeremy Peshl, Tyler Viducic, and Josh Carter, you are the best coworkers-turned-friends I could have asked for. To Jeremy, for telling me every day that ”everything will be fine” when I was convinced otherwise and letting me escape to your lab as long as the door was left open. To Tyler, for listening to me complain before you bought noise canceling headphones, debugging my codes, and sharing our mutual obsession with dogs. To Josh, for always being there to listen even if you had no idea what I was talking about. I will miss our daily coffee walks, conversations, and of course the weekend shenanigans.

To Drs. Ilya Larin, Gagik Gavalian, Raffaella De Vita, Ken Hicks, and many others at Jefferson Lab, for providing so much knowledge and expertise with very old data and software, and for always being willing to help with my analysis. A special thank you to Nick Tyler, without whom this work would have never been finished.

To the Department of Physics at ODU, for a steadfast commitment to see their students succeed. To Lisa Okun for always listening and finding solutions to any problem. To Gail Dodge and Lepsha Vušković for Women in Physics dinners and supporting me both personally and professionally. To my Professors: Alexander Godunov, Alexander Gurevich, Anatoly Radyushkin, J. Wallace Van Orden, and Rocco Schiavilla, for making classes equal parts challenging and enjoyable with humor and stories included.

To my committee members; Profs. Sebastian Kuhn, Alexander Gurevich, Anatoly Radyushkin, and Richard Zimmerman, and Larry Weinstein for your time, advice, and suggestions for improving this work.

To my undergraduate research advsiors, Drs. Horia Petrache and Philip Gurnev; for letting me play around in the lab and giving me the initial ”push” into physics.

Finally, to my advisor, Moskov Amaryan. There are hardly any words I can come up

with to properly express my gratitude for your time serving as my advisor. You have taught me to have patience and persevere. Your endless commitment to physics is inspiring.

DEDICATION

This work is dedicated to my son, Adam. You are the light of my life.

TABLE OF CONTENTS

APPENDICES

LIST OF TABLES

LIST OF FIGURES

Figure Page

CHAPTER 1

INTRODUCTION

The structure of this thesis is organized as follows. Chapter 1 gives an introduction to the Standard Model and introduces the theoretical background of our experimental measurement.

Chapter 2 describes the CLAS spectrometer during the CLAS6 era when the data for this thesis was taken.

Chapter 3 summarizes the event selection and corrections applied to the data and describes the analysis.

Chapter 4 summarizes the results of our work.

1.1 THE STANDARD MODEL

The Standard Model describes fundamental particles and interactions that comprise and govern the visible matter of our Universe. The fundamental particles are called leptons, quarks, and bosons. The leptons include electrons, muons, and neutrinos and their corresponding antiparticles. The bosons include the photon, W and Z bosons, gluons, and the Higgs boson. The bosons (excluding the Higgs) are known as force mediators: the photon mediates the Electromagnetic force; the gluon mediates the Strong Nuclear Force; and the W and Z bosons mediate the Weak Nuclear Force. There are six quarks (q) and antiquarks ($\bar{q}$): up (u), down (d), strange (s), top (t), bottom (b) and charm (c). Quarks and leptons combine to form the visible matter in our Universe. The defining feature of quarks is that they possess color charge. Inside a hadron, quarks are very strongly bound to each other resulting (this is known as confinement) in a colorless composite states known as hadrons. There are two ways to form a colorless hadron: a quark-antiquark pair or a colorless combination of three quarks. A quark-antiquark pair is known as a meson while a combination of three quarks is known as a baryon. There is recent evidence suggesting the existence of exotic quark combinations, mainly tetraquarks and pentaquarks. Fig. 1 summarizes the fundamental particles and their properties. The Standard Model is written in the language of Quantum Field Theory, which describes the mechanics of very light particles traveling near the speed of light.

Even with the predictive success of the Standard Model, there are limitations. For instance, it does not yet incorporate gravity, predict the quark masses, describe neutrino oscillations, or incorporate any dark matter particle. In Fig. 1, the fundamental particles and their properties are summarized in visual form.

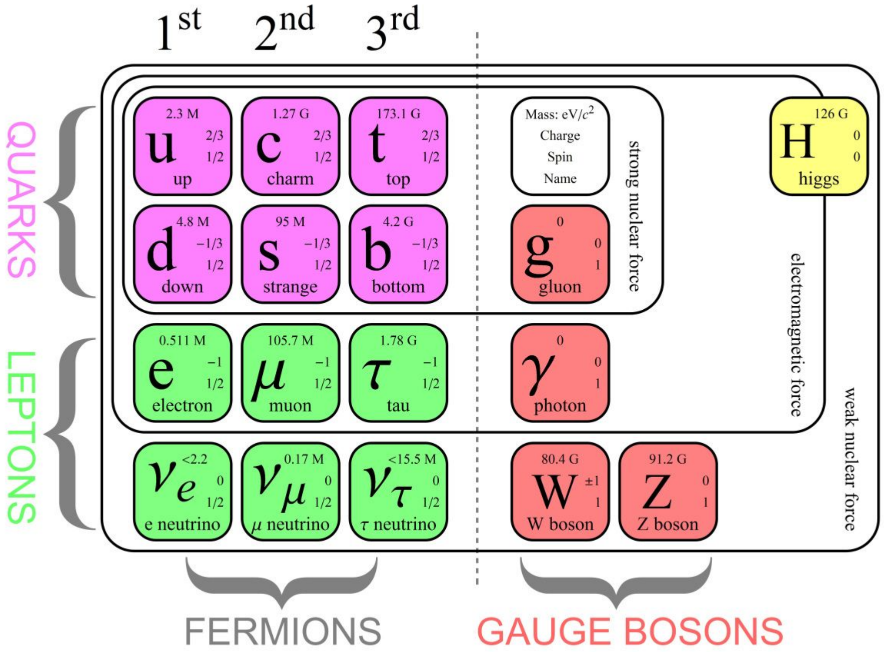

FIG. 1: Visual summary of the fundamental particles and their properties described in the Standard Model. Each square denotes the particle mass, charge, spin, and name from top to bottom. The first, second, and third notations correspond to the particle's generation. Image from [1].

To construct hadrons from quarks, the Quark Model was proposed by Gell-Man, Zweig, and Ne'eman. Assuming three types of quarks (u, d, and s), the colorless combinations yielded baryons and mesons. The baryons are summarized in Table 1. The meson combinations yield the meson nonet seen in 2 and tabulated in Table 2.

TABLE 1: Baryon Decuplet

qqq	Q	S	Baryon
uuu	2	0	Δ^{++}
uud	1	0	Δ^{+}
udd	0	0	Δ^{0}
ddd	-1	0	Δ^{-}
uus	1	-1	Σ^{*+}
uds	0	-1	Σ^{*0}
dds	-1	-1	Σ^{*-}
uss	0	-2	Ξ^{*0}
dss	-1	-2	Ξ^{*-}
sss	-1	-3	Ω^{-}

TABLE 2: Meson Nonet

q$\bar{q}$	Q	S	Meson
u$\bar{u}$	0	0	π^0
u$\bar{d}$	1	0	π^+
d$\bar{u}$	-1	0	π^-
d$\bar{d}$	0	0	η
u$\bar{s}$	1	1	K^+
d$\bar{s}$	0	1	K^0
s$\bar{u}$	-1	-1	K^-
s$\bar{d}$	0	-1	$\bar{K}^0$
s$\bar{s}$	0	0	η'

This approach led to the prediction of the Ω^- baryon and its discovery in 1964, for which Gell-Mann won the Nobel Prize.

Since baryons have three valence quarks, each with spin $\frac{1}{2}$, they have half integer spin and are thus fermions. Fermions obey Fermi-Dirac statistics and the Pauli exclusion principle. The Pauli exclusion principle states that two or more identical fermions cannot occupy the same state simultaneously. Mesons have two valence quarks and have integer spin and are bosons. Bosons obey Bose-Einstein statistics. Now, according to Table 1, there are baryons with the same quarks, which are also fermions. This appeared to violate the Pauli exclusion principle until the introduction of the color degrees of freedom in Quantum Chromodynamics. The two up quarks in the proton (and the down quark) must have different color, thus obeying the Pauli exclusion principle.

Much like classifying every day objects by their shape, size, and color, we can further classify subatomic particles by their intrinsic properties such as angular momentum and how they transform under certain operations. These properties are encoded in J^{PC} notation, where J is the *total* angular momentum, L is the angular momentum, and S is the spin angular momentum. The values J can take are:

$$|L - S| \leq J \leq |L + S|. \tag{1.1.1}$$

A naive example of the difference between L and S can be explained using the rotation of the Earth around the Sun (L) and the rotation of the Earth about its own axis (S). P represents parity conjugation, and inverts the sign of the spatial coordinates, $P = (-1)^{L+1}$. C represents charge conjugation and turns particles into antiparticles, $C = (-1)^{L+S}$. The classification of mesons using the quantum numbers above is presented in Table 3.

TABLE 3: Types of Mesons

Type	L	S	J	P	J^{PC}
Pseudoscalar	0	0	0	-	0^{-+}
Scalar	1	1	0	+	0^{++}
Vector	0	1	1	-	1^{--}
Axial Vector	1	0	1	+	1^{+-}
Tensor	1	1	2	+	2^{++}

1.2 THE η MESON AND ALLOWED DECAY MODES

The η meson is a pseudoscalar with quantum numbers $J^{PC} = 0^{-+}$. It is a light meson with mass of 547.862 ± 0.017 MeV and a lifetime of $(5.0 \pm 0.3) \cdot 10^{-19}$ s. It is part of the pseudoscalar meson nonet along with the charged and neutral pions and kaons.

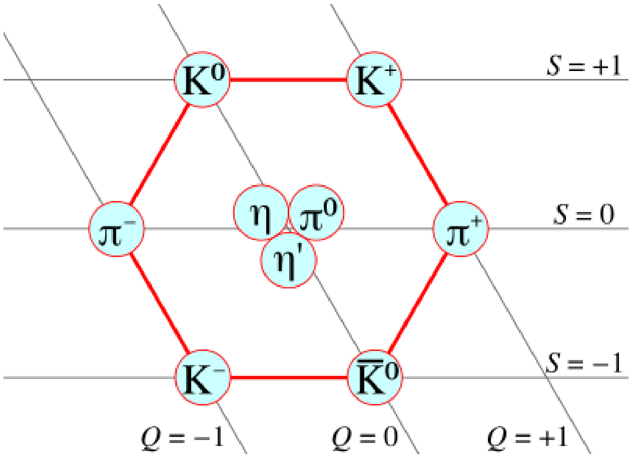

FIG. 2: Nonet of pseudoscalar mesons. The vertical axis is *strangeness*. It is equal to the difference in antistrange quarks and strange quarks. The diagonal axis corresponds to electric charge.

The physically observed η is a linear combination of the octet and single states η_8 and η_0, respectively. The quark content of the octet and singlet states are

$$\begin{aligned}\eta_0 &= \sqrt{\frac{2}{3}}\left(u\bar{u} + d\bar{d} + s\bar{s}\right)\\ \eta_8 &= \sqrt{\frac{1}{6}}\left(u\bar{u} + d\bar{d} - 2s\bar{s}\right).\end{aligned} \tag{1.2.2}$$

The octet state is a pseudo-Goldstone boson whose mass vanishes in the chiral limit, whereas the singlet state is not because of the anomalous breaking of the U(3) to SU(3) symmetry [24]. The combination is described using an experimentally determined mixing angle θ_{mix} and can be written as

$$\begin{pmatrix}\eta\\ \eta'\end{pmatrix} = \begin{pmatrix}-\sin\theta_{\text{mix}} & \cos\theta_{\text{mix}}\\ \cos\theta_{\text{mix}} & \sin\theta_{\text{mix}}\end{pmatrix}\cdot\begin{pmatrix}\eta_0\\ \eta_8\end{pmatrix} \tag{1.2.3}$$

where $\theta_{\text{mix}} \approx 20\,\text{deg}$ [24]. The mixing angle is an important quantity to test theoretical predictions with experimental results. The $\eta \to \pi^+\pi^-\gamma$ decay is C-conserving, with the C(η) = 1, C(γ) = -1, and C($\pi^+\pi^-$) = $(-1)^l$. Therefore, C invariance is only given for odd values of l. The most common decay modes of η meson are described in Table 4.

Decay	Branching Ratio
$\eta \to 2\gamma$	$39.3 \pm 0.20\%$
$\eta \to 3\pi^0$	32.56 ± 0.23 %
$\eta \to \pi^+\pi^-\pi^0$	22.73 ± 0.28 %
$\eta \to \pi^+\pi^-\gamma$	4.22 ± 0.08 %
$\eta \to e^+e^-\gamma$	$(7.0 \pm 0.7) \cdot 10^{-3}$ %

TABLE 4: Most common decay modes of the η meson.

1.3 SYMMETRIES AND THE CHIRAL ANOMALY

All of the dynamics of a classical system can be determined from a function called the Lagrangian. The Lagrangian is equal to the difference in kinetic and potential energies of the system. From this, the equations of motion can be derived using the Euler-Lagrange equations: In one dimension, this is written as:

$$\frac{d}{dt}\frac{\partial L}{\partial \dot{x}} - \frac{\partial L}{\partial x} = 0, \tag{1.3.4}$$

where the single dot notation represents the first time derivative. Another important quantity is called the action, defined as

$$S = \int L dt. \tag{1.3.5}$$

A very important principle in physics is that of least action: given an infinite number of paths between two points, a particle will take the one which minimizes the action. Examples of classical actions and their symmetries are summarized in Table 5. In quantum field theory, the Lagrangian becomes a function of spacetime, and for a field ϕ, the Euler-Lagrange equations become

$$\frac{\partial \mathcal{L}}{\partial \phi} - \partial_\mu \left(\frac{\partial \mathcal{L}}{\partial [\partial_\mu \phi]} \right) = 0 \tag{1.3.6}$$

Symmetries arise from transformations that do not change the physics of a system. Noether's theorem expresses the relationship between symmetries and conservation laws: for every continuous transformation that leaves the action invariant there exists a time dependent classical charge Q and corresponding conserved current, $\partial_\mu J^\mu = 0$. The quantity inside the parenthesis in Eq.1.3.6 is defined as the current J^μ. The conserved charge is found by integrating the time component of the current,

$$Q = \int d^3x J^0. \tag{1.3.7}$$

TABLE 5: Symmetries and Conservation Laws

Symmetry	Conservation Law
Translation in time	Energy
Translation in space	Momentum
Rotation	Angular Momentum
Gauge transformation	Charge

In general, there are three different types of symmetries: exact, broken, and approximate. Exact symmetries are valid under any condition; approximate symmetries are valid under certain conditions; and broken symmetries arise under various circumstances where the Lagrangian is still invariant under the given transformation but the ground state is not. When a classical symmetry is broken in the realm of quantum physics it is an anomalous symmetry.

The chiral symmetry, $SU_L(3) \times SU_R(3)$, of QCD occurs when the three light quarks: u, d, and s are massless. This symmetry is spontaneously broken which gives rise to the octet of massless Goldstone bosons, which are identified as the pseudoscalar pions, kaons, and eta mesons. A chiral transformation is one of the form:

$$\Psi \rightarrow \Psi' = e^{-i\theta\gamma_5}\Psi, \tag{1.3.8}$$

where θ measures the rotation and $\gamma^5 = i\gamma^0\gamma^1\gamma^2\gamma^3$ is the product of the four gamma matrices. As a straightforward example, one can apply the chiral transformation to demonstrate the conservation of the axial vector current, $j^{\mu 5} = \bar{\Psi}\gamma_\mu\gamma_5\Psi$, using the Dirac Lagrangian

$$L_{Dirac} = \bar{\Psi}(i\gamma^\mu\partial_\mu - m)\Psi. \tag{1.3.9}$$

The wavefunctions under a chiral transformation become

$$\begin{aligned} \Psi &\rightarrow \Psi' = e^{-i\theta\gamma^5}\Psi \\ \bar{\Psi} &\rightarrow \bar{\Psi}' = \bar{\Psi}e^{i\theta\gamma^5}. \end{aligned} \tag{1.3.10}$$

Using the axial vector current and the Dirac equation, the divergence can be calculated as

$$\partial_\mu j^{\mu 5} = (\partial_\mu\bar{\Psi})\gamma^\mu\gamma^5\Psi - \bar{\Psi}\gamma^5\gamma^\mu\partial_\mu\Psi = 2im\bar{\Psi}\gamma_5\Psi. \tag{1.3.11}$$

Clearly, if the mass of the particle is zero the axial vector current is conserved. When a gauge field (A_μ) is present, as in,

$$\mathcal{L} = \bar{\Psi}[i\gamma^\mu(\partial_\mu - ieA_\mu) - m]\Psi, \tag{1.3.12}$$

one can find that the axial vector current is no longer conserved even when the particle mass is zero:

$$\partial^\mu j_{5\mu} = -\frac{e^2}{16\pi^2}\epsilon^{\mu\nu\alpha\beta}F_{\mu\nu}F_{\alpha\beta}, \tag{1.3.13}$$

where $F_{\mu\nu} = \partial_\mu A_\nu - \partial_\nu A_\mu$ is the electromagnetic field strength tensor, $\epsilon^{\mu\nu\alpha\beta}$ is the Levi-Civita tensor, and e is the electric charge. This result was first discovered by Adler, Bell, and Jackiw and is known as the ABJ or chiral anomaly.

1.4 QCD AND THE WZW LAGRANGIAN

Quantum Chromodynamics (QCD) is the theory that describes the strong interaction that exists between the quarks and gluons in hadrons. Two main features of QCD include:

1. Color confinement: This is why we do not observe individual quarks themselves. In order to separate quarks inside a hadron, increasing amounts of energy are required. This would become so great that a quark-antiquark pair would be produced, resulting in a pair of hadrons.

2. Asymptotic freedom: The asymptotic freedom of QCD was discovered by David Gross and Frank Wilczek and independently by David Politzer. Asymptotic freedom describes a reduction in the strength of interactions between the quarks and gluons as the energy scale increases.

The QCD Lagrangian is given by:

$$\mathcal{L}_{QCD} = -\frac{1}{2}Tr[G_{\mu\nu}G^{\mu\nu}] + \bar{q}(i\gamma_\mu D^\mu - m)q \tag{1.4.14}$$

where

$$\begin{aligned} G_{\mu\nu} &= \partial_\mu G_\nu - \partial_\nu G_\mu - ig[G_\mu, G_\nu] \\ D_\mu q &= (\partial_\mu - igG_\mu)q \end{aligned} \tag{1.4.15}$$

and where $G_\mu = G^a_\mu \lambda^a/2$ is the vector field of the gluons and $G_{\mu\nu}$ is the field strength tensor. In low energy QCD, Chiral Perturbation Theory exploits the global $SU(3)_L \times SU(3)_R$ symmetry in the limit of vanishing quark masses. Following Witten's approach in [5], the lowest order effective chiral action is:

$$S = \frac{f_\pi^2}{4}\int d^4x \mathrm{Tr}[(D_\mu U)(D^\mu U^\dagger)] \tag{1.4.16}$$

with U being the chiral unitary matrix

$$U = \exp\left(\frac{i\sqrt{2}}{f_\pi}P\right) \tag{1.4.17}$$

and with P being the pseudoscalar field matrix

$$\begin{pmatrix} P = \frac{1}{\sqrt{2}}\pi^0 + \frac{1}{\sqrt{6}}\eta_8 + \frac{1}{\sqrt{3}}\eta_0 & \pi^+ & K^+ \\ \pi^- & -\frac{1}{\sqrt{2}}\pi^0 + \frac{1}{\sqrt{6}}\eta_8 + \frac{1}{\sqrt{3}}\eta_0 & K^0 \\ K^- & \bar{K}^0 & -\sqrt{\frac{2}{3}}\eta_8 + \frac{1}{\sqrt{3}}\eta_0 \end{pmatrix}. \tag{1.4.18}$$

The Wess-Zumino-Witten Lagrangian is of the form

$$\begin{aligned} \Gamma_{WZW} &= \frac{iN_c}{240\pi^2}\int_M d\Sigma^{ijklm} Tr\left((U^\dagger\partial_i U)(U^\dagger\partial_j U)(U^\dagger\partial_k U)(U^\dagger\partial_l U)(U^\dagger\partial_m U)\right) \\ &= -\frac{N_c}{240\pi^2 F_\pi^5}\int dx^4 Tr(\phi^a\partial_\mu\phi^a\partial_\nu\phi^a\partial_\alpha\phi^a\partial_\beta\phi^a)\epsilon^{\mu\nu\alpha\beta} + \text{higher orders} \end{aligned} \tag{1.4.19}$$

where N_c is the number of colors and F_π is the pion decay constant. When the Lagrangian is coupled to a photon field A_μ, it is of the form [24]

$$\begin{aligned} \mathcal{L}_{WZW}(UA_\mu) = \mathcal{L}_{WZW}(U) & \\ &+ \frac{eN_c}{48\pi^2}\epsilon^{\mu\nu\alpha\beta}\int d^4x A_\mu Tr(Q(R_\nu R_\alpha R_\beta + L_\nu L_\alpha L_\beta)) \\ &- \frac{iN_c e^2}{48\pi^2}\epsilon^{\mu\nu\alpha\beta}\int d^4x F_{\mu\nu}A_\alpha Tr\left(Q^2(R_\beta + L_\beta) + \frac{1}{2}(QU^\dagger QUR_\beta + QUQU^\dagger L_\beta)\right) \end{aligned} \tag{1.4.20}$$

where Q is the quark charge matrix, $F_{\mu\nu} = \partial_\mu A_\nu - \partial_\nu A_\mu$ is the electromagnetic field strength tensor, and R_μ and L_μ are defined as $(\partial_\mu U^\dagger)U$ and $U\partial_\mu U^\dagger$, respectively. The first term corresponds to the quintangle anomaly $K^+K^- \to \pi^+\pi^-\pi^0$. The second term represents the QCD box anomaly and the third term corresponds to the triangle anomaly. The triangle and box diagrams are shown in Fig.3.

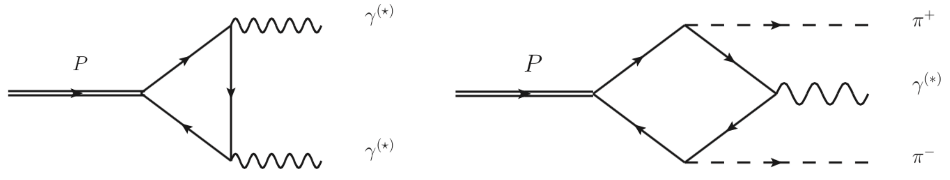

FIG. 3: The decay of a pseudoscalar meson P to two photons and to $\pi^+\pi^-\gamma$. The AVV anomaly (left) describes the coupling of two vector mesons and a pseudoscalar, while the VAAA anomaly (right) describes the coupling of three pseudoscalar mesons and a vector meson.

At the chiral limit ($s_{\pi^+\pi^-} = 0$), the decay amplitude can be written [24] from the box anomaly term of the $\mathcal{L}_{WZW}$ coupled to a photon field:

$$\mathcal{A}_{\eta\to\pi^+\pi^-\gamma}(0,0,0) = \frac{eN_c}{12\sqrt{3}\pi^2 F_\pi^3}\left(\frac{F_\pi}{F_8}\cos\theta - \sqrt{2}\frac{F_\pi}{F_0}\sin\theta\right)\epsilon^{\mu\nu\alpha\beta}\epsilon^*_\mu p_{+\nu} p_{-\alpha} k_{\gamma\beta} \tag{1.4.21}$$

where F_0 and F_8 are the decay constants for the singlet and octet η states, θ is the mixing angle, $p_\pm$ and k are the momenta of the pions and photon, and ϵ^* is the polarization of the photon. The resulting decay rate $\Gamma_{\eta\to\pi^+\pi^-\gamma} = 35.7$ eV [24] is nearly a factor of two smaller than the experimental value of $\Gamma_{\eta\to\pi^+\pi^-\gamma} = 60 \pm 4$ eV. The physical decay region, $4m^2_{\pi^\pm} \le s_{\pi^+\pi^-} \le m^2_\eta$, is far from this region, thus proper inclusion of the momenta of the pions and final state interactions is essential.

1.5 DECAY RATE AND AMPLITUDE CALCULATIONS

In this section we will derive the amplitude and the decay rate for the decay $\eta \to \pi^+\pi^-\gamma$ following the procedure in [6]. For the reaction $P(P) \to \pi^+(p_+)\pi^-(p_-)\gamma(k)$, momentum conservation gives

$$P = p_+ + p_- + k. \tag{1.5.22}$$

The invariant decay amplitude can be written as given in [6]

$$\mathcal{A}(\eta\to\pi^+\pi^-\gamma) = \frac{i}{m_\eta^3}\left(M_G\epsilon_{\mu\nu\alpha\beta}\epsilon^\mu k^\nu p_+^\alpha p_-^\beta + E_g[(\epsilon\cdot p_+)(k\cdot p_-) - (\epsilon\cdot p_-)(k\cdot p_+)]\right), \tag{1.5.23}$$

where M and E are the magnetic and electric form factors. To calculate the squared amplitude, and eventually the decay rate, we can insert $p_- = P - p_+ - k$ to take advantage of the antisymmetric tensor:

$$\mathcal{A}(\eta \to \pi^+\pi^-\gamma) = \frac{i}{m_\eta^3}\left(M_G \epsilon_{\mu\nu\alpha\beta}\epsilon^\mu k^\nu p_+^\alpha P^\beta + E_G[(\epsilon \cdot p_+)(k \cdot P) - (\epsilon \cdot P)(k \cdot p_+)]\right). \quad (1.5.24)$$

In the rest frame of the η, $P^\mu = m_\eta \delta^{\mu 0}$, the amplitude then reads

$$\mathcal{A}(\eta \to \pi^+\pi^-\gamma) = \frac{i}{m_\eta^2}\left(-M_G \epsilon^{ijk}\epsilon^i \tilde{k}^j \tilde{p}_+^k + E_G\left[(-\epsilon \cdot \tilde{\mathbf{p}}_+)(\tilde{E}_\gamma)\right]\right)$$

$$= \frac{i\tilde{E}_\gamma}{m_\eta^2}\left(M_G \hat{\mathbf{k}} \cdot (\boldsymbol{\epsilon} \times \tilde{\mathbf{p}}_+) - E_G \boldsymbol{\epsilon} \cdot \tilde{\mathbf{p}}_+\right). \quad (1.5.25)$$

Squaring the amplitude yields

$$|\mathcal{A}|^2(\eta \to \pi^+\pi^-\gamma) = \frac{\tilde{E_\gamma}^2}{m_\eta^4}\Big(|M_G|^2|\hat{\boldsymbol{k}} \cdot (\boldsymbol{\epsilon} \times \mathbf{p}_{+\perp})|^2 + |E_G|^2|\boldsymbol{\epsilon} \cdot \mathbf{p}_{+\perp}$$

$$+E_G^* M_G \left[\hat{\mathbf{k}} \cdot (\mathbf{p}_{+\perp} \times \boldsymbol{\epsilon})\right](\boldsymbol{\epsilon} \cdot \mathbf{p}_{+\perp})^* + M_G^* E_G \left[\hat{\mathbf{k}} \cdot (\mathbf{p}_{+\perp} \times \boldsymbol{\epsilon})\right]^*(\boldsymbol{\epsilon} \cdot \mathbf{p}_{+\perp})^*\Big). \quad (1.5.26)$$

Ref. [6] defines the polarization vectors as:

$$\boldsymbol{\epsilon_1} = \frac{(\mathbf{p}_+ \times \mathbf{k}) \times \mathbf{k}}{|(\mathbf{p}_+ \times \mathbf{k}) \times \mathbf{k}|} = \frac{\hat{\mathbf{k}}(\mathbf{p}_+ \cdot \hat{\mathbf{k}}) - \mathbf{p}_+}{|\hat{\mathbf{k}}(\mathbf{p}_+ \cdot \hat{\mathbf{k}}) - \mathbf{p}_+|} = -\hat{\mathbf{p}}_{+\perp} \quad (1.5.27)$$

and

$$\boldsymbol{\epsilon}_2 = \frac{\mathbf{p}_+ \times \mathbf{k}}{|\mathbf{p}_+ \times \mathbf{k}|} = \frac{\mathbf{p}_{+\perp} \times \hat{\mathbf{k}}}{|\mathbf{p}_{+\perp} \times \hat{\mathbf{k}}|} = \hat{\mathbf{k}} \times (-\hat{\mathbf{p}}_{+\perp}). \quad (1.5.28)$$

This results in an unpolarized square decay amplitude:

$$\sum_{\text{pol}=1}^{2} |\mathcal{A}|^2(\eta \to \pi^+\pi^-\gamma) = \frac{\tilde{E}_\gamma^2 |\mathbf{p}_+^*|^2 \sin^2\theta_\pi}{m_\eta^4}\left(|M_G(s_{\pi\pi})|^2 + |E_G|^2\right). \quad (1.5.29)$$

Rewriting Eq. 1.5.29 in terms of standard variables $s_{\pi\pi}$ and θ_π is

$$\sum_{\text{pol}=1}^{2} |\mathcal{A}|^2(\eta \to \pi^+\pi^-\gamma) = \frac{\lambda(m_\eta^2, s_{\pi\pi}, 0) s_{\pi\pi} \beta_\pi^2 \sin^2\theta_\pi}{16 m_\eta^2}\left(|M_G|^2 + |E_G|^2\right), \quad (1.5.30)$$

where

$$\beta_\pi = \sqrt{1 - \frac{4m_\pi^2}{s_{\pi\pi}(\tilde{E}_\gamma)}}. \quad (1.5.31)$$

The partial decay rate for $\eta \to \pi^+\pi^-\gamma$ is given by eq.(46.19) in [2].

$$\begin{aligned} d\Gamma &= \frac{1}{(2\pi)^5}\frac{1}{16m_\eta^2}|\mathcal{A}|^2|\mathbf{p}_+^*||\tilde{E}_\gamma dm_{\pi\pi}\mathrm{d}\cos\theta_\pi \mathrm{d}\phi_\pi^* \mathrm{d}\cos\tilde{\theta}_\gamma \mathrm{d}\tilde{\phi}_\gamma \\ &= \frac{1}{2^{12}\pi^3}\left(1-\frac{s_{\pi\pi}}{m_\eta^2}\right)^3 \frac{s_{\pi\pi}^{3/2}}{m_\eta^3}\beta_\pi^3 \sin^2\theta_\pi(|M_G(s_{\pi\pi})|^2+|E_G|^2)d\sqrt{s_{\pi\pi}}d\cos\theta_\pi, \end{aligned} \tag{1.5.32}$$

where

$$M_G(s_{\pi\pi}) = m_\eta^3\mathcal{M}(s_{\pi\pi}, k^2=0), \tag{1.5.33}$$

and where

$$M(s_{\pi\pi}, k^2=0) = \mathcal{A}_{\eta\to\pi\pi\gamma}(0,0,0)\times F. \tag{1.5.34}$$

Eq.1.5.34 is a product of the chiral limit amplitude with a form factor F. For the specific decay of interest, $\mathcal{M}$ is equal to Eq.1.4.21. To leading order, the electric form factor, $|E_G|$ is set to zero. In the next section, we describe different approaches to describe the form factor F in Eq.1.5.34.

1.6 MODEL PREDICTIONS FOR $\eta \to \pi^+\pi^-\gamma$

Proper inclusion of the final state interactions has been attempted using various theoretical models. Each of these models are briefly summarized below.

a) VMD: In this model, the decay amplitude is modified either using the simplest possible

$$F_V(s_{\pi\pi}) = -\frac{m_\rho^2}{s_{\pi\pi} - m_{\rho^2} i m_\rho \Gamma_\rho} \tag{1.6.35}$$

The resulting total decay width is $\Gamma^{VMD}(\eta \to \pi^+\pi^-\gamma) = 62.3$ eV.

b) N/D: The $\pi\pi$ final state interactions are taken into account using contributions from both vector meson dominance as well as one-loop corrections. The modification to the decay amplitude is

$$\left(1 - c + c\cdot\frac{1+as_{\pi\pi}}{D_1(s_{\pi\pi})}\right) \tag{1.6.36}$$

The Omnes function, $D_1(s_{\pi\pi})$ incorporates $\pi\pi$ scattering phase space. The parameter c is set to 1, while $a = \frac{1}{2m\rho^2}$. The modified decay width using this approach is $\Gamma^{N/D}(\eta \to \pi^+\pi^-\gamma) = 65.7$ eV [24], and the predicted value for the α parameter is 0.64 ± 0.02.

c) Inclusion of pion loop corrections and higher order momenta on the order $\mathcal{O}(p^6)$. The form factor was modified using the one-loop formulation

$$F_V(s_{\pi\pi}) = 1 + \frac{1}{6f_\pi^2}(s_{\pi\pi} - 4m_\pi^2)\bar{J}(s_{\pi\pi}) + \frac{s_{\pi\pi}}{6}\left(\langle r^2\rangle + \frac{1}{24\pi^2 f_\pi^2}\right). \quad (1.6.37)$$

This leads to the predicted decay width of $\Gamma(\eta \to \pi^+\pi^-\gamma) = 47$ eV [19]. The prediction for the α parameter is -0.7 ± 0.1.

d) Uses the Hidden Local Symmetries (HLS) model, which describes γ-V transitions. The vector mesons are treated as degrees of freedom with pseudoscalar mesons and contact terms. The Lagrangian describing the $\eta \to \pi^+\pi^-\gamma$ decay consists of both a resonant term and a contact term, which contains the box anomaly term. The decay rate calculated from this model is $\Gamma(\eta \to \pi^+\pi^-\gamma)^{HLS} = 56.3 \pm 1.7$ eV [21]. The prediction for the α parameter is 0.23 ± 0.01.

e) Kubis and Plenter [40] consider the effects of the a2 tensor meson, which is the lowest lying resonance that can contribute in the $\pi\eta$ system. This analysis did not report a predicted decay width and instead provided a new prediction of the α parameter to be 1.52 ± 0.06.

Models a-d essentially modify the amplitude in the chiral limit, Eq. 5, by a form factor specific to each model. The predicted decay widths are in better agreement with the experimental value compared to the decay width from the chiral limit. The shape of the dipion invariant mass spectra is more sensitive to the description of the final state interactions which will give more insight into the agreements between the experimental decay rates and the theoretical predictions mentioned previously.

1.7 MODEL-INDEPENDENT ANALYSIS OF $\eta \to \pi^+\pi^-\gamma$

The approach to obtain the α parameter is based on [7] and will be described briefly below. It combines chiral perturbation theory (ChPT), extended from SU(3) to U(3), and a dispersive analysis. It is general and can be applied to all decays of mesons with a $\pi\pi\gamma$ final state, where soft bremsstrahlung does not occur and where the pion pair is of invariant mass square below the first significant $\pi\pi$ threshold. The need for this approach arises from the significant deviation between the theory predictions and data, which mostly stems from the non-perturbative $\pi\pi$ final state interaction.

The method involves two main steps. The first step is to fit the spectral decay data with a function of the form

$$\frac{d\Gamma}{ds_{\pi\pi}} = |AP(s_{\pi\pi})F_V(s_{\pi\pi})|^2\Gamma_0(s_{\pi\pi}), \tag{1.7.38}$$

where the normalization parameter A has the dimensions of mass^{-3} and where

$$\Gamma_0 = \frac{1}{3 \cdot 2^{11} \cdot \pi^3 m_\eta^3} \left(m_\eta^2 - s_{\pi\pi}\right)^3 s_{\pi\pi}\sigma(s_{\pi\pi})^3, \tag{1.7.39}$$

and

$$\sigma(s_{\pi\pi}) = \sqrt{1 - \frac{4m_\pi^2}{s_{\pi\pi}}}. \tag{1.7.40}$$

represents the phase-space terms and the kinematics of the absolute square of the simplest gauge invariant matrix element (for point particles). The decay rate is equivalent to the decay rate derived in Section 1.4, provided the electric form factor is set to zero in the leading order, and the form factor is replaced with the pion vector form factor and the reaction specific polynomial $P(s_{\pi\pi})$.

The pion vector form factor $F_V(s_{\pi\pi})$ is well known from both theory ([8]-[14]) and measurements of $e^+e^- \to \pi^+\pi^-$ ([15]-[18]). It collects all non-perturbative $\pi\pi$ interactions and is universal. It is defined in terms of the vector-isovector current:

$$\langle \pi^+(p')\pi^-(p)|V_\mu^3|0\rangle = (p - p')_\mu F_V(s_{\pi\pi}). \tag{1.7.41}$$

In the elastic regime, the form factor is defined as

$$F_V = M_V + T_{\pi\pi}G_{\pi\pi}M_V, \tag{1.7.42}$$

where M_V, $G_{\pi\pi}$, and $T_{\pi\pi}$ stand for the production vertex, the two-pion propagator and the $\pi\pi$ scattering amplitude, respectively. In this approach, M_V is assumed to be real. From Eq. 1.6.35, we can write

$$\mathrm{Im}(F_V(s_{\pi\pi})) = \sigma(s_{\pi\pi})T_{\pi\pi}(s_{\pi\pi})^* F_V(s_{\pi\pi}). \tag{1.7.43}$$

It is at this point where the variance between different models can be seen. In terms of Vector Meson Dominance, the relative strength of the first and second term is a free parameter. With the model independent approach used for our analysis, this is not a possibility. Instead, the authors use a twice subtracted dispersion integral:

$$F_V(s_{\pi\pi}) = \exp\left(\frac{1}{6}s_{\pi\pi}\langle r^2\rangle + \frac{s_{\pi\pi}^2}{\pi}\int_{4m_\pi^2}^{\infty} ds \frac{\delta_{11}(s)}{s^2(s - s_{\pi\pi} - i\epsilon)}\right), \tag{1.7.44}$$

where $\langle r^2 \rangle$ is the mean pion radius and δ_{11} is the phase, in order to guarantee that the integral over the phase space converges in the elastic regime. For our kinematic region, the pion vector form factor is approximated as

$$|F_V(s_{\pi\pi})| \approx 1 + (2.12 \pm 0.01)s_{\pi\pi} + (2.13 \pm 0.01)s_{\pi\pi}^2 + (13.80 \pm 0.14)s_{\pi\pi}^3. \tag{1.7.45}$$

The form factor contains both the Born term as well as the final state interactions. The right plot in Fig. 4 shows the form factor in the appropriate kinematic range for the η decay. From the plot, visible differences between the one loop calculation and the result derived from the dispersion integral are already apparent.

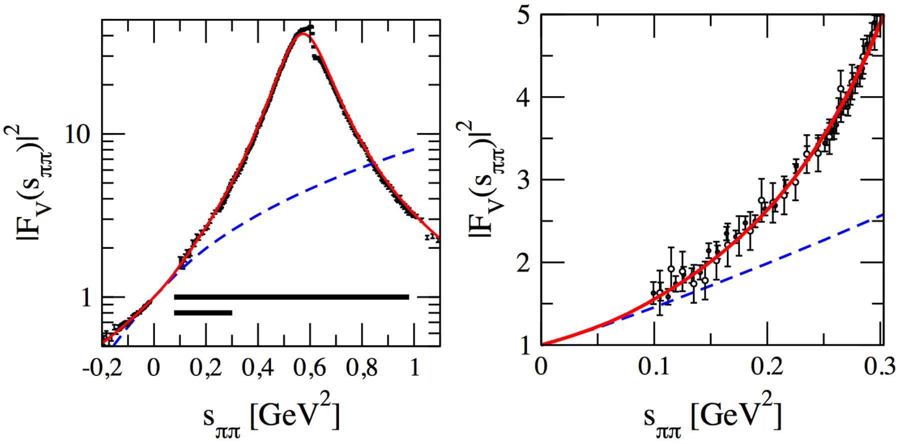

FIG. 4: The (red) solid band shows the form factor derived from Eq. 1.6.39, the (blue) dashed line is the result from one-loop ChPT with identical values of the pion radius. The time-like data is shown as solid and open circles, respectively. The space-like data are from. The short (long) thick, horizontal bar in the left panel denotes the kinematic range covered in the decay of the η (η') meson. The right panel shows a zoom into the $s_{\pi\pi}$ range relevant for the η decay.

The normalization parameter A and the function $P(s_{\pi\pi})$ are reaction specific. The polynomial $P(s_{\pi\pi})$ is expanded in a Taylor series around $s_{\pi\pi} = 0$,

$$P(s_{\pi\pi}) = 1 + \alpha s_{\pi\pi} + \mathcal{O}\left(s_{\pi\pi}^2\right). \tag{1.7.46}$$

The parameters A and α allow insights into the physics underlying the decay process. This is described in the second step of the method by developing a matching scheme to relate A and α to the parameters of the underlying effective field theory.

CHAPTER 2

CEBAF, CLAS, AND THE G11 EXPERIMENT AT JEFFERSON LAB

To study fundamental and/or composite particles and their interactions, physicists can gain insight using three different methods. The first involves scattering events. This essentially corresponds to firing one particle at another and recording what happens. The second involves decays, in which one particle decays into many particles and we observe the decay products. The third method involves studying bound states, or the combination of two or more particles. At Jefferson Lab, these types of interactions are studied using an electron accelerator (CEBAF) that can send electrons (or for some Halls, photons) at different experimental targets.

This chapter describes the Continuous Electron Beam Accelerator Facility (CEBAF), the CEBAF Large Acceptance Spectrometer, and the G11 Experiment that took place at the Thomas Jefferson National Accelerator Facility located in Newport News, Virginia before the 12 GeV upgrade. Since the data for this thesis was taken in 2004, the detector and the lab facilities will be described as they were during data taking. The main components of CEBAF and CLAS are described and a brief overview of the G11 experiment is provided.

2.1 THOMAS JEFFERSON NATIONAL ACCELERATOR FACILITY

The data for this thesis was collected in Hall B at the Thomas Jefferson National Acceleration Facility (JLAB) during the Summer of 2004. At the time, JLAB was home to the Continuous Electron Beam Accelerator Facility (CEBAF), three Experimental Halls: A, B, and C, and numerous other research facilities. Hall B is home to the CEBAF Large Acceptance Spectrometer (CLAS) detector. The CLAS detector is composed of many detector systems in order to provide charged particle resolution and a large angular acceptance.

FIG. 5: Aerial view of the Thomas Jefferson National Accelerator Facility in Newport News, VA. The three experimental Halls can be seen in the lower right corner of the image.

2.2 CONTINUOUS ELECTRON BEAM ACCELERATOR FACILITY

Construction on the Continuous Electron Beam Accelerator Facility started on February 13, 1987. The machine has a racetrack configuration with two superconducting linear accelerator (LINACs) segments connected by beam lines to allow recirculation passes. The superconducting radio frequency (SRF) cavities are used to accelerate electrons and provide beam to all experimental halls.

The electron beam is produced at the injector using an electron gun. Three diode lasers produce pulses which illuminate a GaAs photocathode. The pulses are timed so that each experimental hall receives electron bunches every 2 ns. Initially, the electrons are accelerated to 100 keV and then an optical chopper improves the separation of the bunches. Then, CEBAF uses superconducting radio frequency (SRF) cavities in order to accelerate the electrons. Superconducting cavities are non-resistive, allowing CEBAF to obtain a 100% duty factor. The electrons are then sent into the recirculating linear accelerators (LINACs). Fig. 6 displays a pair of Niobium SRF cavities.

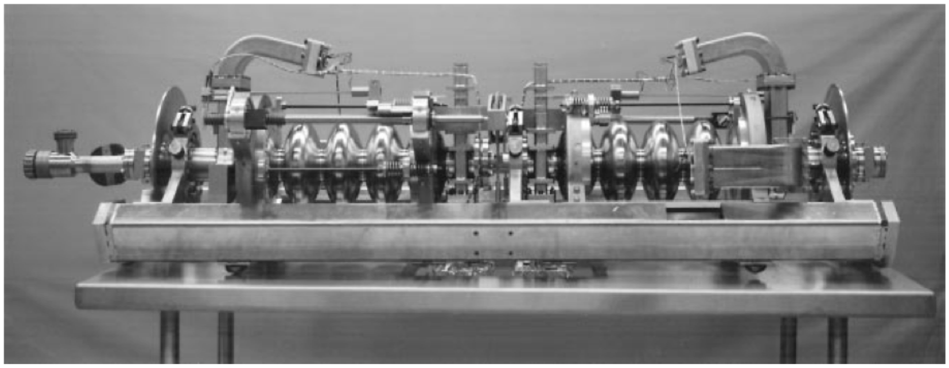

FIG. 6: Pair of superconducting Niobium cavities.

Each LINAC consists of 168 superconducting RF Niobium cavities. Each cavity is immersed in liquid Helium within a cryomodule and is cooled to -271deg C. Each LINAC is capable of providing 600 MeV of acceleration. The LINACs are connected by 9 recirculating arcs. The arcs allow the beam to make up to five passes through each LINAC, resulting in a maximum energy of ≈ 6 GeV. Each hall can extract the beam after any number of passes, although no two halls can run with the same lower energy.

The operating conditions and parameters for CEBAF are summarized in Table **??**.

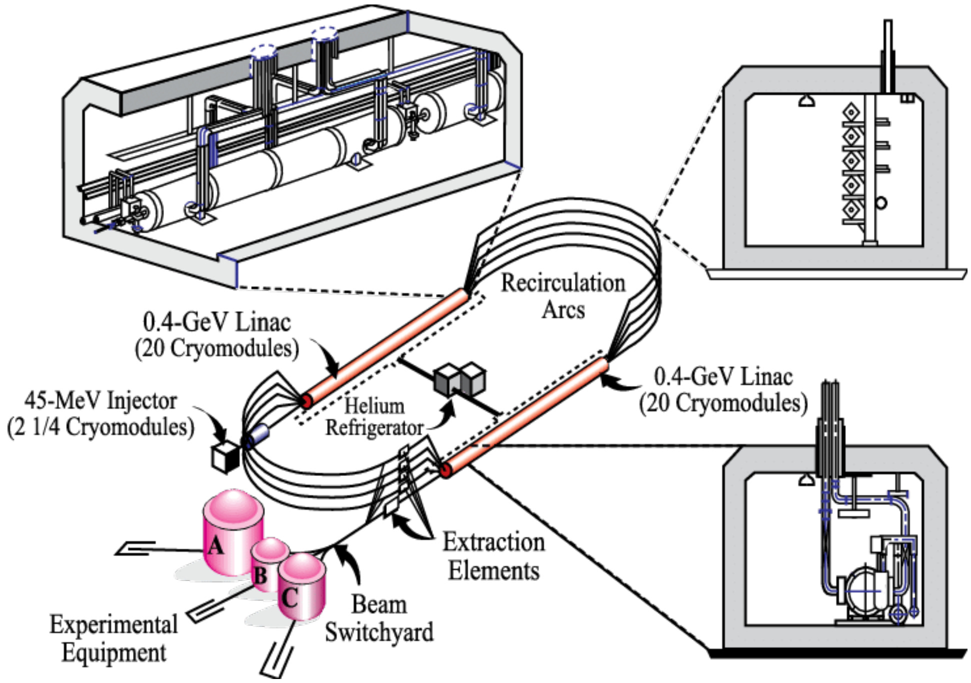

FIG. 7: Schematic of the Continuous Electron Beam Accelerator Facility (CEBAF).

2.3 PHOTON TAGGER

For our experiment, the electron beam must be converted into a photon beam. This is accomplished with the photon tagging system, shown in Fig. 8. The electron beam interacts with a gold foil radiator, producing photons via Bremsstrahlung radiation. Bremsstrahlung, from *bremsen* "to brake" and *strahlung* "radiation", refers to the process of producing radiation from decelerated charged particles deflected from nuclei. Since the nucleus of an atom is much heavier than the electron, the energy transferred to the nucleus is negligible. To satisfy conservation of energy, the energy of the Bremsstrahlung photon is equal to the difference of the incident electron energy and the deflected electron energy. For the setup in CLAS, the Bremsstrahlung photons and the decelerated electrons are traveling along the same direction as the initial incident electron.

A radiator with 10^{-4} radiation lengths was used during the production runs, while a much thinner radiator was used during normalization runs. The radiation length refers to the thickness of a material required to reduce the mean energy of an electron by a factor of e. It is defined as

$$\frac{1}{L_0} = \frac{4Z(Z+1)r_e^2 N_0}{137 \cdot A} \cdot \ln \frac{183}{Z^{1/3}}, \tag{2.3.47}$$

where $r_e = \frac{e^2}{mc^2}$, N_0 is Avogadro's number, Z (A) is the atomic (mass) number of the nucleus, and where e (m) is the charge (mass) of the electron.

After interacting with the Gold foil target, the beam now consists of a mix of electrons and photons. A dipole magnetic field is used to separate electrons from the photon beam and allows the photons to proceed towards the CLAS target. The magnetic field directed the recoil electrons towards two hodoscope planes, each made of overlapping arrays of scintillators. The first hodoscope plane, called the E plane, measures the momentum of the recoil electrons and the energy of the emitted photon. The second hodoscope, called the T plane, measures the timing information needed for the coincidence with events triggered by the interaction of corresponding photons in the target. Together, the E and T planes can tag photon energies in the range of 20-95% of the initial electron energy. Fig. 9 shows a schematic of the E and T planes.

The remaining components of the tagging system are collimators. These are used to trim the beam halos. There are sweeping magnets between the collimators to remove any unwanted particles from the interaction of the photon beam with the first collimator.

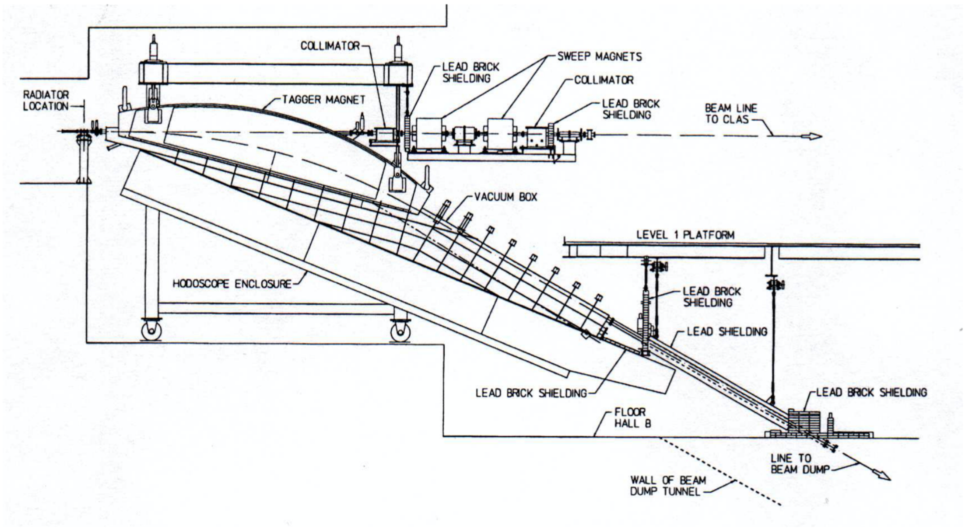

FIG. 8: Photon Tagging system in Hall B.

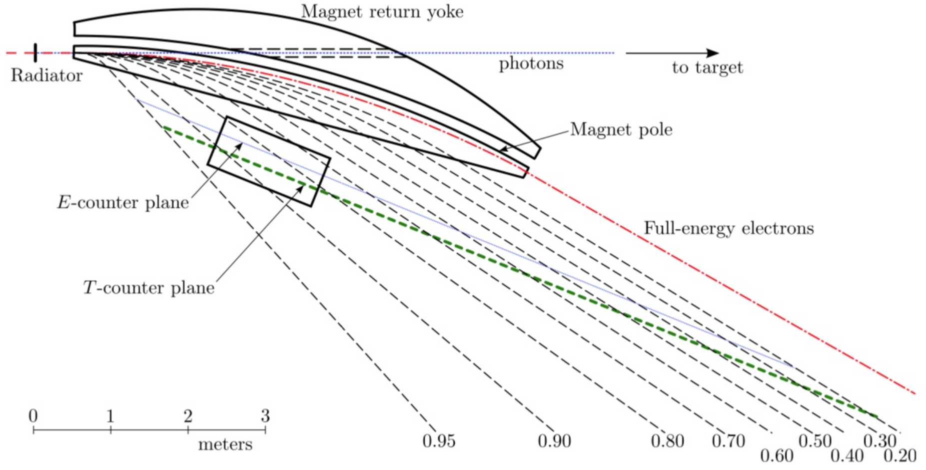

FIG. 9: Diagram of tagger E and T planes.

The tagging system is also used to calculate the event start time. The timing system can identify which RF beam bucket the photon is associated with. This is useful to calculate the event vertex time, which is the time when the final state particles were located in the same physical location, i.e. the event vertex. Complete details of the photon tagging system can be found in [25].

2.4 CEBAF LARGE ACCEPTANCE SPECTROMETER

The CEBAF Large Acceptance Spectrometer (CLAS) detector is located in Hall B. The detector consists of many layers of sub-components. Fig.11 shows a schematic of the detector. The detector was designed based on a toroidal magnetic field, and optimized to measure charged particles with good momentum resolution, geometrical coverage of charged particles to large angles in the laboratory, and keep the region around the target free of a magnetic field magnetic so that dynamically polarized targets can be used. The CLAS Collaboration consists of many institutions throughout the world whose members designed, assembled, commissioned and continue to operate the detector to this day.

The detector is used to measure momenta and angles of outgoing charged particles produced from the interaction of the photon beam with target. The components of the detector are laid out in an onion like pattern surrounding the target, with six visible sectors.

Each component will be briefly described below.

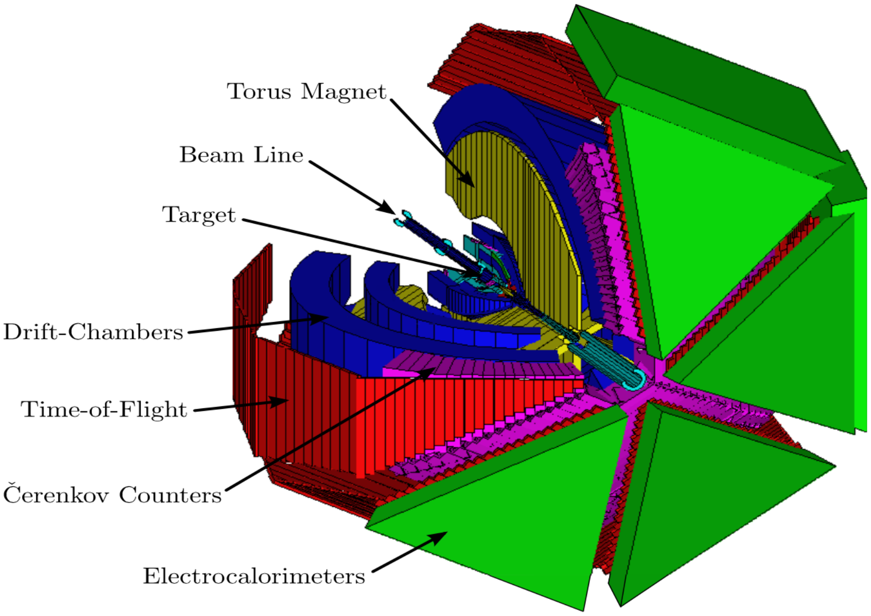

FIG. 10: A schematic of the CLAS detector housed in Hall B at Jefferson Lab.

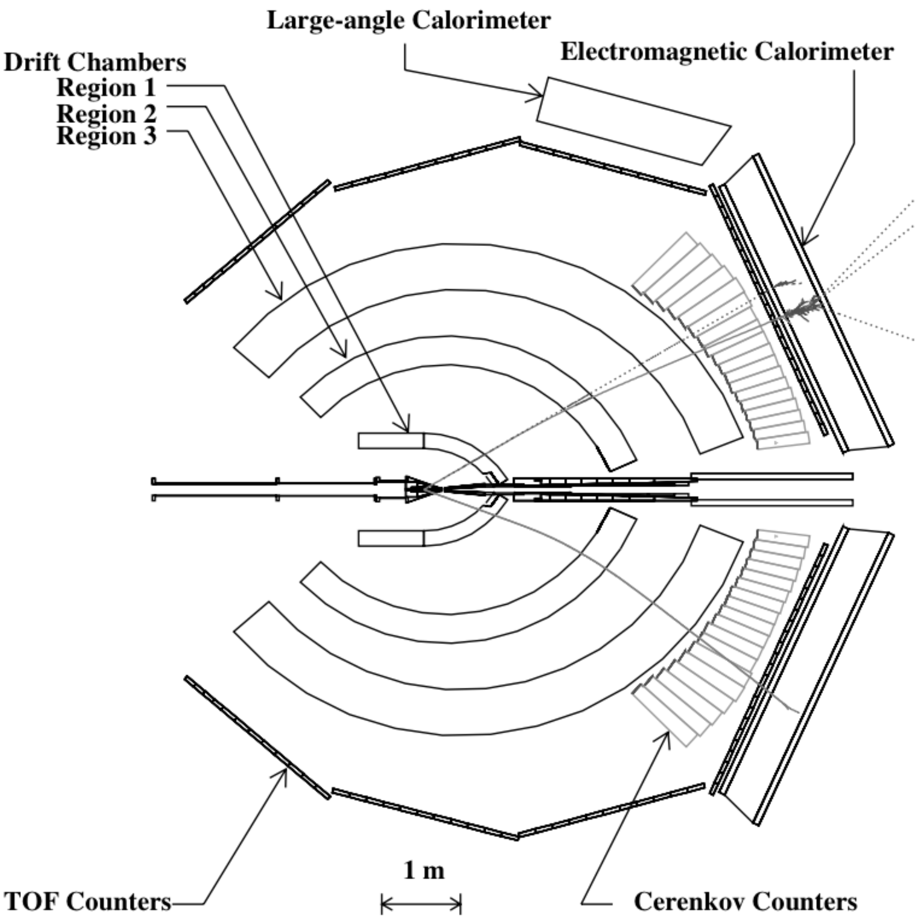

FIG. 11: A top view of the CLAS detector cut along the beam line. Typical photon, electron, and proton tracks are superimposed on the figure.

2.4.1 TARGET

The g11 target cell was cylindrical in shape and made from Kapton by CLAS technician Steve Christo. The target cell is 40 cm long with a radius of 2 cm. The target material was liquid Hydrogen. A schematic of the target cell is shown below.

TABLE 6: Specifications of the cryogenic target

Length	40.0 cm
Radius	2.0 cm
Temperature	19.3 K
Pressure	1122 mBar
Density	0.07177 g/cm^3

FIG. 12: A schematic of the target inside the CLAS detector.

2.4.2 START COUNTER

A new start counter was installed for the g11 run period. The start counter is divided to six sectors each with four scintillator paddles. Each section was made of four 502 mm long straight scintillator paddles with tapered ends that form the 30 mm long nose of the counter. Each paddle was 29 mm wide and 2.15 mm thick and connected to an acrylic light guide which was connected to a photomultiplier tube. The start counter measures the interaction time of incident photons in the target by detecting any charged particle produced in the reaction. The timing resolution is $\approx$ 400 ps. The timing information was included in the Level 1 trigger during the experiment. More details on this detector element can be found in [29].

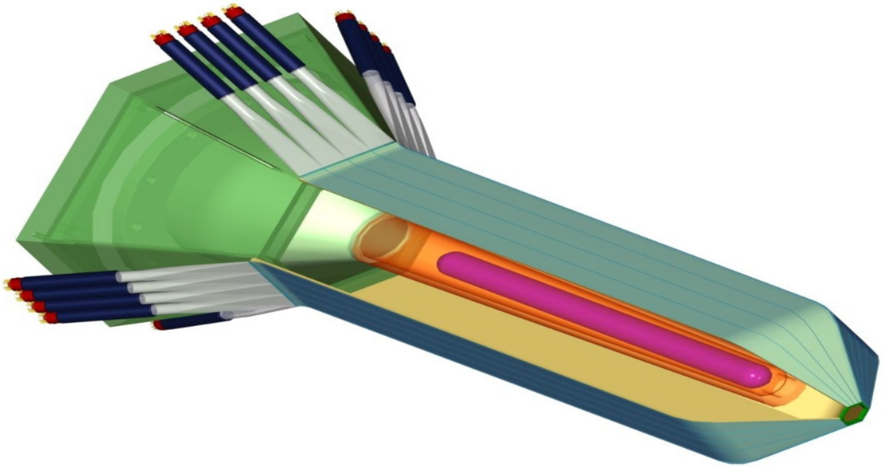

FIG. 13: A schematic of the new start counter installed before the g11 run.

2.4.3 SUPERCONDUCTING TOROIDAL MAGNET

The CLAS detector contained six kidney shaped superconducting toroidal magnets. Each coil is located in its own cryostat. Each coil is about 5 m long and 2.5 m wide with 60° separation in the azimuthal direction. Together, the 6 coils produced an approximately toroidal magnetic field, with the maximum field strength of 3.5 T.

When charged particles encounter magnetic fields, their trajectory is bent. During the g11 experiment, negatively charged particles were bent towards the beam pipe and positively charged particles were bent away from the beam pipe. Running at higher currents provides better momentum resolution but decreases the detector's acceptance for negative particles, it was decided that running at a lower current was the optimal choice. The charged particles in CLAS travel through the drift chambers. When the strength and direction of the magnetic field is known, the trajectory of the particle can be used to determine its momentum.

2.4.4 DRIFT CHAMBERS

In order to determine the momentum of charged particles, the particles must be tracked as they travel through the field generated by the magnet. The particles were tracked using three separate drift chamber regions. Region 1 is located inside the torus coils. Region 2 was mounted directly to the magnet's cryostats, where the magnetic field was the strongest. Region 3 was positioned outside the torus coils. Region 1 and Region 3 are both located where the magnetic field is weak.

Each region of the drift chamber spans the same polar angle range and consists of two superlayers of wires. Each superlayer contains six layers of hexagonal Gold-plated Aluminum alloy field wire cells of 140 μm diameter surrounding 20 μm Gold-plated Tungsten sense wires. The first superlayer had wires along the axial direction (perpendicular to the beamline). The second superlayer has wires tilted at 6° with respect to the axial wires. Together, the information from both superlayers allows us to reconstruct the polar and azimuthal angles. There are 35,148 hexagonal cells in total that can detect charged particles with momenta greater than 0.2 GeV and cover a polar angle range from 8° to 143°. Each drift chamber is filled with a 90% Argon and 10% Carbon Dioxide gas mixture. The gas mixture supports drift velocities of 4 cm/μsec and very high operational voltage.

Charged particles passing through the drift chambers ionize gas molecules. After the gas is ionized, the electrons and ions move towards the sense and field wires, respectively. The hit positions of the initial charged particles is found using the drift time information from the detected signals and hit positions of the initial charged particles. More information about the CLAS drift chamber system can be obtained from [30] and [31].

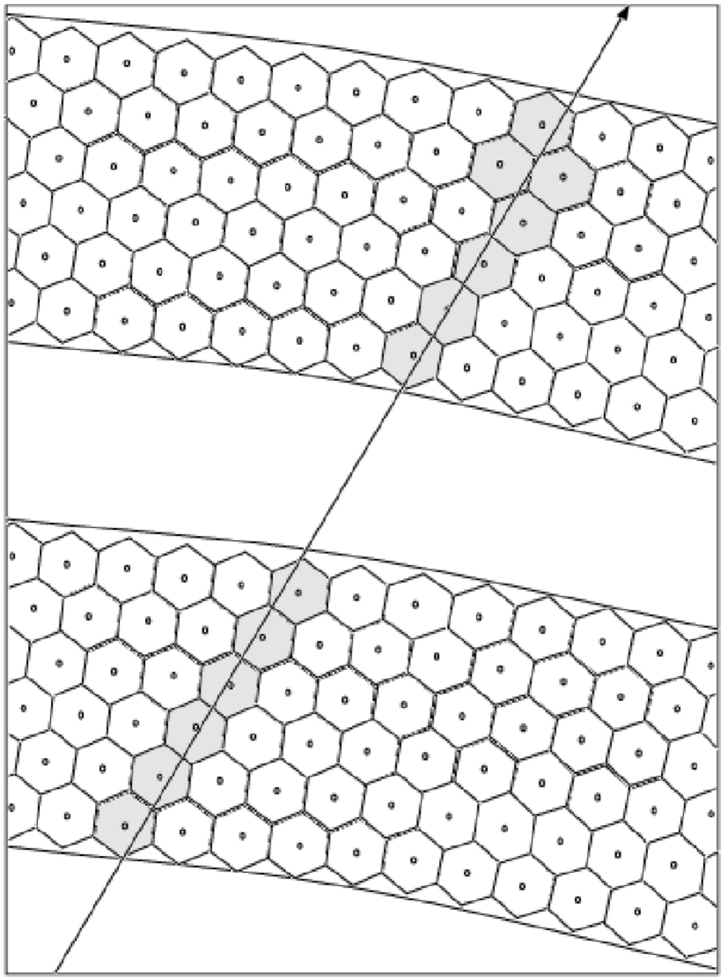

FIG. 14: A schematic of a section of the drift chambers showing two super layers. The wires are arranged in hexagonal cells. The sense wires are located in the center and the field wires are located at each corner of each cell. The track of a charged particle is depicted by the arrow passing through the drift chambers. The shaded hexagons represent hit cells.

2.4.5 TIME-OF-FLIGHT DETECTORS

The next detector element used during G11 consists of six segmented scintillator walls. Each wall has four panels with 57 scintillator paddles with variable lengths of 30 to 450 cm and widths of either 15 or 22 cm. The thickness of the paddles is 5.08 cm. The primary purpose of this TOF system is to measure the arrival time of charged tracks. The timing resolution was 80 to 160 ps, from shortest to longest paddle length, respectively. The timing resolution allows the separation of pions and protons up to a momentum of 2.5 GeV/c.

With the event vertex time measured from the photon tagger, the arrival time gives the total time of flight of the particle through the detector. Once this is known, the speed of the particle is obtained by dividing the path length by the arrival time. Then, knowing the momentum and speed of the particle allows us to compute its mass

$$m = \frac{p\sqrt{1-\beta^2}}{\beta}, \tag{2.4.48}$$

thus identifying the particle. The details of the TOF system can be found in [30].

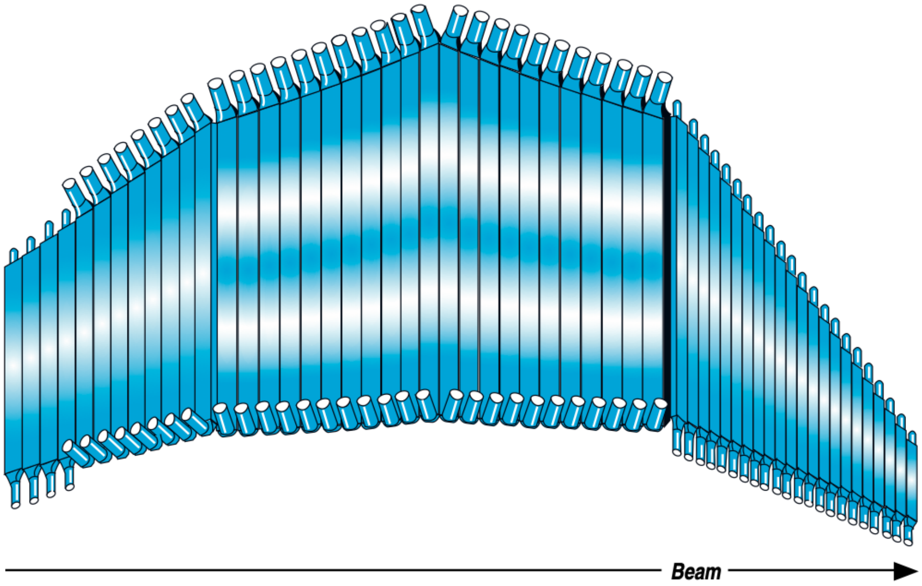

FIG. 15: Section of Time-of-Flight detector system used in each sector of CLAS. Each of the four panels consists of different sized scintillator paddles.

2.4.6 CHERENKOV DETECTORS

When a charged particle moves through a medium faster than the speed of light in that medium, Cherenkov radiation is produced. This is analogous to the shock wave produced by a jet traveling faster than the speed of sound. The gas Cherenkov detectors are used to discriminate between negative pions and electrons for momenta lower than 2.5 GeV *after* passing through the drift chambers. The critical angle, θ_c is defined as

$$\cos\theta_c = \frac{1}{\mathrm{n}\beta}, \tag{2.4.49}$$

where $\beta = v/c$, and n is the index of refraction is unique to each particle.

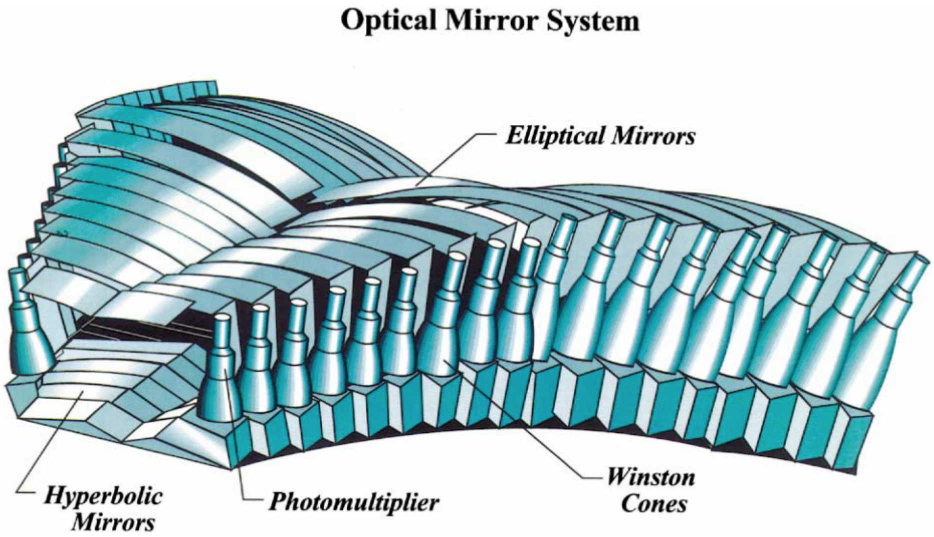

FIG. 16: A schematic of a single Cherenkov Counter showing mirrors and Winston tubes.

The gas used was perfluorobutane (C_4F_{10}. This was chosen due to its high index of refraction (1.00153) which produces a higher yield of photons. The minimum energy for a pion to produce Cherenkov radiation in this material is 2.7 GeV, while for electrons it is 9.2 GeV. Complete details of the CLAS Cherenkov detector can be found in [26].

2.4.7 ELECTROMAGNETIC CALORIMETERS

The electromagnetic calorimeters are used to identify electrons above 0.5 GeV and photons above 0.2 GeV. It is primarily used for reconstructing the radiative decays of the π^0 and η mesons, but is also used for leptons and neutral particles. The calorimeter is constructed of 39 layers consisting of alternating lead sheets and scintillator bars. The scintillators are arranged in three views, called U, V, and W, that allow for electromagnetic showers to be spatially located by the pixels created with the overlapping layers. The design of the calorimeter was such that the following conditions could be achieved:

1. e/γ energy resolution σ/E $\leq 0.1/\sqrt{E(GeV)}$;
2. position resolution $\delta r \approx 2$ cm at 1 GeV;
3. π/e rejection greater than 99% at $E \leq 1$ GeV;
4. fast ($<$ 100 n) total energy sum for the event trigger;
5. mass resolution for two photon decays δm/m $\leq$0.15;

6. neutron detection efficiency $> 50\%$ for $E_n > 0.5$ GeV;

7. time of flight resolution ≈ 1 ns.

More information on the electromagnetic calorimeters can be found in [32].

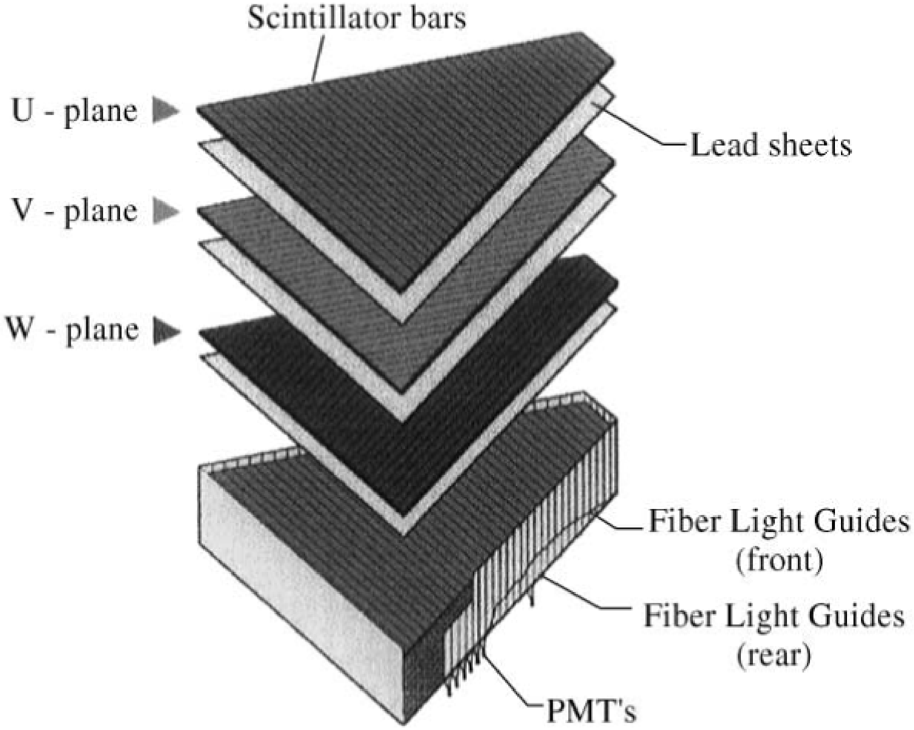

FIG. 17: View of the electromagnetic calorimeters U, V, and W planes.

2.5 BEAM LINE DEVICES

Aside from the CLAS detector, Hall B houses more instruments for various purposes. Upstream from the detector these instruments include: beam position monitors, harps, and current measuring devices to monitor the quality of the beam. Downstream, the total absorption shower counter, pair spectrometer, and pair converter are used to measure the photon flux incident on the target. A brief description of these instruments is given below.

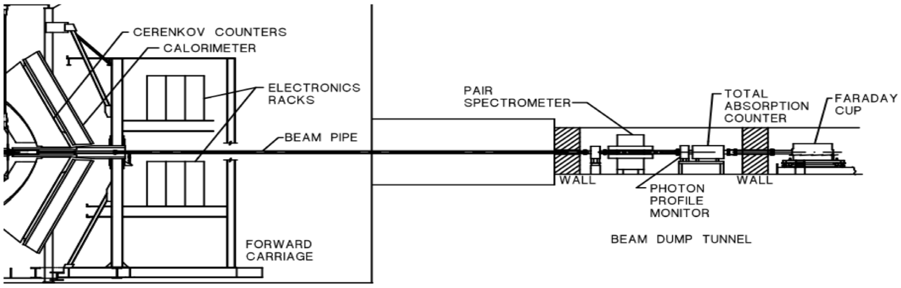

FIG. 18: Beamline components downstream of the CLAS detector.

2.5.1 BEAM POSITION MONITORS

Beam Position Monitors are used to monitor the x and y position with a resolution of less than 0.1 mm and a current measurement. The BPM's reported the beam position at a rate of 1 Hz. The BPMs were located at 36.0, 24.6, and 8.2 m upstream from the target [33].

2.5.2 HARPS

Harps allow the beam profile to be studies. They consist of a pair of wires oriented to scan the beam profile in orthogonal directions. These wires are made from both Tungsten and Iron. The position of the harps are located at 36.7m, 22.1m, and 15.5m upstream from the target. Electrons scattered by the harps were detected by an array of PMT detectors downstream from the location of the harps. More information on the harps can be found in [33].

2.5.3 TOTAL ABSORPTION SHOWER COUNTER

The TASC was used to obtain the photon flux at beam currents lower than 100 pA. During production data taking, the TASC was removed from the beamline and reinserted during the lower-intesity normalization runs.

It consisted of four lead glass blocks made of 55% PbO and 45% SiO_2 with a radiation length of 2.36 cm. The blocks were (10x10x40) cm and were mounted in a 2x2 array. Each block contained a Philips XP4312B phototube. More information about the TASC can be found in [33].

2.5.4 PAIR SPECTROMETER

The pair spectrometer was used to measure the photon flux at higher beam intensities than that of the TASC. The pair spectrometer consisted of a large aperture dipole magnet, an aluminum converter, and an array of eight scintillator paddles. As photons struck the converter, they produced e^+e^- pairs which were then swept out of the beam line and directed towards the scintillator paddles. The converters had a radiation length of 1% or 2%. The scintillators were positioned so that the spectrometer would detect e^+e^- pairs over the full energy range of the tagger spectrometer.

The pair spectrometer remained in the beam line during higher intensity runs of up to several nano amps, in contrast with the TASC.

Fig. 19 displays a top view of the upstream beam line components and their location relative to the CLAS detector.

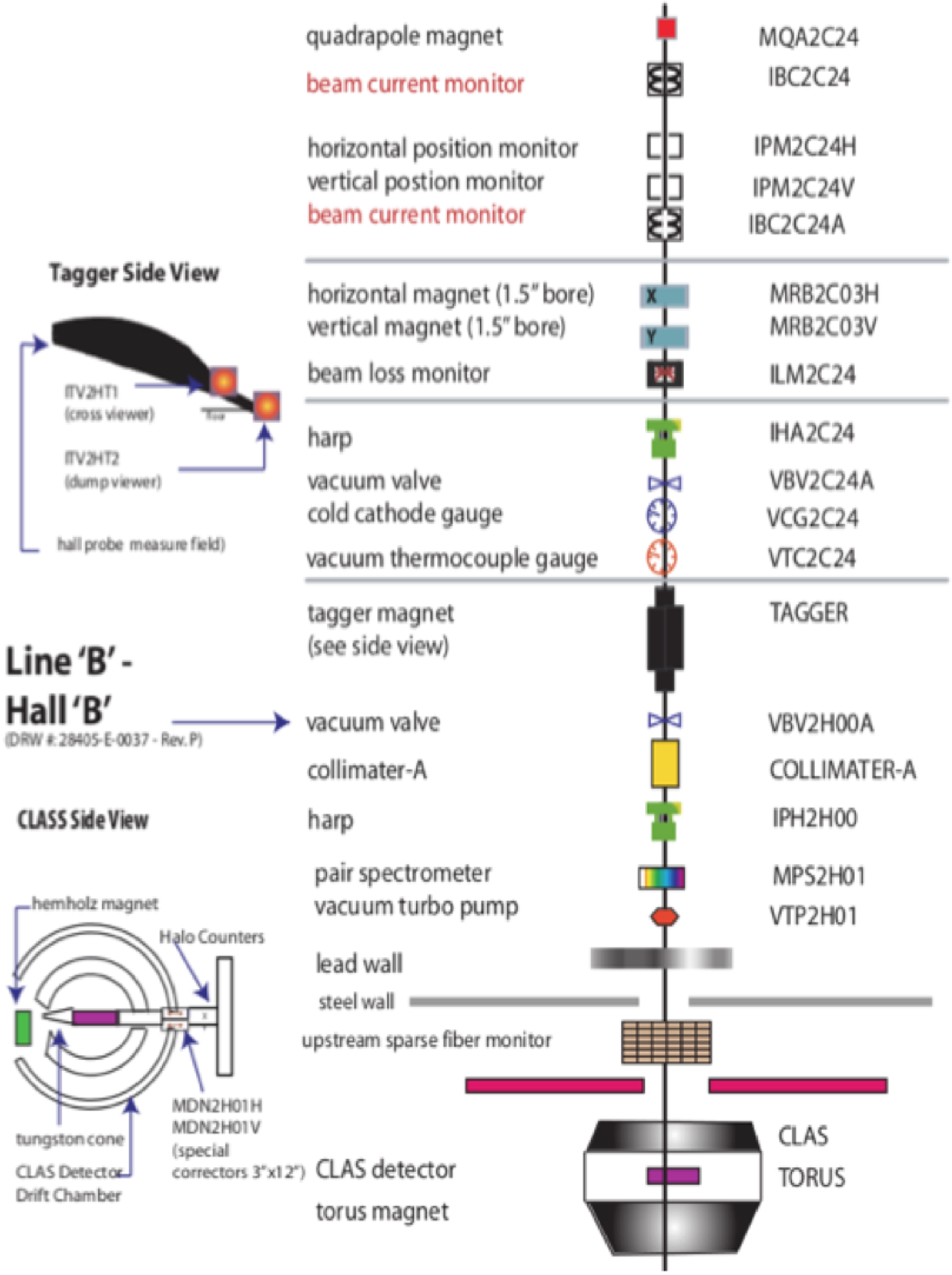

FIG. 19: Beamline components in Hall B.

2.6 DATA ACQUISITION

Signals from each detector system are read out by electronic crates that convert the analog signals into digital signals. Analog to Digital Converters (ADCs) are used for signal amplitude while Time to Digital Converters (TDCs) are more sensitive to the signal rise or fall time. Triggers are used to separate real physics events from electronic signals from other sources, such as cosmic radiation or electronic noise. Once there is a trigger, the DAQ collected the signals and wrote them to magnetic tape for analysis.

Once an event satisfies the level 1 trigger, the DAQ is gated and begins to read the event. Signals from the detector elements in CLAS are digitized and then read out by 24 VME readout controllers, known as ROC's. Then, data tables from the various systems were sent to the CLAS online acquisition computer in the control room. The Event Builder associates the tables into banks, and then packaged the event into its final form before storing it in a shared memory bank. For the g11 run period, events were selected using information from the tagger, start counter, and the time-of-flight scintillators. Events were recorded when both the tagger Master OR (MOR) and the CLAS Level 1 hardware trigger fell within a timing window of 15 ns. The Level 1 trigger required a signal from any of the 4 start counter paddles and any of the 48 TOF paddles from two separate sectors of CLAS within 150 ns.

2.7 THE G11 EXPERIMENT

The g11 run period was part of experiment E04021, *Spectroscopy of Excited Baryons with CLAS: Search for Ground and First Excited States* was conducted in Hall B during the summer of 2004. The goal for the experiment was to search for the Θ^+ pentaquark state. As a result, data for a number of different final states was obtained. The process of calibrating the subsystems of CLAS and converting the raw information into events containing tracks with momentum and timing information is called cooking. Cooking was done by Maurizio Ungaro. The process is described in [34].

2.7.1 BEAM ENERGY

The electron beam energy during the g11 experiment was 4.017 GeV. Towards the end of the run period, an additional 26 runs were collected with a beam energy of 5.021 GeV. The data analyzed in this work does not include the runs at 5.021 GeV. The photon beam energy for the g11 experiment ranges from 1.5 to 3.5 GeV.

2.7.2 G11A TRIGGER

The trigger was chosen specifically to maximize multi-track event detection in CLAS. The trigger required at least 2 charged tracks in different sectors of the TOF system within a 100 ns timing coincidence window. In addition, two hits in the Start Counter matching the sectors of the TOF hits within a 15 ns timing window were required. The MOR from the photon tagger was required as well. The photon tagger was only triggered on the first 40 of the 61 T-counters, which preferentially selected events originating from higher energy photons.

2.8 EXCLUDED RUNS

Data taken during the g11a run period was grouped into runs, which consist of 10M events per run. The g11a run period includes runs 43490 to 44133. Runs 43490 to 44107 were taken with the electron beam energy equal to 4.019 GeV, while runs 44108 to 44133 were taken with an electron beam energy of 5.021 GeV. Only runs 43490 to 44133 are included in this analysis. In addition, runs 43490 to 43525 were commissioning runs and are not used for physics analysis. The table below lists additional runs that are not included in our analysis:

Run	Description
43490-43525	Commissioning Runs
43586-43596	TOF Problem in Sector 3
43675-43778, 44013	Different Trigger Configuration
43871	Data Processing Error
43981-43982	Logbook Lists DC Problems
43989-43991	Logbook Lists DAQ Problems
44000-44002, 44007-44008, 44010-44012	TOF Problem in Sector 2
44108-44133	5.021 Beam Energy

TABLE 7: g11a cooked runs that are not included in physics analysis

2.9 EVENT SELECTION

Events were required to have three charged tracks in the final state identified as a proton, π^+, and π^- and a photon tagged by an electron in the tagger. Charged particles were identified using the CLAS Simple Event Builder (SEB) package. The SEB package calculates the velocity of the detected particle and compares it with an expected velocity corresponding to the measured momentum and the masses of the different particle candidates. The particle is chosen based on the minimum difference between the measured and candidate velocities. The final state photon is identified by having an energy deposition in the ECAL without a corresponding charged track and simultaneously having $\beta > 0.9c$. To suppress accidental coincidences from different beam bunches, there is an additional requirement to have only one photon present in the tagger within the ± 2 ns time interval between the tagger and the start counter, i.e. $|ST_{time} - TAG_{time}| < 2$ ns.

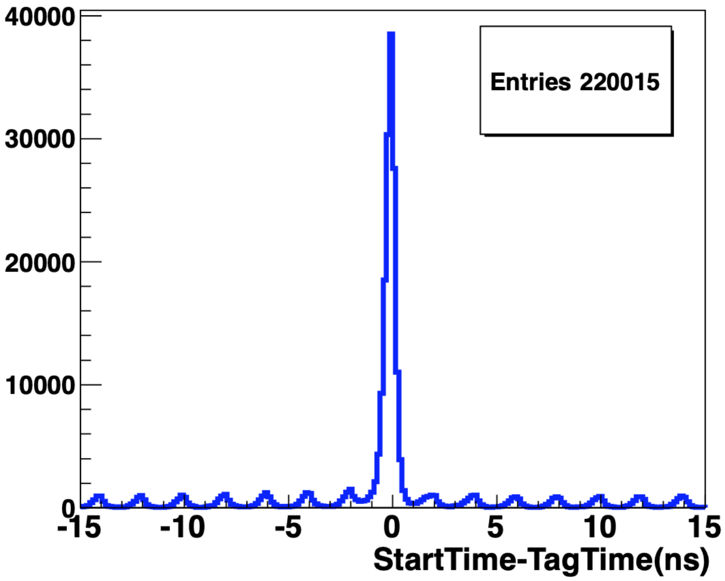

FIG. 20: Tagger time subtracted from the event start time. Image from [41].

This cut ensures we choose the correct photon in the case that multiple photons were detected close to the event start time. An additional cut was required that each event only have one photon detected in the tagger during the 2 ns interval.

CHAPTER 3

DATA ANALYSIS

This chapter describes the corrections applied to the raw data, including the standard CLAS corrections involving Tagger Energy, Energy Loss, and Momentum corrections. The CLAS detector performance cuts are discussed. After applying the standard CLAS cuts, there are kinematic cuts that are applied which are specific to our analysis. We describe the method used to extract our signal events and then describe the standard CLAS software packages used for simulations.

3.1 CORRECTIONS

This section summarizes the corrections applied to the g11 data set. These were discovered either during or after data was take and subsequently applied to our skimmed data set. These corrections were not applied to the Monte Carlo data.

3.1.1 TAGGER ENERGY CORRECTIONS

Alignment issues in the photon tagger's focal plane lead to an inaccurate photon energy constructed from the raw trigger information. The alignment issues arise because of the sagging of the tagger under gravity. As a consequence, there is a deviation between the proton mass and the missing mass of the $\gamma p \rightarrow K^+K^-X$ reaction, $\Delta M = M_X - M_P$. This shift is visualized in Fig. 21. The deviation was dependent on the run number and was corrected on a run-by-run basis. The correction factor on average was $R = E_{corrected}/E_{initial} = 1.005$, which indicates the reported beam energy was about 0.5% less than the actual value.

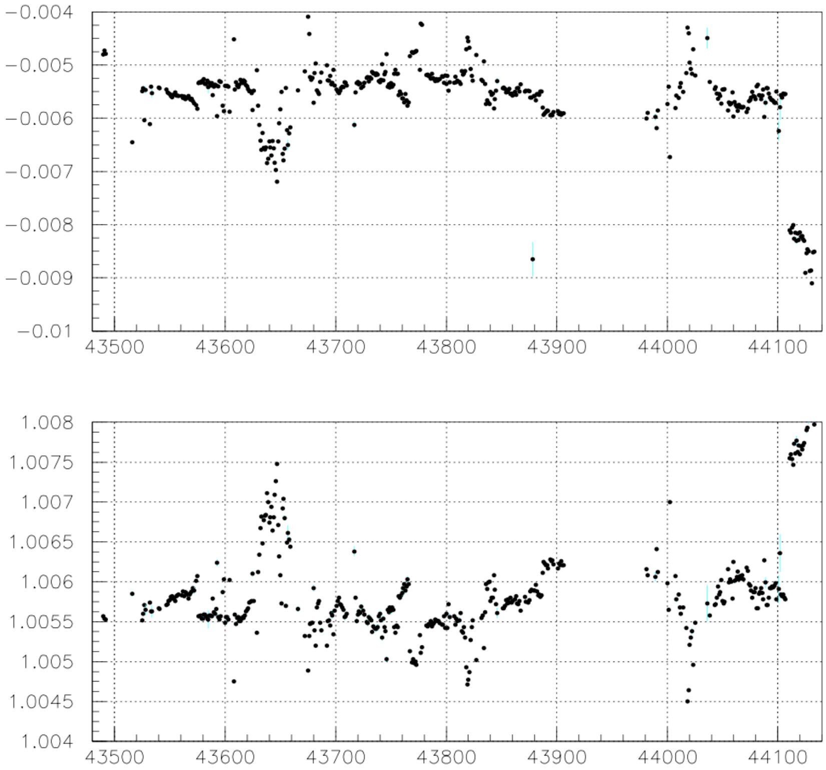

FIG. 21: Upper Panel: Missing mass shift as function of run number. Lower panel: photon energy corrections as a function of run number. Image from

The photon energy corrections were checked using $\gamma p \rightarrow \pi^+\pi^- X$. After the corrections were applied, the proton mass was shifted to the correct value. The tagger energy corrections as a function of the Tagger ID are shown in 22. The red line corresponds to the corrections before electron energy corrections. After the electron energy corrections the photon energy is shifted by 0.5%. The black curve confirms that after the electron beam energy corrections and tagger corrections are applied, the missing proton mass has the correct value.

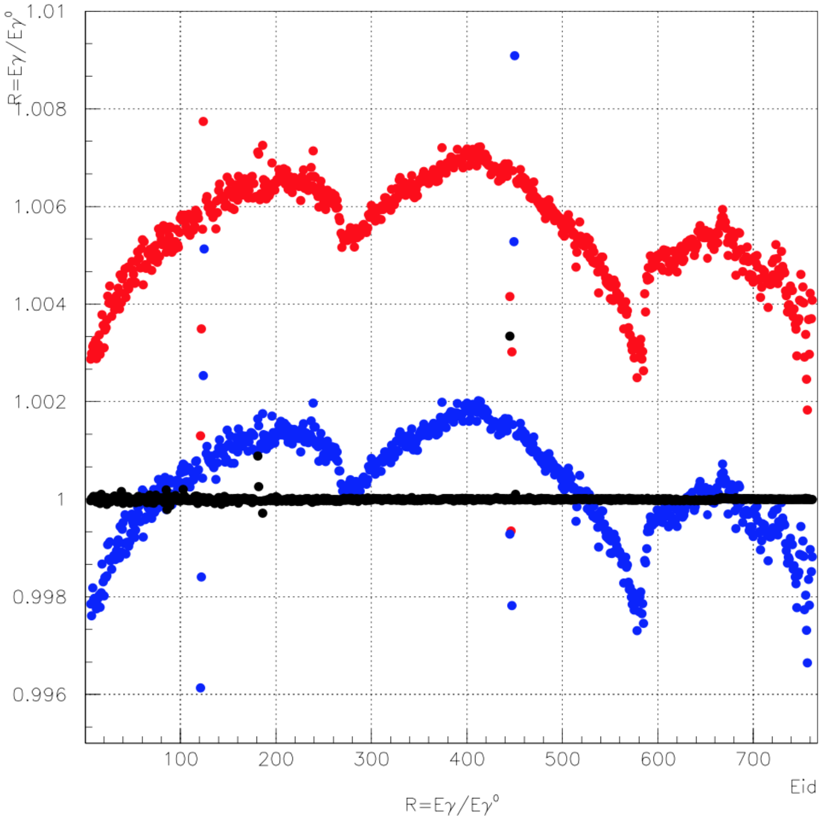

FIG. 22: Tagger energy correction as function of Tagger ID. Red (blue) line corresponds to the corrections before (after) electron energy corrections. Image from

The inconsistent points correspond to cable swaps. This was discovered during the photon energy calibration after the data taking was completed. They were accounted for via a correction procedure from [35].

3.1.2 ENERGY LOSS CORRECTIONS

Particles traveling through materials lose energy primarily due to excitation and ionization. Corrections were derived to account for energy loss in the target, the beam pipe, the start counter, and the air gap between the start counter and the Region 1 drift chambers. The corrections were applied with the CLAS Eloss package written by Eugene Pasyuk [27]. For the g11 experiment, this was modified to include the geometry of the target and new start counters.

3.1.3 MOMENTUM CORRECTIONS

Discrepancies in the toroidal magnetic field map and/or in the drift chamber survey information can lead to inaccuracies in the reconstructed momenta. The momentum corrections used in this analysis were derived by Valery Kubarovksy [35]. The corrections were determined using the missing mass technique. The reactions $\gamma p \rightarrow \pi^+\pi^- p$ and $\gamma p \rightarrow K^+K^- p$ were used to extract the corrections as a function of the ϕ angle, after the energy loss and tagger corrections were applied. They are individually calculated for π^+, π^-, K^+, K^-, and protons.

The corrections for the π^+ and π^- are obtained from $\gamma p \rightarrow \pi^+\pi^- p$ inclusive reaction, requiring only one of each final state particle, and for the K^+ and K^- from the $\gamma p \rightarrow K^+K^- p$ reaction again with only one of each particle in the final state. The correction factors are on the order of ±1% for ϕ and are much smaller for θ and P and are thus ignored. Fig.23 shows the momentum corrections for positive particles as a function of ϕ. Fig. 24 shows the corrections for negative particles.

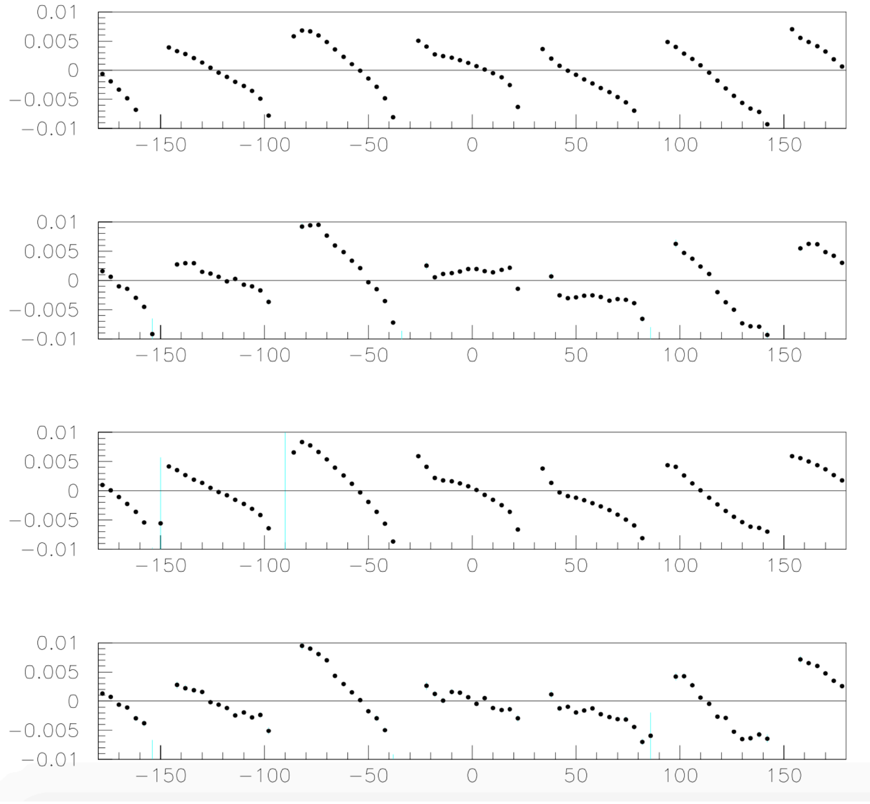

FIG. 23: Momentum corrections, $R = P_{corrected}/P_{measured} - 1$, as a function of ϕ for positive particles estimated from the missing mass distributions in $\gamma p \rightarrow \pi^+\pi^- p$ reaction for π^+, protons, and for K^+ and protons from $\gamma p \rightarrow K^+K^- p$. Figure taken from [35].

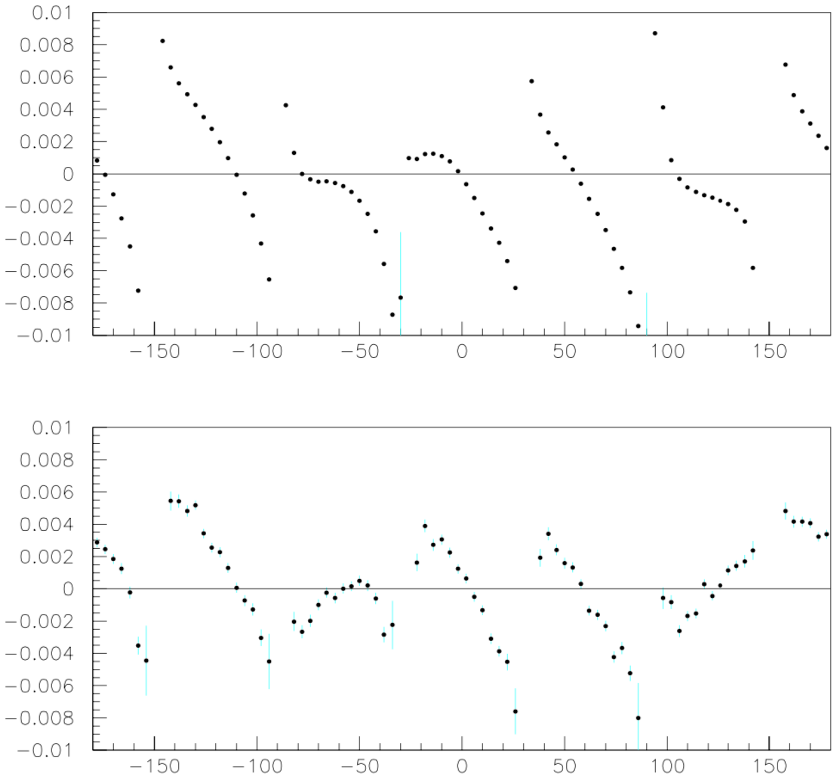

FIG. 24: Momentum corrections, $R = P_{corrected}/P_{measured} - 1$, as a function of ϕ for negative particles K^- and π^-. Figure taken from [35].

Since the corrections involved reactions and final states different from the one under study, it is important to determine the dependence of η as a function of θ_P, E_{beam}, and P_P. With no dependence on these quantities, the η signal should appear as a flat band. This is shown in Figs. 25-27.

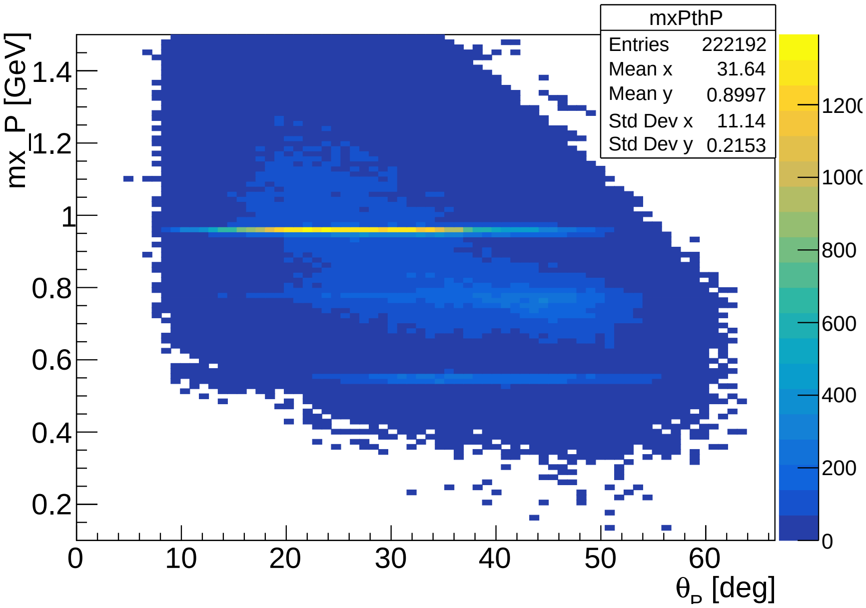

FIG. 25: $m_x(P)$ as function of θ_P. The signal of η appears as a flat band around 0.547 GeV.

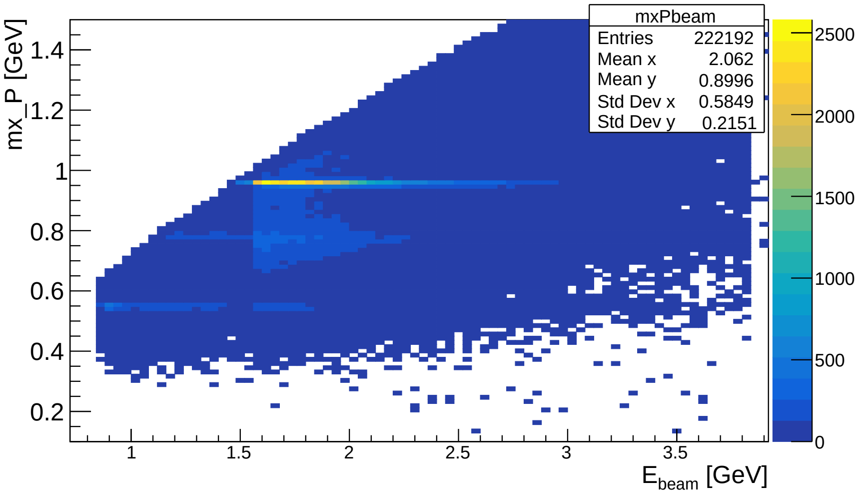

FIG. 26: $m_x(P)$ as function of E_{beam}. Note the minimum beam energy for g11 was 1.51 GeV. The η signal appears as a flat band around 0.547 GeV.

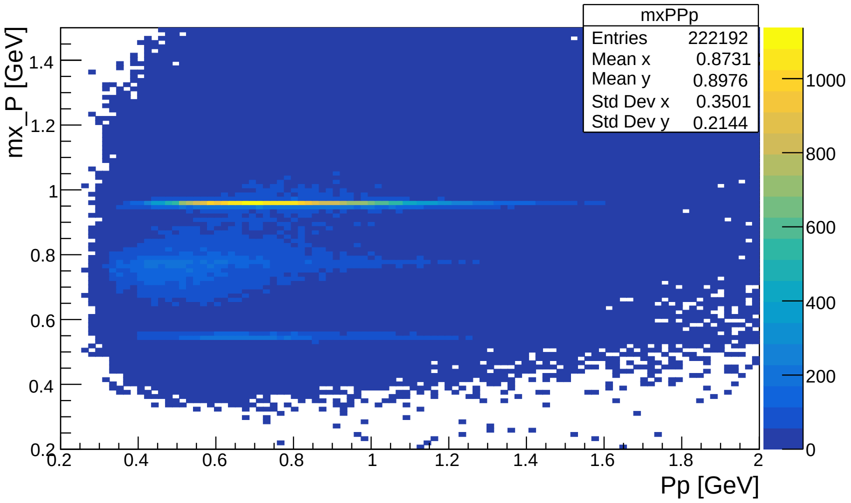

FIG. 27: $m_x(P)$ as function of θ_P. The η signal appears as a flat band around 0.547 GeV.

Since the η signal appears as a flat band, it is evident our signal peak does not depend on the beam energy, θ_P or momentum of the proton, as expected.

3.2 DETECTOR PERFORMANCE CUTS

This section summarizes the cuts on the data related to the CLAS detector itself.

3.2.1 MINIMUM MOMENTUM CUTS

Protons with low momentum are difficult to model in CLAS because they lose a significant amount of energy as the pass through material in the detector. Matt Bellis, a post-doctoral researcher at Carnegie Mellon University, performed a study that compared the acceptance of the data and Monte Carlo using the reaction $\gamma p \rightarrow p\pi^+\pi^-$. An acceptance asymmetry, defined as:

$$A = \frac{|A_{data} - A_{mc}|}{A_{data} + A_{mc}} \tag{3.2.50}$$

was calculated. This quantity should be zero. Fig. 28 shows this quantity for protons. In most areas, the data and MC acceptances are equal except in the very forward region and for low momentum protons, thus these regions are cut.

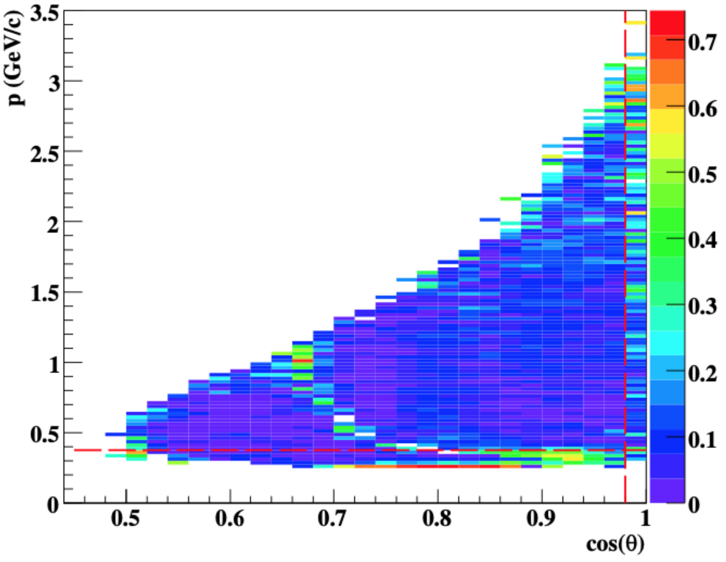

FIG. 28: Acceptance asymmetry vs p (GeV/c) and $\cos\theta$ for protons. The vertical dashed line indicates a cut $\cos\theta = 0.985$ and the horizontal dashed line indicates a cut at $p = 375 MeV/c$. The curved segment corresponds to a bad TOF paddle.

For our specific analysis, the low momentum proton cut was placed at $P_p = 350$MeV. For the charged pions, a minimum momentum cut is placed at P_{π^+} and $P_{\pi^-} > 0.1$ GeV.

3.2.2 TOF PADDLE KNOCK OUTS

Dead time-of-flight particles were removed if they had noticeable discrepancies for pions and/or protons. The paddles were identified by examining occupancy plots of both the data and Monte Carlo. Table 3.2.2 summarizes the knocked out paddles for each sector.

TABLE 8: Bad time-of-flight paddles that were not used for analysis.

Sector	Knocked Out Paddles
1	18,26,27,33
2	none
3	11,24,25
4	26
5	20,23
6	25,30,34

3.3 KINEMATIC CUTS

After the corrections, we can plot the missing mass of the proton from the reaction $\gamma p \to pX$ from our data. In Fig. we see three peaks corresponding to the η, ρ/ω, and the η' mesons as identified by their mass, demonstrating that particle X in the reaction above could have been the mesons shown.

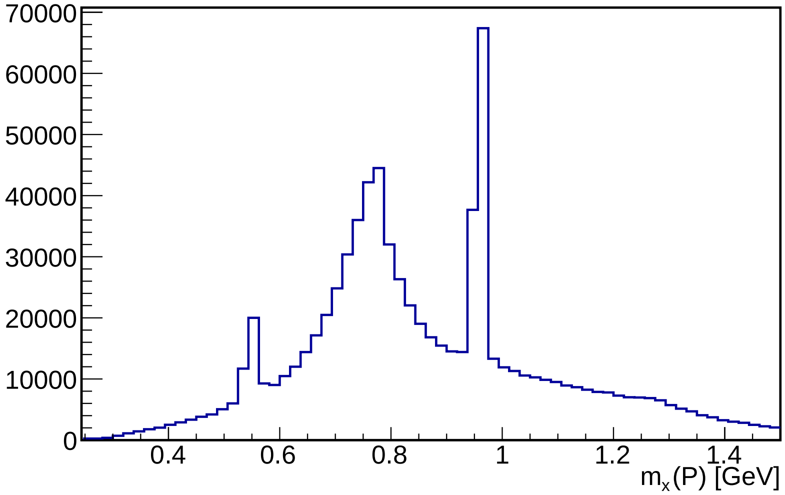

FIG. 29: Missing mass of the proton, $m_x(P)$, showing the η, ρ, and η' peaks, respectively. We required $|m_x^2(P\pi^+\pi^-\gamma| < 0.0005$ and $|m_x^2(P\pi^+\pi^-)| < 0.005$.

To identify the $\pi^+\pi^-\gamma$ final state from the decay of η meson we require the squared missing mass of all final state particles to be around zero, $|m_x^2(P\pi^+\pi^-\gamma)| \leq 0.0005\ GeV^2$. This exclusivity cut ensures there are no other particles in our desired final state. This is shown in Fig. 30. To select the mother particle of interest, in this case eta, we require the missing mass of the proton to be $|m_x(P) - M_\eta| \leq 0.03\ GeV$. This cut corresponds to approximately 2.3σ obtained from the fit of $m_x(P)$. Furthermore, we require the missing mass of all charged particles to be $|m_x^2(P\pi^+\pi^-)| < 0.005\ GeV^2$, shown in Fig. 31. This ensures we are looking at reaction $\eta \to \pi^+\pi^-\gamma$ and not $\eta \to \pi^+\pi^-\pi^0$. Fig. 32 shows the signal of η with the vertical bars showing our defined signal region.

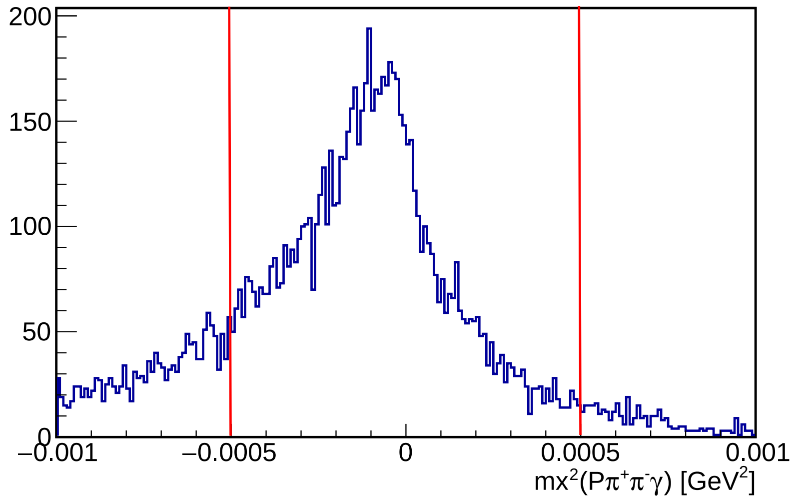

FIG. 30: Missing mass squared of all final state particles, $m_x^2(P\pi^+\pi^-\gamma)$. The cut value used in this analysis is $|m_x^2(P\pi^+\pi^-\gamma)| < 0.0005$ GeV^2.

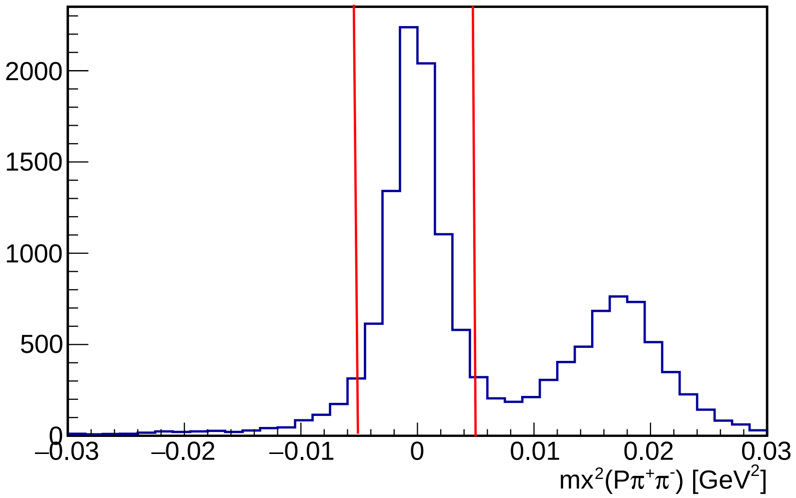

FIG. 31: Missing mass squared of proton, π^+, and π^-, $m_x^2(P\pi^+\pi^-)$. In order to separate the photons from π^0, we select the region $|m_x^2(P\pi^+\pi^-)| < 0.005$ GeV^2.

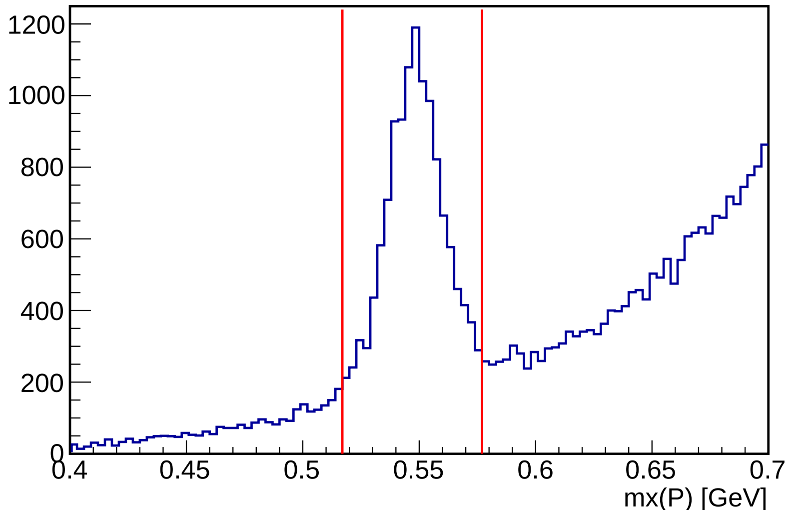

FIG. 32: Missing mass of the proton, $m_x(P)$ showing the η peak. Cut value used to select η region is $|m_x(P) - M_\eta| < 0.03$ GeV.

In addition to the cuts mentioned previously, we require the missing energy of the proton, π^+, and π^- and the momentum of the outgoing photon to be greater than 0.1 GeV. This cut is based on the threshold of the ECAL photon detection threshold of 75 MeV. We require the difference between these two cuts to be small, ensuring that the missing energy of the three particles match the momentum of the outgoing photon.

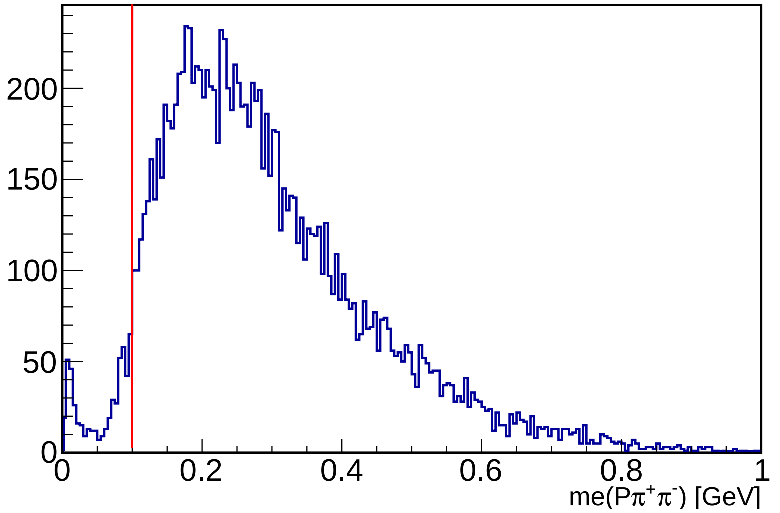

FIG. 33: Missing energy of proton, π^+, and π^-. Cut value is me($P\pi^+\pi^-$) > 0.1 GeV.

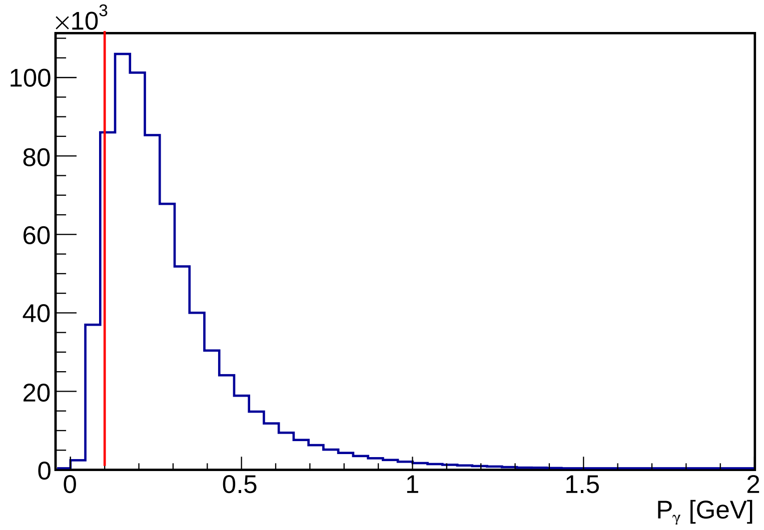

FIG. 34: Momentum of outgoing photon. Cut value is $P_\gamma > 0.1$ GeV

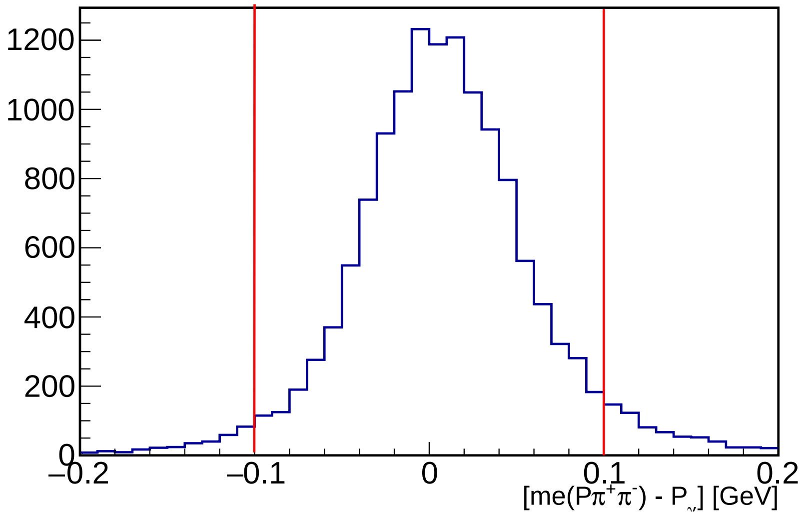

FIG. 35: Difference of missing energy of the proton, π^+, π^- and P_γ. The cut value used in this analysis is $|me(P\pi^+\pi^-) - P_\gamma| < 0.1$ GeV.

An additional cut has been placed on θ_γ to be in the range of 15-45 deg. This is shown in Fig. 53. For this analysis, all relative cuts were applied to each variable excluding the cut on the variable itself.

3.4 RECONSTRUCTING η

We first check to see if we can resolve the peak of η from the missing mass of the proton in each bin of $IM(\pi^+\pi^-)$ since the two pion invariant mass spans the range from $[2m_\pi, m_\eta]$. The invariant mass is binned in 21, 10 MeV wide bins. This is shown in Fig. 39 - 42. There is a clear signal of η in all bins except those larger than $|IM(\pi^+\pi^-) - 0.505| < 0.05$, therefore we exclude those in our analysis.

3.4.1 SIDEBAND SUBTRACTION

Sideband subtraction is a method used to subtract the background under a signal. In principle, it requires at least two variables: the variable of interest and the separation variable. In our case, our variable of interest is the squared missing mass of the proton, π^+, and π^-, labeled as $m_x^2(P\pi^+\pi^-)$ while our separation variable is the missing mass of the proton, m_xP. The separation variable is used to separate the background from the signal region using the regions away from the Gaussian peak, called sidebands. The sideband regions must be chosen such that they are sufficiently far from the η peak, not in the region of another resonance, and with the sum of the two sideband regions equal in width to the signal region.

The procedure is as follows. First, a plot of $m_x^2(P\pi^+\pi^-)$ is produced with a cut on the m_xP in the sideband regions. Then, the $m_x^2(P\pi^+\pi^-)$ is plotted with a cut on m_xP from the signal region, which includes signal (S) and background (B) events. Then, we integrate the sideband and signal regions and calculate the ratio $R = A_{signal}/A_{sidebands}$. Once this ratio is obtained, the events in $m_x^2(P\pi^+\pi^-)$ are scaled by the ratio R. This gives an estimate of the number of background events under the signal peak. Finally, this weighted histogram is subtracted from the $m_x2(P\pi^+\pi^-)$ obtained from the signal region of $m_x(P)$. An example construction for one bin is provided below.

For each bin of $IM(\pi^+\pi^-) \in [0.305, 0.505]$, if the η peak is present, we fit the distribution with a Gaussian and linear background polynomial and estimate the number of background events in the signal and sideband regions. We show the η signal as postage stamp plots in Fig. 39 - 42. An example fit is shown in Fig. 37 for the bin corresponding to $|\text{IM}(\pi^+\pi^-) - 0.345| < 0.005$. Fits for all bins are shown in the Appendix.

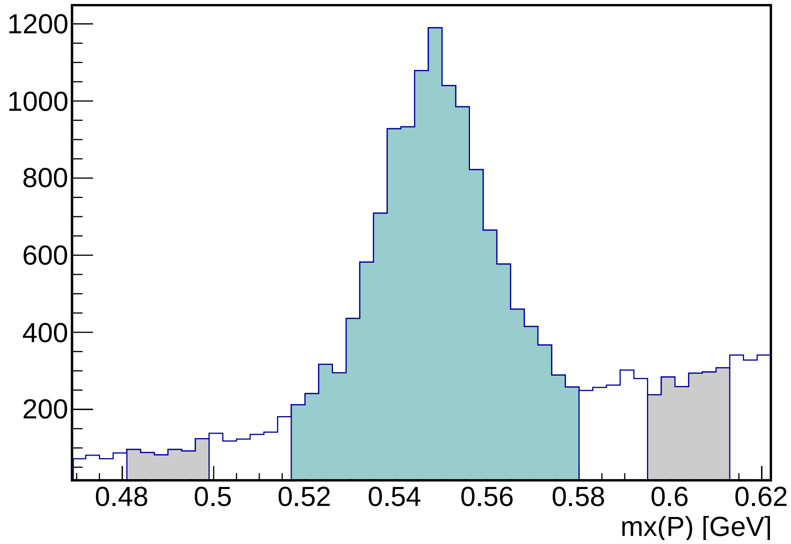

FIG. 36: Missing mass of the proton with signal (green) and sideband regions (grey) labeled.

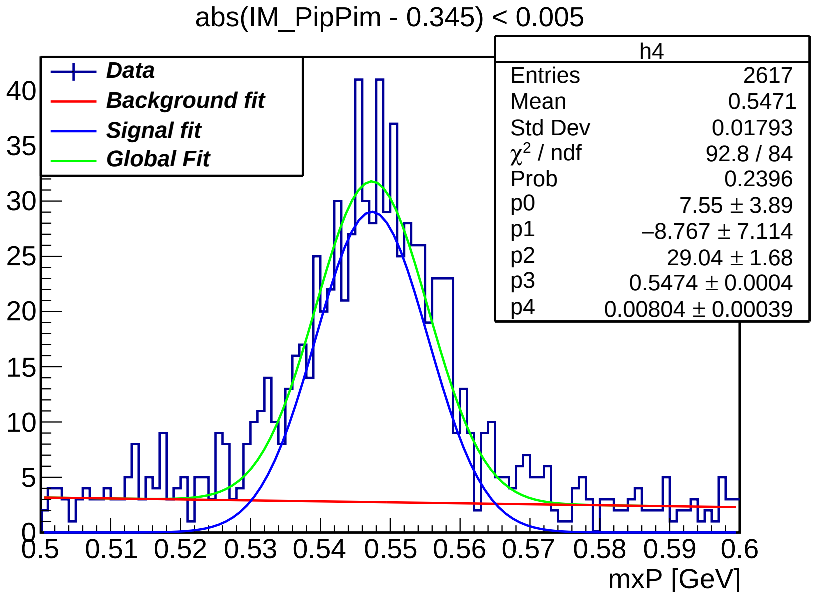

FIG. 37: Missing mass of the proton for $|\mathrm{IM}(\pi^+\pi^-) - 0.355| < 0.005$ GeV. The total fit function is in green, the background polynomial is red, and the Gaussian signal is blue. The number of events in the signal and sideband regions was obtained via integrating the total function in the three respective regions.

The signal region is defined as $|m_x(P) - M_\eta| < 0.03$ GeV. The sideband regions are chosen to be from $|m_x(P) - 0.490| < 0.0075$ GeV and $|m_x(P) - 0.604| < 0.0075$ GeV. The number of background events in the signal region, containing both signal and background events, and the number of events in the sideband regions is obtained. They are denoted as A_{peak}, A_{left}, and A_{right}.

$$A_{region} = \frac{1}{BW} \int_{M_l}^{M_h} (a_0 + b_0 m) dm \tag{3.4.51}$$

where M_h and M_l denote the upper and lower limits of the defined mass region. We then plot $m_x^2(P\pi^+\pi^-)$ from the signal region of η, labeled Φ_{signal} and from the left and right sideband regions, labeled $\Phi_{sidebands}$. An example bin is shown in Fig. 38. The left most peak corresponds to the photon peak, while the other peak visible in lower $IM(\pi^+\pi^-)$ bins corresponds to neutral pions. The sideband subtraction is then performed in each bin using the following:

$$\Phi_{sub} = \Phi_{signal} - \frac{A_{peak}}{A_{left} + A_{right}} \Phi_{sideband}, \tag{3.4.52}$$

and is shown in for all bins are shown in Fig. 43-47.

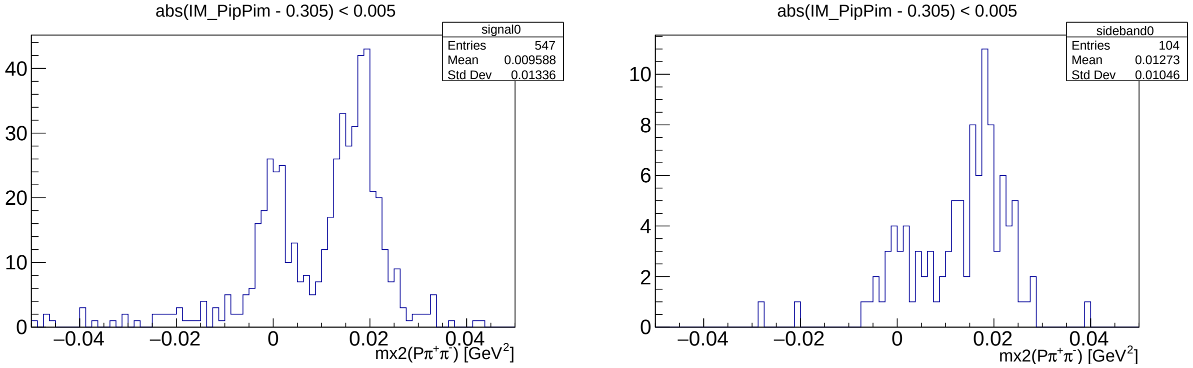

FIG. 38: Left plot: $m_x^2(P\pi^+\pi^-)$ from the signal region of η, $|m_x(P) - 0.547| < 0.03$ GeV. Right plot: same as left but from the sideband regions of η, $|m_x(P) - 0.490| < 0.0075$ GeV and $|m_x(P) - 0.604| < 0.0075$ GeV. The invariant mass bin selected is $|IM(\pi^+\pi^-) - 0.345| < 0.005$ GeV.

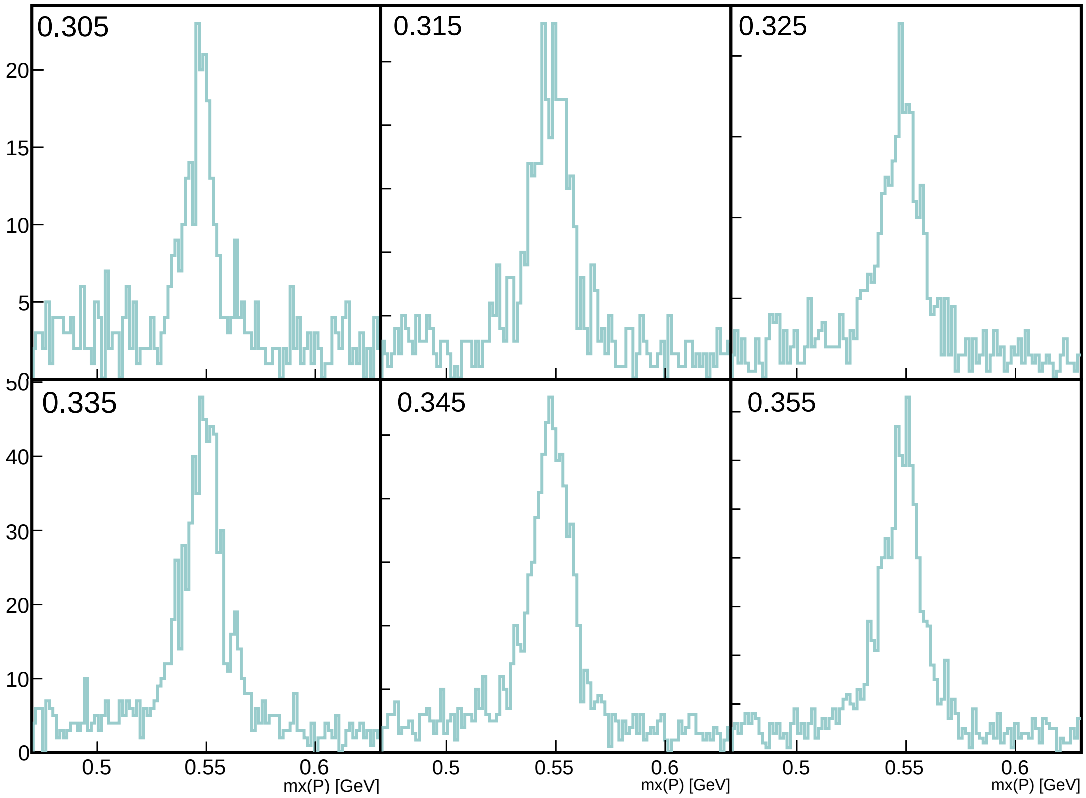

FIG. 39: $m_x(P)$ for bins $|IM(\pi^+\pi^-)| \in [0.305, 0.355]$. The centroid of the invariant mass bin is printed in the upper left corner of each plot.

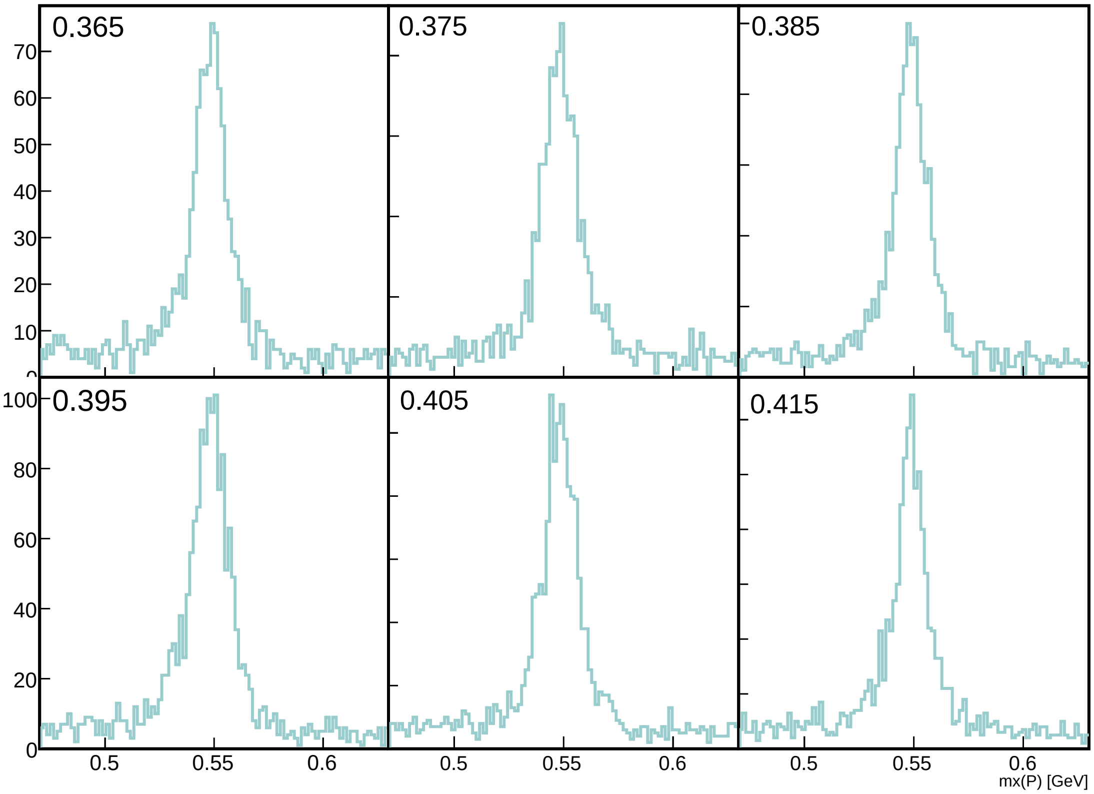

FIG. 40: $m_x(P)$ for $|IM(\pi^+\pi^-)| \in [0.365, 0.415]$. The centroid of the invariant mass bin is printed in the upper left corner of each plot.

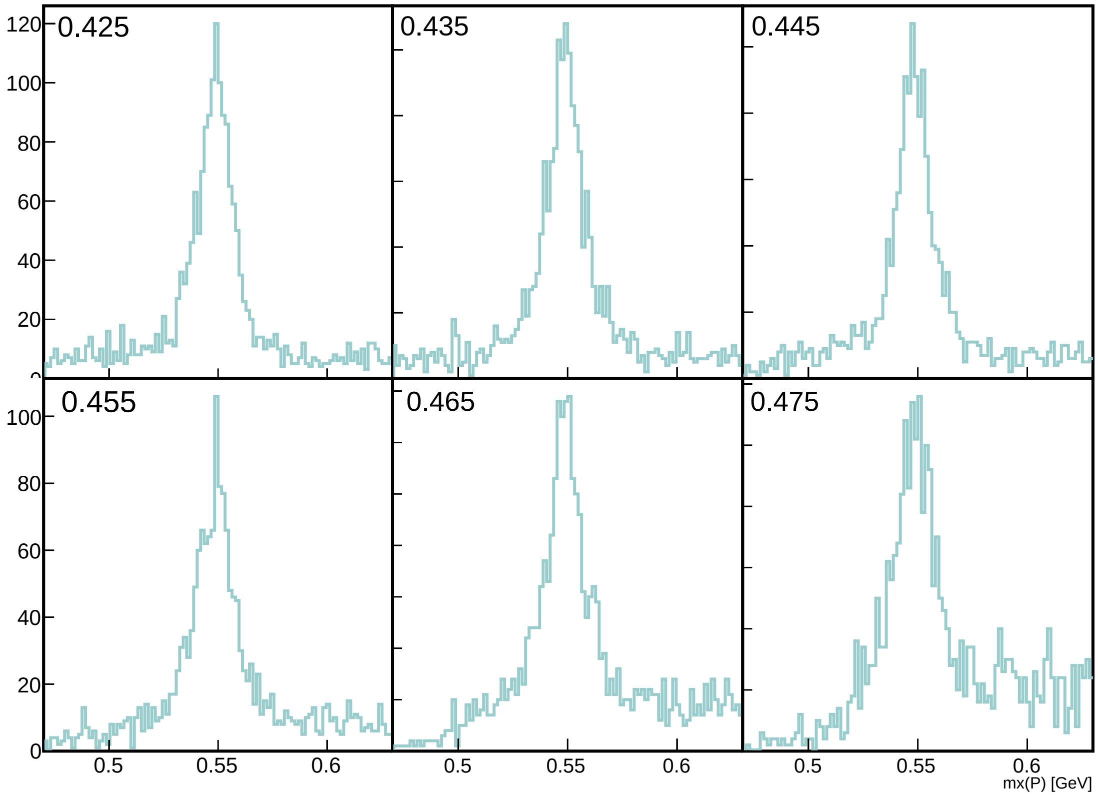

FIG. 41: $m_x(P)$ for $|IM(\pi^+\pi^-)| \in [0.425, 0.475]$. The centroid of the invariant mass bin is printed in the upper left corner of each plot.

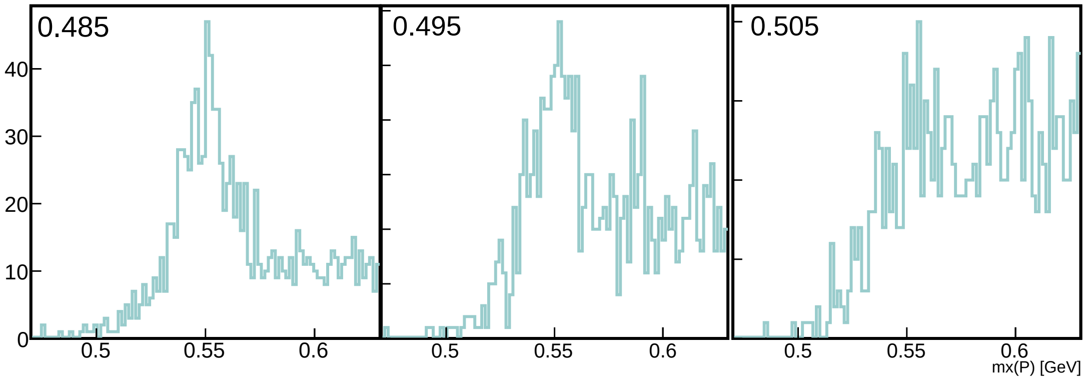

FIG. 42: $m_x(P)$ for $|IM(\pi^+\pi^-)| \in [0.485, 0.505]$. Bins above $|IM(\pi^+\pi^-) - 0.495|$ are excluded from the analysis.

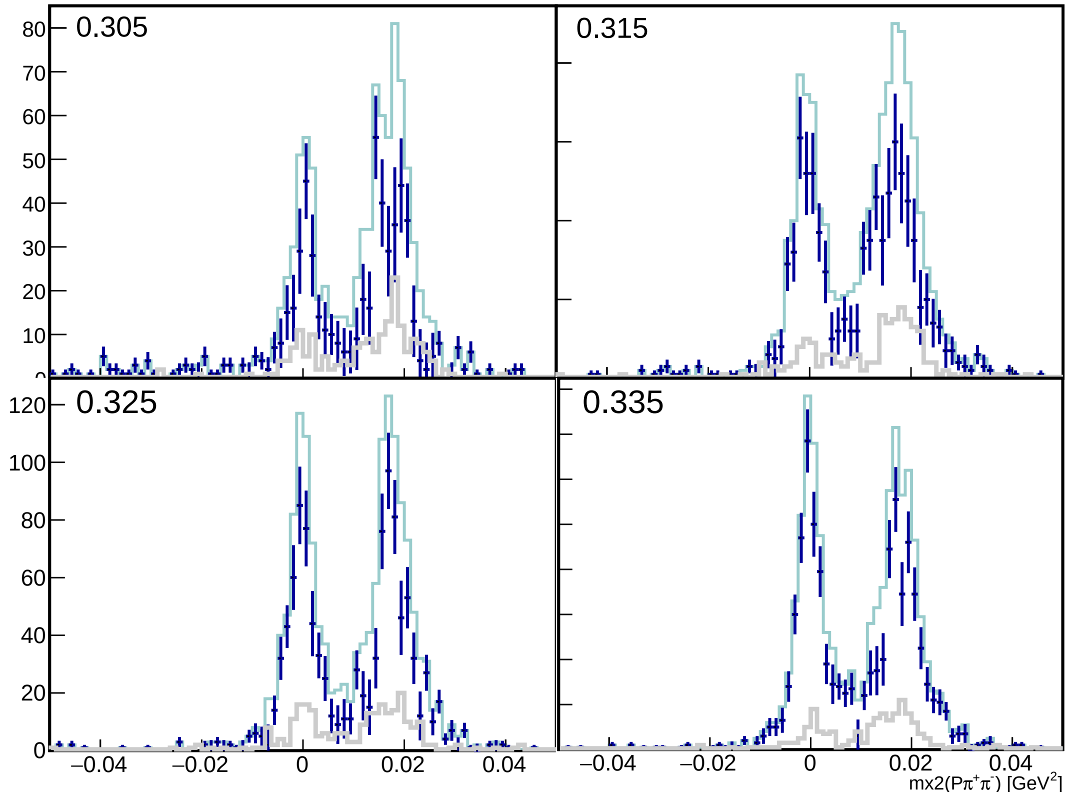

FIG. 43: $m_x^2(P\pi^+\pi^-)$, from signal region (green) and sidebands (grey). The dark blue histogram is the result of the weighted sideband events subtracted from the signal events. The selected bin of $IM(\pi^+\pi^-)$ is printed at the top of each plot.

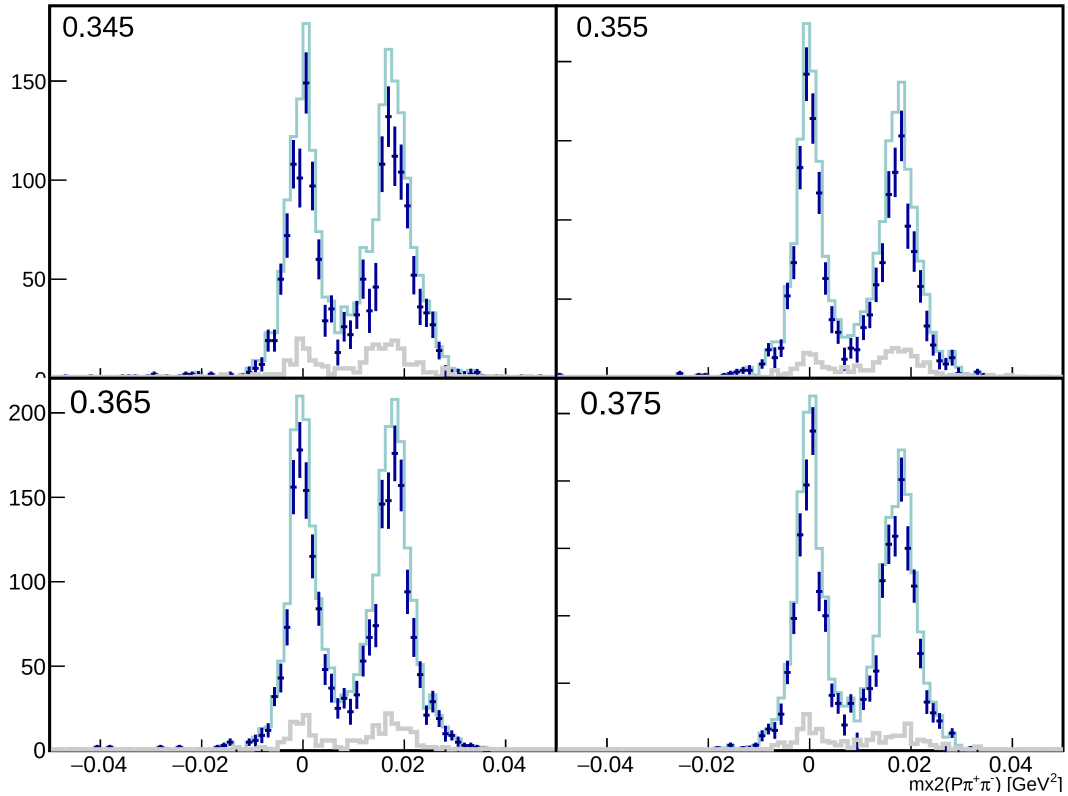

FIG. 44: $m_x^2(P\pi^+\pi^-)$, from signal region (green) and sidebands (grey). The dark blue histogram is the result of the weighted sideband events subtracted from the signal events. The selected bin of $IM(\pi^+\pi^-)$ is printed at the top of each plot.

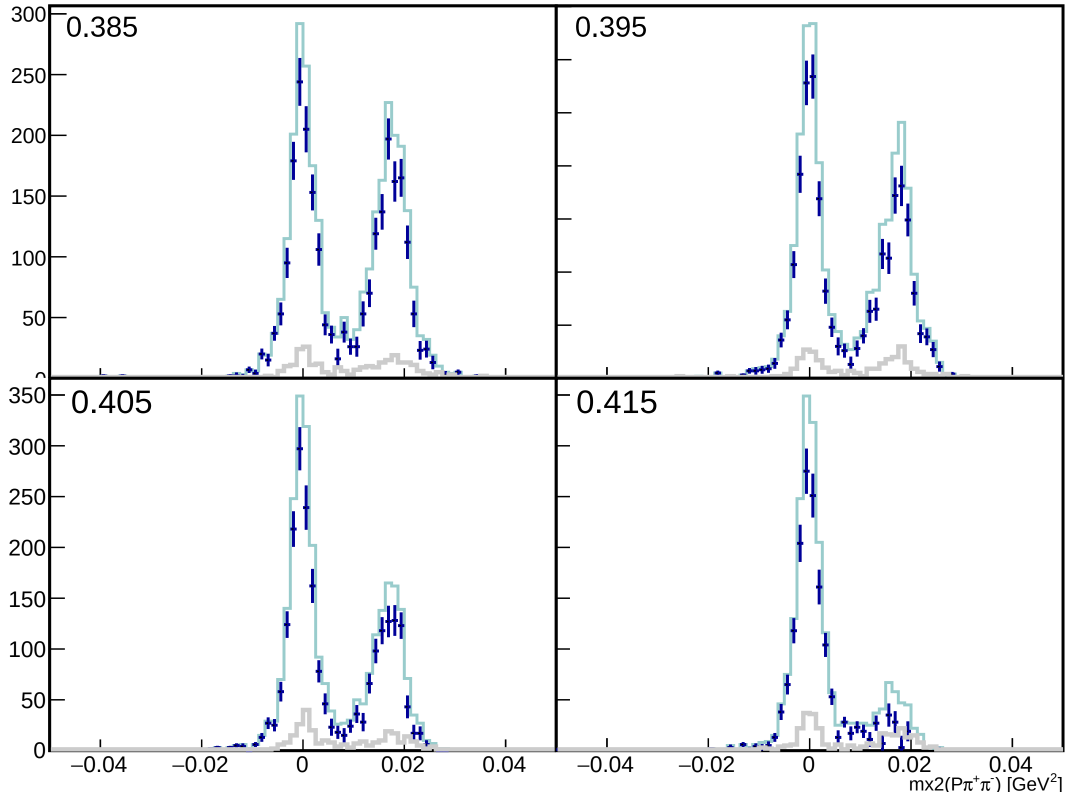

FIG. 45: $m_x^2(P\pi^+\pi^-)$, from signal region (green) and sidebands (grey). The dark blue histogram is the result of the weighted sideband events subtracted from the signal events. The selected bin of $IM(\pi^+\pi^-)$ is printed at the top of each plot.

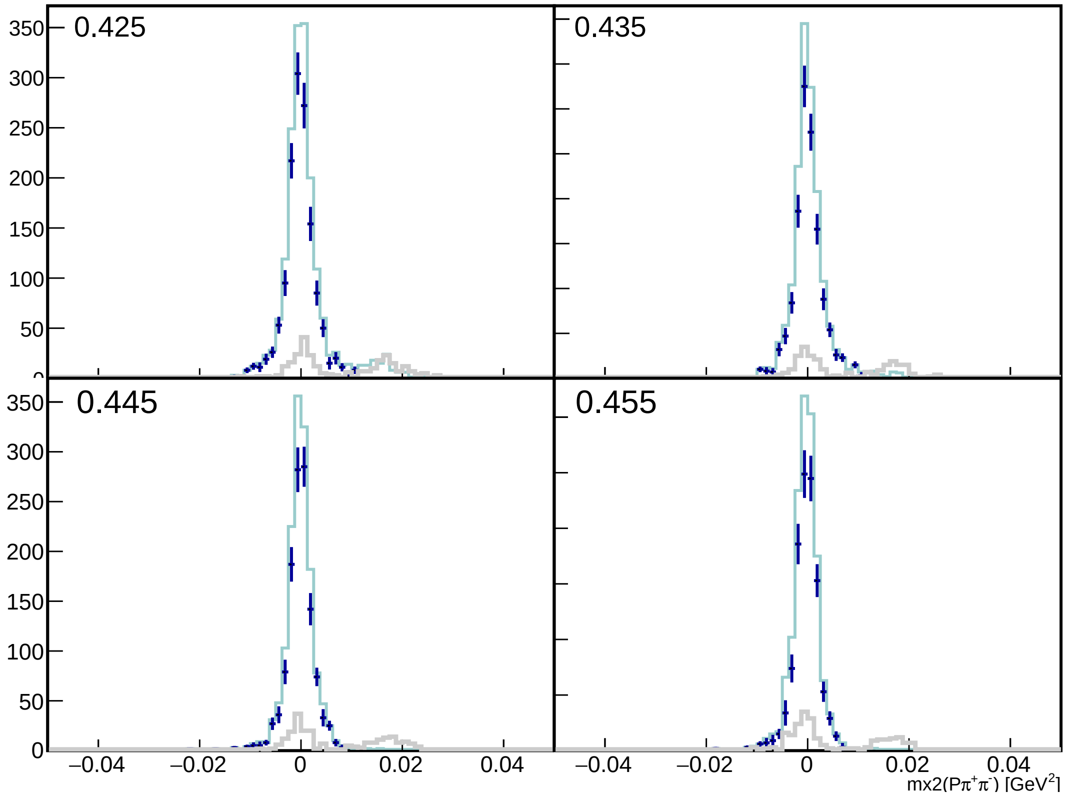

FIG. 46: $m_x^2(P\pi^+\pi^-)$, from signal region (green) and sidebands (grey). The dark blue histogram is the result of the weighted sideband events subtracted from the signal events. The selected bin of $IM(\pi^+\pi^-)$ is printed at the upper left of each plot.

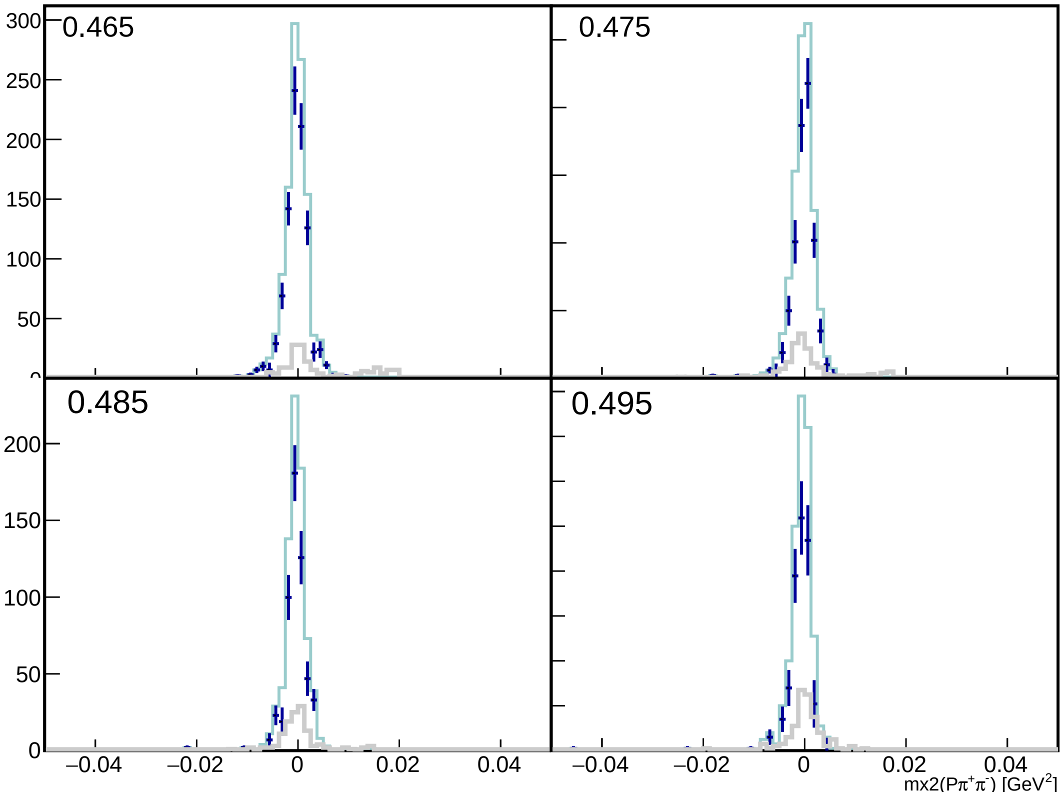

FIG. 47: $m_x^2(P\pi^+\pi^-)$, from signal region (green) and sidebands (grey). The dark blue histogram is the result of the weighted sideband events subtracted from the signal events. The selected bin of $IM(\pi^+\pi^-)$ is printed at the top of each plot.

3.5 EXTRACTING N_γ

Each Φ_{sub} histogram is fitted with either a double Gaussian and polynomial or single Gaussian and polynomial as appropriate, see Fig. 48. The number of events from the photon peak is then plotted as a function of $s(\pi^+\pi^-) = IM^2(\pi^+\pi^-)$ in Fig. 49. The total number of signal events, N_s, is 17302 ± 131.

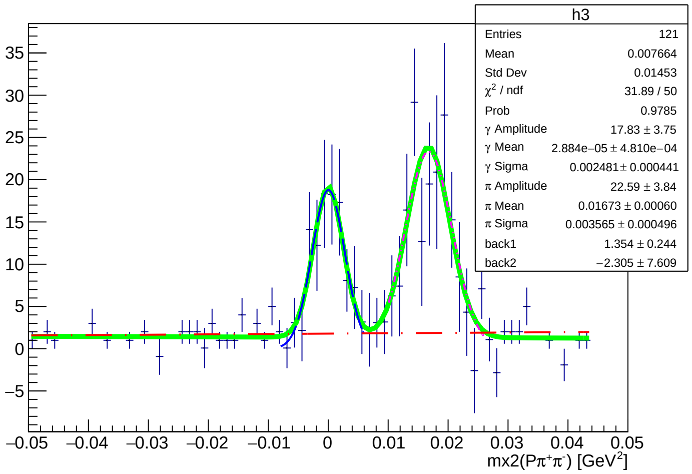

FIG. 48: Fit to $m_x^2(P\pi^+\pi^-)$ after sideband subtraction. The green solid curve is the total fit, the red dashed curve is the linear background function, and the blue and pink dashed curves correspond to the Gaussian fits for the photon and pion peaks, respectively.

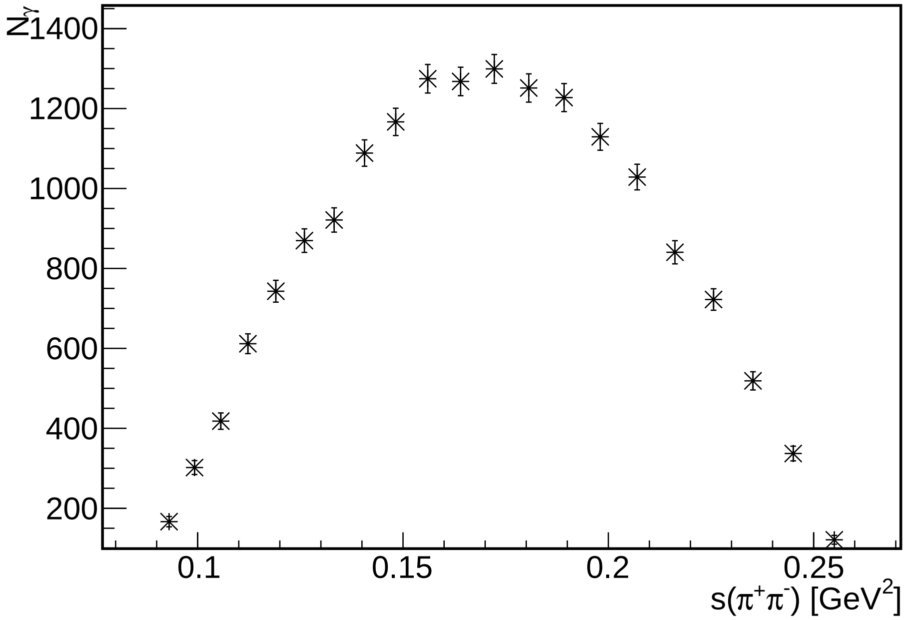

FIG. 49: Number of photons as function of s($\pi^+\pi^-$). This does not include any acceptance corrections. The total number of signal events, N_s, is 17302 ± 131.

3.6 SIMULATIONS

In the CLAS detector, there are certain regions in which physics events cannot be recorded, such as in the area dividing each sector. In addition, each sector in CLAS has inefficiencies in the subsystems: inoperable DC wires, PMT inefficiencies, dead scintillator strips, and bad paddles. Simulations are performed to understand the effects of these inefficiencies and dead regions on the experimental data. The simulation chain is described in this section. More information can be found in the Appendices.

The software used in this analysis was run inside a Docker container. A container is a standard unit of software that packages up code and all its dependencies so the application runs quickly and reliably independently of the computing environment. A Docker container image is a lightweight, standalone, executable package of software that includes everything needed to run an application: code, runtime, system tools, system libraries and settings [36]. Nick Tyler, a Graduate Student at the University of South Carolina, compiled most of the CLAS6 software inside a Docker container, thus allowing the usage of old software when analysing old data without having to recompile on the new Jefferson Lab computers.

3.6.1 SGEN

The event generator is used to generate Monte Carlo files for the reaction $\eta \rightarrow \pi^+\pi^-\gamma$. In each Monte Carlo file, 100,000 decays were generated containing the initial (γ + p) and final state particles $p, \pi^+\pi^-\gamma$. The total number of events generated is approximately 1.3 billion. The beam energy range was 1.5 to 3.5 GeV. The decay was generated according to the following:

$$|M|^2 \approx |F(s_{\pi\pi})|^2 E_\gamma^2 q^2 \sin^2\theta \tag{3.6.53}$$

where

$$E_\gamma = \frac{1}{2}\left(m_\eta - \frac{s_{\pi\pi}}{m_\eta}\right) \tag{3.6.54}$$

and where q is the pion momentum in the pion-pion rest frame. An input value of 1.80 for the α parameter was also used. The pion vector form factor parameterization was the same used in Fig. 4. The η production angle was taken according to the differential cross section published from Williams, et al. The following table tabulates the number of events generated for each IM($\pi^+\pi^-$) bin.

$IM(\pi^+\pi^-)$ (GeV)	N_{gen} (M)	$IM(\pi^+\pi^-)$ (GeV)	N_{gen} (M)
0.305	10.2	0.415	94.8
0.315	18.0	0.425	95.2
0.325	26.8	0.435	93.2
0.335	36.3	0.445	88.9
0.345	46.0	0.455	82.3
0.355	55.8	0.465	73.5
0.365	65.2	0.475	62.9
0.375	73.8	0.485	51.1
0.385	81.4	0.495	38.7
0.395	87.6	0.505	26.7
0.405	92.2	**total:**	**1.3007E9**

TABLE 9: Number of events generated for each $IM(\pi^+\pi^-)$ bin. The value of the bin displayed is the center.

SGEN produces a text file containing the particle id, momenta, and energy information for every particle in each event.

3.6.2 GAMP2MC

After event generation, the output text files from SGEN are converted to input bos files for GSIM using a program called gamp2MC. The original script was written by Michael Kunkel and was recompiled by Raffaella De Vita. The software flags used are summarized in the table below.

Name	Value	Meaning
-m		make MC banks instead of PART bank
-r	43582	run number
-o		output file
-T		put beam particle in TAGR bank
-S	0.321, -0.254, 0.378, 0.407	distribute xy vertices according to $\mu_x, \mu_y, \sigma_x, \sigma_y$
-z	-30.0,10.0	distribute z-vertex in given range

TABLE 10: gamp2MC flag parameters and definitions

3.6.3 GSIM

In order to calculate the acceptance, the CLAS GSIM package was used. GSIM is a GEANT based simulation of the CLAS detector and was the standard simulation package used when data was taken. After event generation, GSIM propagates each of the particles through the CLAS detector, resulting in a simulated set of detector signals for each track. GSIM takes into account the inefficiencies described previously in the CLAS_CALDB_RUNINDEX. This contains information about the inefficiency of each subsystem in CLAS. The run index used is calib_user.RunIndexg11a. The parameters used for GSIM are summarized in Table 11.

Name	Value	Name	Value
AUTO	1	LIST	
KINE	1	BEAM	
MAGTYPE	2	MAGSCALE	0.4974
FIELD	2	GEOM	ALL
NOSEC	OTHE	TARGET	g11a
TGPOS	0.0 0.0 0.0	STZOFF	-10.0
STTYPE	1.0	RUNG	43582
CUTS	5e-3	DCCUTS	1e-4
ECCUTS	5e-4	SCCUTS	1e-4
STCUTS	5e-5	NOGEOM	EC1 CC MINI PTG
FASTCODE		TRIG	500000

TABLE 11: GSIM flag parameters contained in ffread card and definitions

The flag KINE specifies the kinematics generator. There are default generator options or a separate kinematics generator can be used. For a separate generator, the kinematics information can be written into the MCVX and MCTK banks in the input bos files. This was the case for our simulations. The remaining flag parameters are described in the Appendix. All output bank information is stored in BOS files for further processing.

3.6.4 GPP

The output of GSIM is then processed by software called GSIM Post Processor (GPP). This program smears the particle momentum, timing information, and removes dead wires to more accurately reflect the actual resolution of the detector. The parameters used for

GPP are listed in Table 12.

Name	Value	Meaning
P	0x1f	remove dead wires
R	43582	run number for the wire map
Y		drops the DC hits according to the efficiency in the GPP map and the DC wire map in the database
f	1.0	time smearing
a	1.0	DOCA smearing region 1
b	1.0	DOCA smearing region 2
c	1.0	DOCA smearing region 3

TABLE 12: GPP flag parameters and definitions

The DOCA smearing values of 1.0 indicate default values where minimal smearing is used. After GPP, the events are passed through RECSIS.

3.6.5 RECSIS

After post-processing, the simulated data is processed through the user_ ana routine, which is an implementation of RECSIS. RECSIS, REConstruction and analySIS, is the same framework that was used to cook the g11a data. The reconstructed Monte Carlo events are then analyzed using the same cuts as the experimental data.

3.7 SIMULATION VALIDATION

In order to check the accuracy of our event generator, we compare momenta, θ, and ϕ of each final state particle, in addition to the photon beam energy. The comparisons are shown in Figures 50-, 53. The experimental data is shown in blue and the simulated data is in red. Each histogram is normalized to unity using its integral. For θ_γ, angles less than 15 deg and greater than 45 deg were removed from the analysis. For most quantities, the agreement between the Monte Carlo data and experimental data is good.

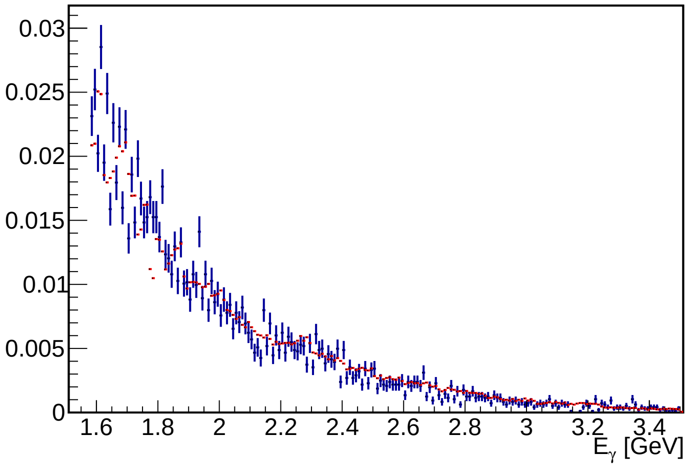

FIG. 50: Comparison of photon beam energy. Experimental data is in blue and simulated data is in red.

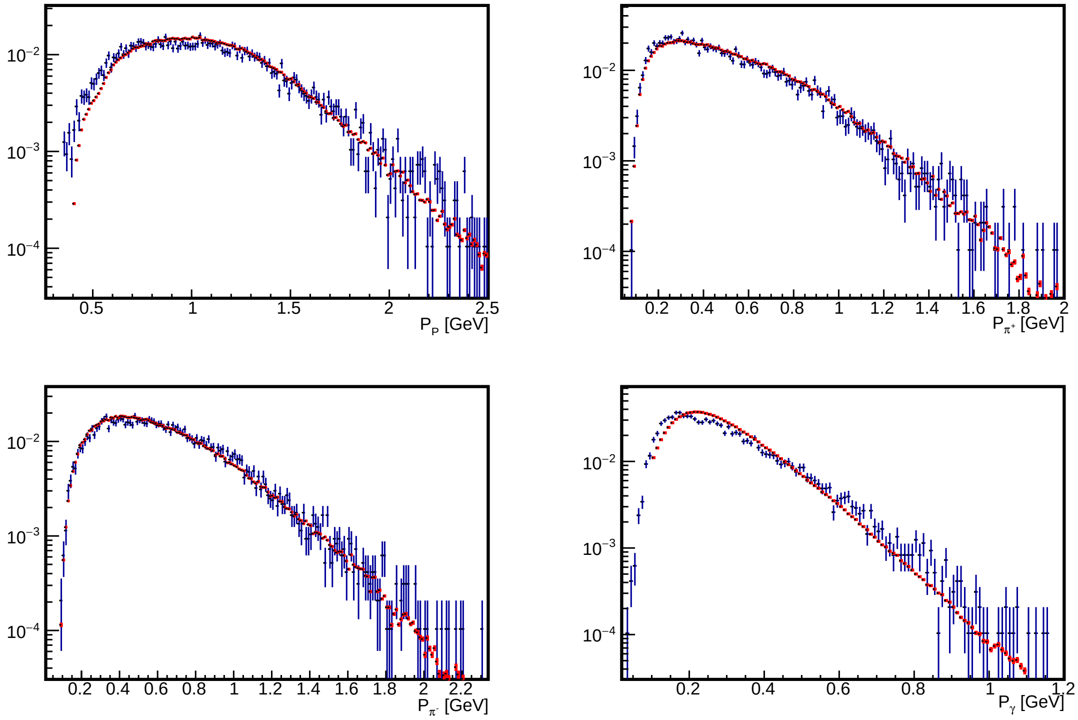

FIG. 51: Comparison of momenta of each final state particle from Monte Carlo and experimental data. Experimental data is in blue and simulated data is in red.

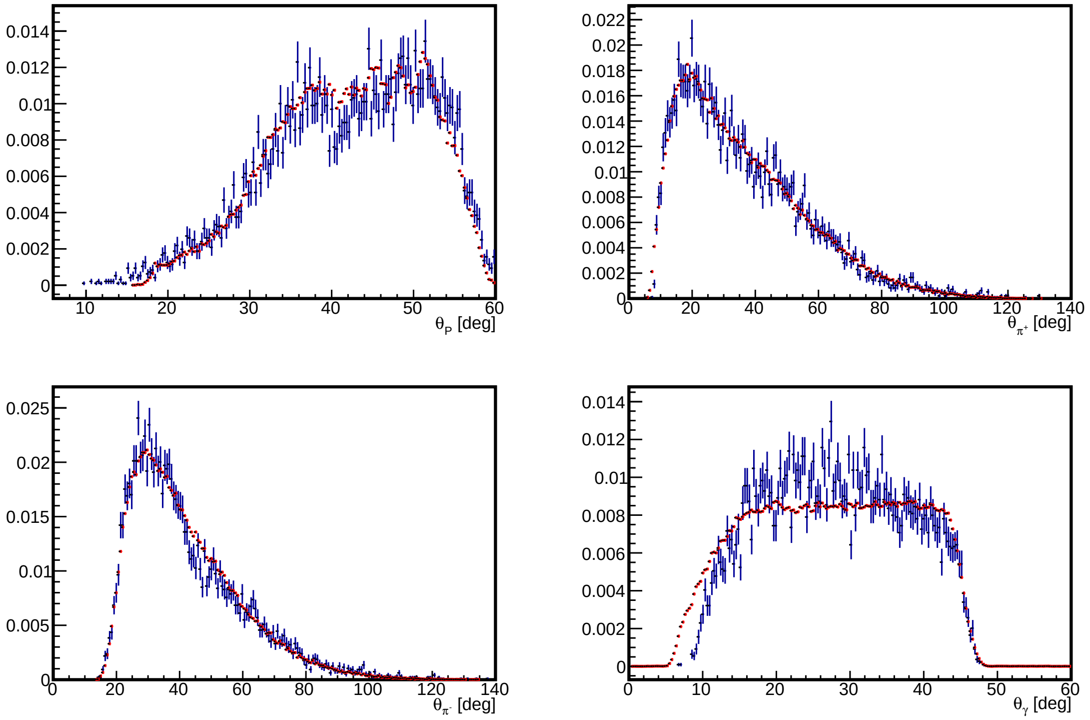

FIG. 52: Comparison of θ of each final state particle from Monte Carlo and experimental data. Experimental data is in blue and simulated data is in red. An additional cut has been placed on θ_γ to be in the range of 15-45 deg.

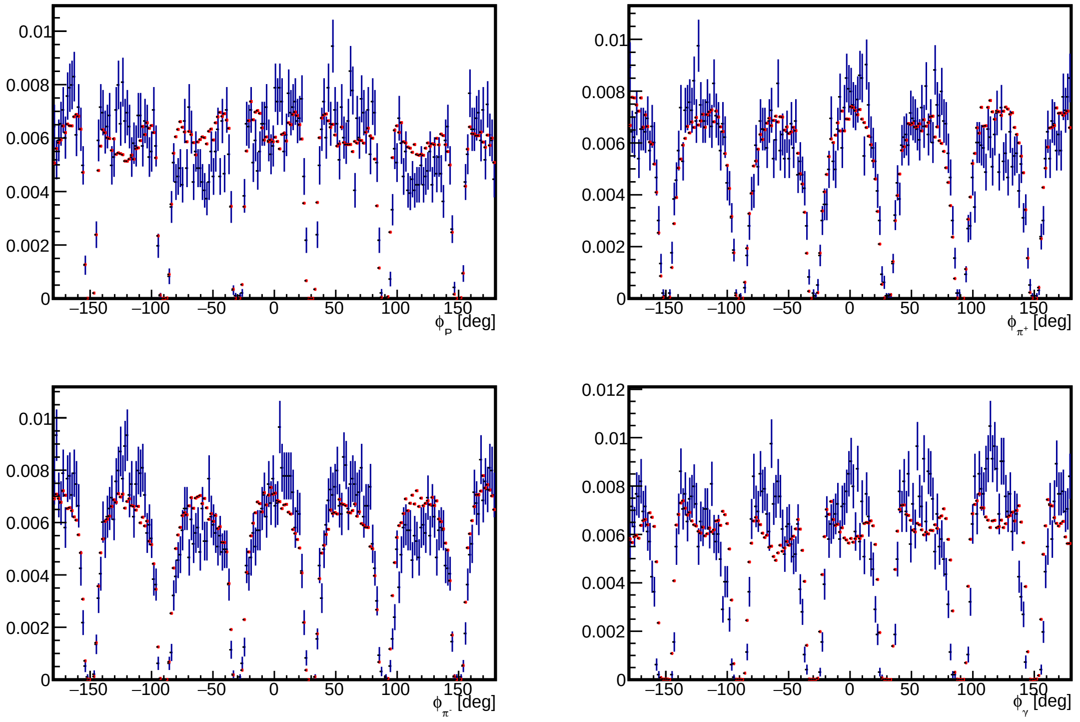

FIG. 53: Comparison of ϕ of each final state particle. Experimental data is in blue and simulated data is in red.

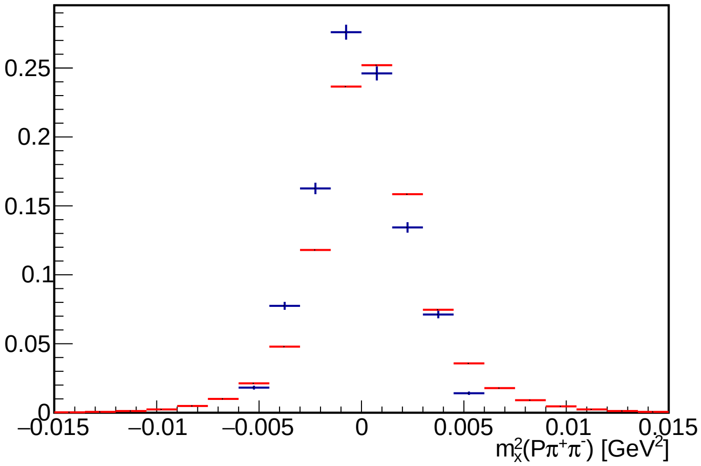

FIG. 54: Comparison of $m_x^2(P\pi^+\pi^-)$. Experimental data is in blue and simulated data is in red.

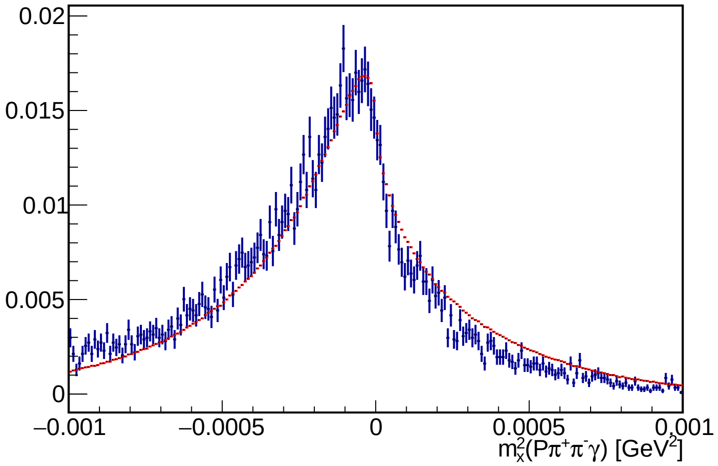

FIG. 55: Comparison of $m_x^2(P\pi^+\pi^-\gamma)$. Experimental data is in blue and simulated data is in red.

The comparison between the data and reconstructed Monte Carlo events is also shown for $m_x^2(P\pi^+\pi^-)$ and $m_x^2(P\pi^+\pi^-\gamma)$ in Fig. 54 and Fig. 55. The overall agreement between the g11 data and the reconstructed Monte Carlo is good.

CHAPTER 4

RESULTS

4.1 CLAS DETECTOR ACCEPTANCE

The acceptance is the probability that an event will be kept after it has been passed through the simulation chain (described in Chapter 3) and subject to the same cuts as in the data analysis. Events that do pass are called reconstructed events. The acceptance for each s($\pi^+\pi^-$) bin is calculated as:

$$A(s_{\pi^+\pi^-}) = \frac{N_{rec}}{N_{gen}} \tag{4.1.55}$$

where N_{rec} is the number of successfully reconstructed events and N_{gen} is the number of generated events in each bin. The error on each data point is calculated using the standard error propagation for Poisson statistics,

$$\begin{aligned} \sigma(N_{rec}) &= \sqrt{N_{rec}} \\ \sigma(N_{gen}) &= \sqrt{N_{gen}} \end{aligned} \tag{4.1.56}$$

From Eq. 4.1.55, the error for each data point is derived as

$$\left(\frac{\sigma_A}{A}\right) = \left[\left(\frac{\sigma(N_{rec})}{N_{rec}}\right)^2 + \left(\frac{\sigma(N_{gen})}{N_{gen}}\right)^2\right]^{\frac{1}{2}}. \tag{4.1.57}$$

The acceptance as a function of s($\pi^+\pi^-$) is shown in Fig. 56. The acceptance is fit with a fourth-order polynomial. The data is then corrected by the value of the polynomial fit at each $s(\pi^+\pi^-)$ bin.

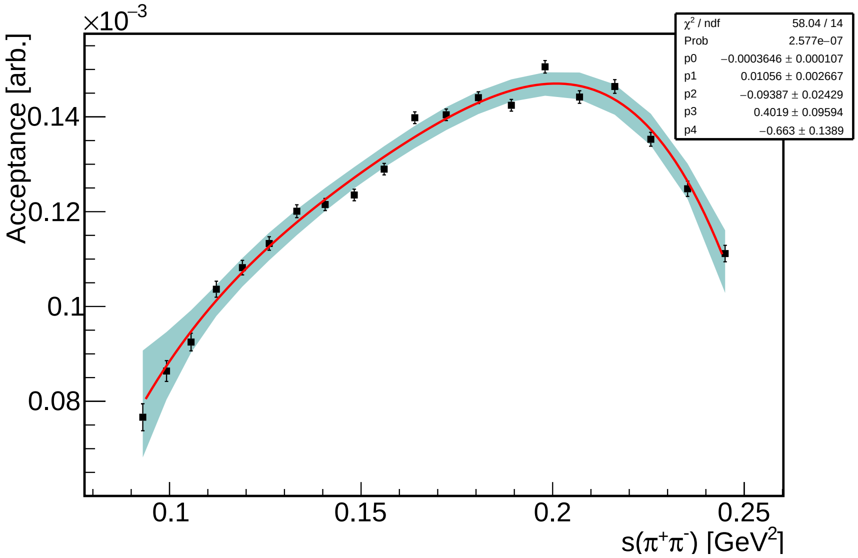

FIG. 56: Acceptance as function of s($\pi^+\pi^-$). Red line is a fit with 4th order polynomial. Green band represents 95% confidence interval.

4.2 α PARAMETER

After obtaining the acceptance, the data in Fig. 49 is then corrected by the value of the fitted function at the corresponding bin. To account for the errors on the parameters, the covariance matrix was recorded and errors were calculated using the general formula presented in Eq. 15.

$$\sigma^2_{polynomial} = \begin{pmatrix} \frac{\partial f}{\partial p_0} & . & . & . & \frac{\partial f}{\partial p_n} \end{pmatrix} \begin{pmatrix} \sigma^2_{a_0} & . & . & \rho\sigma_{a_0}\sigma_{a_n} \\ . & . & . & . \\ . & . & . & . \\ . & . & . & . \\ \rho\sigma_{a_n}\sigma_{a_0} & . & . & \sigma^2_{a_n} \end{pmatrix} \begin{pmatrix} \frac{\partial f}{\partial p_0} \\ . \\ . \\ . \\ \frac{\partial f}{\partial p_n} \end{pmatrix} \tag{4.2.58}$$

.

The resulting data is then fit with Eq. 2 in order to extract α. Fig. 57 displays the fit to the acceptance corrected data. The error bars contain the statistical error of the number of reconstructed photons and the error from the acceptance added in quadrature. Our result is $\alpha = 1.51 \pm 0.24_{stat}$.

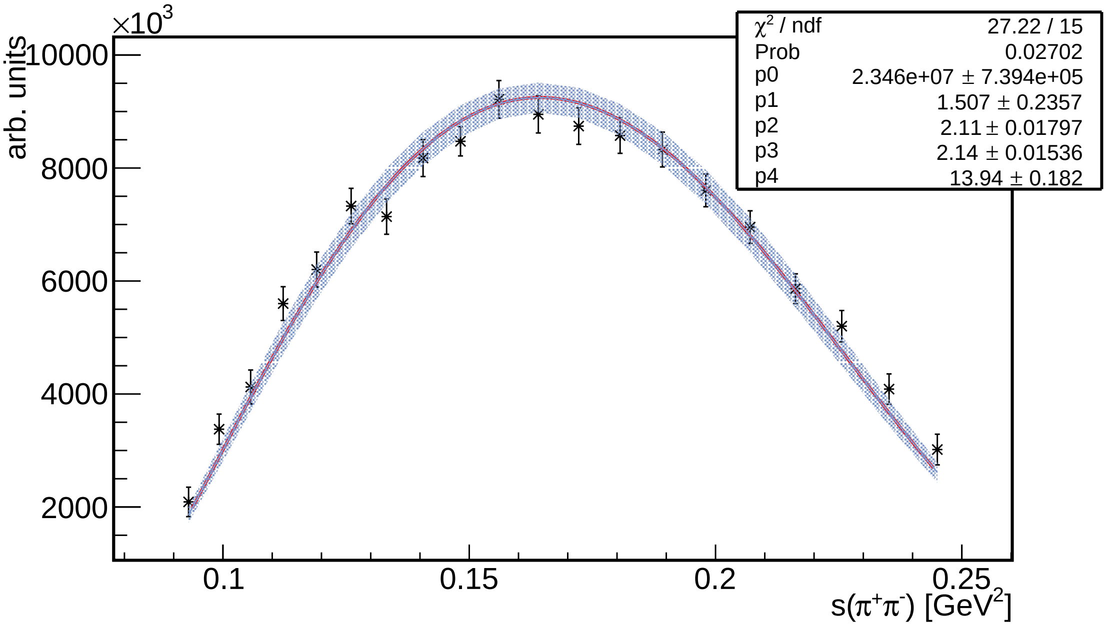

FIG. 57: Acceptance corrected N_γ in arbitrary units as function of s($\pi^+\pi^-$). Error bars contain statistical errors and the error from the acceptance added in quadrature. The red line is the fit function presented in Eq. 2. The purple band is 95% confidence interval.

4.3 SYSTEMATIC ERRORS

In order to calculate the systematic error of our measurement, the following cuts were varied from their original values:

- $|m_x(P) - M_\eta| < 0.03$
- $|m_x(P) - 0.605| < 0.0075$
- $|m_x(P) - 0.490| < 0.0075$
- $|m_x^2(P\pi^+\pi^-\gamma)| < 0.0005$

The width of the signal and sideband regions defined when performing the background subtraction can contribute a systematic error to the measurement. We also vary the exclusivity cut. The changes in the acceptance due to the new cuts is assumed to be negligible. To account for the systematic errors, the cuts are adjusted and then the analysis procedure described in Chapter 3 is repeated for each cut individually. The fit results for the systematic variations can be seen in Fig. 59 -60.

Original Cut	Cut Variation	Description
$\lvert mx\_P - M_\eta\rvert < 0.3$	$\lvert mx\_P - M_\eta\rvert < 0.34$	adjusting signal region
$\lvert mx\_P - 0.605\rvert < 0.0075$	$\lvert mx\_P - 0.605)\rvert < 0.0085$	adjusting right sideband
$\lvert mx\_P - 0.490\rvert < 0.0075$	$\lvert mx\_P - 0.490)\rvert < 0.0085$	adjusting left sideband
$\lvert mx2\_P\pi^+\pi^-\gamma\rvert < 0.0005$	$\lvert mx2\_P\pi^+\pi^-\gamma\rvert < 0.00055$	less exclusive cut
$\lvert \mathrm{mx2\_P}\pi^+\pi^-\gamma\rvert < 0.0005$	$\lvert \mathrm{mx2\_P}\pi^+\pi^-\gamma\rvert < 0.00045$	more exclusive cut

TABLE 13: Cuts used in calculating systematic errors.

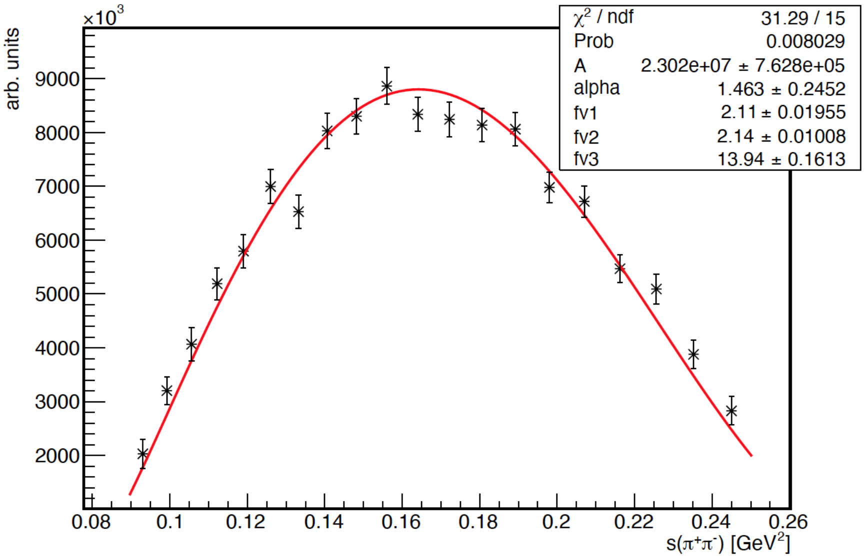

FIG. 58: Fit results for $m_x^2(P\pi^+\pi^-\gamma) < 0.00045$.

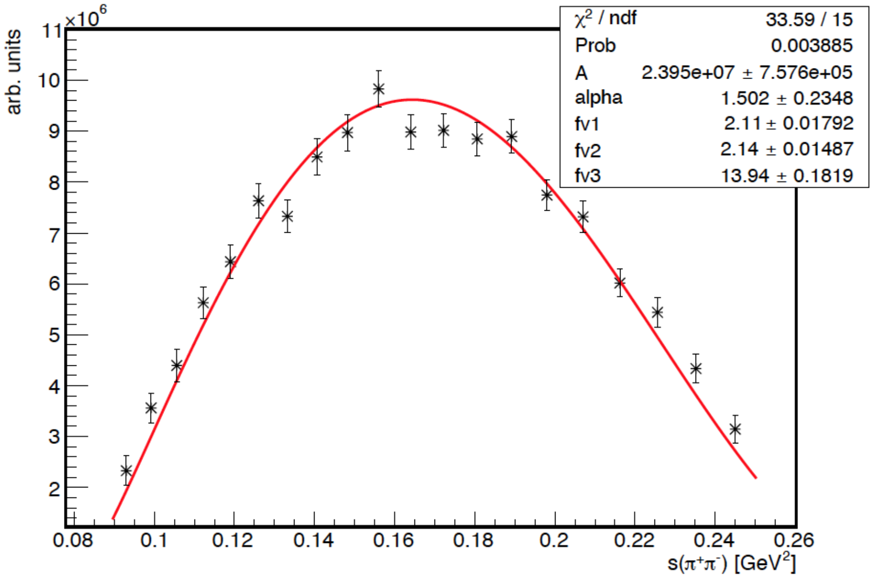

FIG. 59: Fit results for $m_x^2(P\pi^+\pi^-\gamma) < 0.00055$.

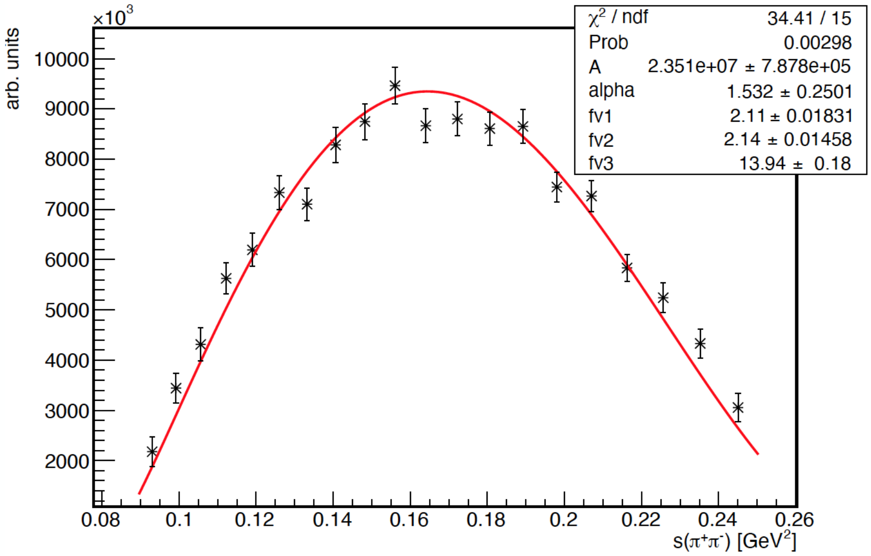

FIG. 60: Fit results for adjusting signal region to $|m_x(P) - M_\eta|$ and sideband regions to $|m_x(P) - 0.605)| < 0.0085$ and $|m_x(P) - 0.490)| < 0.0085$.

The relative difference between the reference value, α_r, and the systematic variation, α_{sys}, is calculated as

$$\Delta\alpha_i = \frac{|\alpha_r - \alpha_{sys}|}{\alpha_r}. \tag{4.3.59}$$

The relative difference is calculated for each systematic error and the results are added in quadrature. The results are tabulated in Table 14. The largest contribution to the total systematic error is due to the exclusivity cut.

Systematic	Relative Error
$\lvert m_x(P) - M_\eta\rvert < 0.034$ $\lvert m_x(P) - 0.605\rvert < 0.0085$ $\lvert m_x(P) - 0.490\rvert < 0.0085$	0.006
$\lvert m_x^2(P\pi^+\pi^-\gamma)\rvert < 0.00055$	0.016
$\lvert m_x^2(P\pi^+\pi^-\gamma)\rvert < 0.00045$	0.039
Total Systematic Error	0.043

TABLE 14: Tabulated systematic errors and their total.

4.4 COMPARISON TO OTHER MEASUREMENTS

The most recent measurements of the α parameter, produced by WASA-at-COSY and KLOE collaborations, are summarized in the table below and plotted together with various theoretical calculations in Fig. 61. The average of the experimental measurements (KLOE, CLAS, WASA) is 1.57 ± 0.34 and is represented by the purple band. Only the recent theoretical work from Kubis and Plenter [40] is in agreement with the latest experimental measurements.

4.4.1 COMPARISON WITH PREVIOUS EXPERIMENTAL MEASUREMENTS

The first reported measurement of the α parameter was obtained from Gormley, et al. in 1970. The analysis of 7250 $\eta \rightarrow \pi^+\pi^-\gamma$ events yielded an $\alpha = 1.8 \pm 0.4$. In 1973, Layter, et al. analysed 18150 $\eta \rightarrow \pi^+\pi^-\gamma$ events yielding an $\alpha = -0.9 \pm 0.1$. The most recent measurements were performed by the WASA-at-COSY collaboration, analysing 13960 ± 140 events, yielding an $\alpha = 1.89 \pm 0.25_{stat} \pm 0.59_{sys} \pm 0.02_{theo}$. The KLOE collaboration measured an $\alpha = 1.32 \pm 0.2_{total}$. It is important to note this measurement takes in to account the effects of the a2 tensor meson. Our measurement is in agreement with the result from the KLOE collaboration and is more precise than that of the WASA collaboration. Our measurement differs significantly from that of Layter, et al.

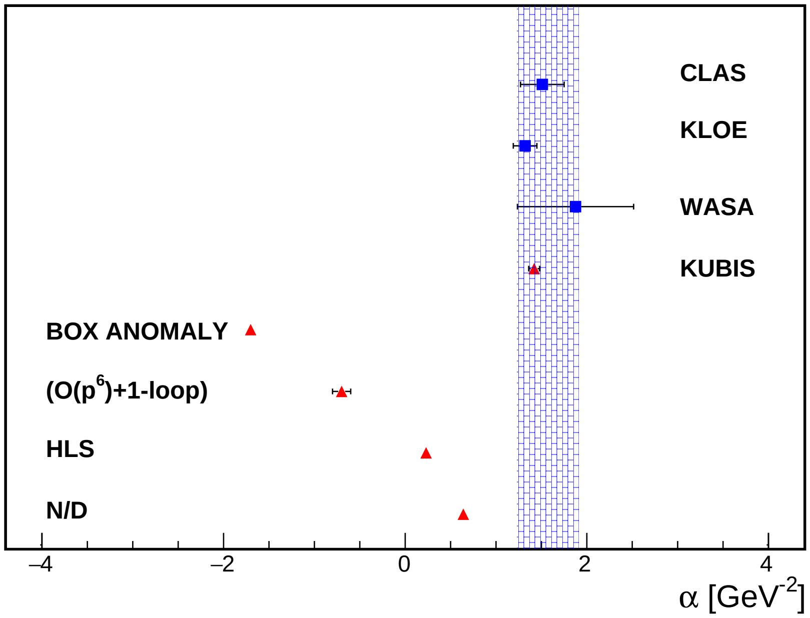

FIG. 61: Graphical representation of experimental measurements (squares) and theoretical calculations (triangles) of α from the decay $\eta \to \pi^+\pi^-\gamma$. The purple shaded region represents the average of the three experimental measurements. Error bars for the experimental measurements contain statistical and systematic errors added in quadrature. References for data points (top to bottom) KLOE [38], WASA [39], Kubis [40], Box Anomaly [24], (O(p^6)+1-loop) [19], HLS [21], and N/D [23].

4.4.2 COMPARISON WITH THEORY PREDICTIONS

From Fig. 61 it is easily seen that the experimental measurements (within the average band) agree with the most recent theoretical result from Kubis [40]. The remaining theoretical predictions, corresponding to the different models described in Sec. 1.5, are in stark contrast with our measurement.

4.5 CONCLUSION

We extract the α parameter from a model independent fit to the dipion invariant mass distribution using CLAS g11 data. This parameter measures the contribution of the dipion momentum dependence to the partial decay width of $\eta \to \pi^+\pi^-\gamma$, which proceeds from the box anomaly. Our value, $\alpha = 1.51 \pm 0.24_{\text{stat}} + 0.04_{\text{sys}}$ is in agreement with the most recent experimental measurement from the KLOE collaboration and the theoretical calculation from Kubis et al. Our result strongly excludes the previous theoretical calculations.

BIBLIOGRAPHY

[1] https://www.physik.uzh.ch/groups/serra/StandardModel.html

[2] P.A. Zyla et al. (Particle Data Group), Prog. Theor. Exp. Phys. 2020, 083C01 (2020)

[3] Thimo Petri, Anomalous Decays of Pseudoscalar Mesons, PhD thesis Institut fur Kern- physik, Forschungszentrum Julich 2010

[4] J. Wess, B. Zumino. Consequences of anomalous Ward identities. *Phys.Lett.,* B37:95, (1971).

[5] E. Witten. Global Aspects of Current Algebra. *Nucl.Phys.,* B223:422-432, 1983.

[6] C. Q. Geng, J. N. Ng, and T. H. Wu, Mod. Phys. Lett. A17, 1489 (2002), hep-ph/0201191

[7] F. Stollenwerk, C. Hanhart, A. Kupsc, U. G. Meissner and A. Wirzba, Model-independent approach to $\eta \to \pi^+\pi^-\gamma$ and $\eta' \to \pi^+\pi^-\gamma$, *Phys. Lett.,* B707:184-190 2012.

[8] J. Gasser, U.-G. Meißner, Nucl. Phys. B 357 (1991) 90.

[9] J. Bijnens, G. Colangelo, P. Talavera, JHEP 9805 (1998) 014.

[10] B. Ananthanarayan, I. Caprini, and I.S. Imsong, Phys. Rev. D 83 (2011) 096002; B. Ananthanarayan and S. Ramanan, Eur. Phys. J. C 60 (2009) 73; J.F. De Troconiz and F.J. Yndurain, Phys. Rev. D 65 (2002) 093001; J.A. Oller, E. Oset, J.E. Palomar, Phys. Rev. D 63 (2001) 114009; I. Caprini, Eur. Phys. J. C 13 (2000) 471.

[11] R. Garcia-Martin, R. Kaminski, J.R. Pelaez, J. Ruiz de Elvira, F.J. Yndurain, Phys. Rev. D 83 (2011) 074004.

[12] J.F. De Troconiz, F.J. Yndurain, Phys. Rev. D 65 (2002) 093001.

[13] F. Guerrero, Phys. Rev. D 57 (1998) 4136; F. Guerrero, A. Pich, Phys. Lett. B 412 (1997) 382.

[14] F.-K. Guo, C. Hanhart, F.J. Llanes-Estrada, U.-G. Meißner, Phys. Lett. B 678 (2009) 90.

[15] R.R. Akhmetshin, et al., JETP Lett. 84 (2006) 413 [Pisma Zh. Eksp. Teor. Fiz. 84 (2006) 491]; R.R. Akhmetshin, et al., CMD-2 Collaboration, Phys. Lett. B 648 (2007) 28; A. Aloisio, et al., KLOE Collaboration, Phys. Lett. B 606 (2005) 12.

[16] B. Aubert, et al., BABAR Collaboration, Phys. Rev. Lett. 103 (2009) 231801.

[17] F. Ambrosio, et al., KLOE Collaboration, Phys. Lett. B 700 (2011) 102.

[18] S.R. Amendolia, et al., NA7 Collaboration, Nucl. Phys. B 277 (1986) 168.

[19] J. Bijnens, A. Bramon, F. Cornet. Three Pseudoscalar Photon Interactions in Chiral Perturbation Theory. *Phys. Lett.,* B237:488, 1990.

[20] C. Picciotto. Analysis of eta, K(L) $\rightarrow \pi^+\pi^-\gamma$ using chiral models. *Phys. Rev.,* D45:1569-1574, 1992.

[21] M. Benayoun, P. David, L. DelBuono, P. Leruste, H.B. O'Connell. Anomalous η/η' decays: The Triangle and Box Anomalies. *Eur. Phys. J. C* 31:525-547, 2003.

[22] M. Benayoun, P. David, L. DelBuono, O. Leitner, Eur. Phys. J. C 65 (2010) 211.

[23] E.P. Venugopal, B.R. Holstein, Phys. Rev. D 57 (1998) 4397.

[24] B.R. Holstein. Allowed eta decay modes and chiral symmetry. *Phys. Scripta* T99:55-67, 2002.

[25] D.I. Sober, et al. The bremsstrahlung tagged photon beam in Hall B at JLab. Nucl Inst Meth A 440, 263 (2000)

[26] G. Adams et al.. The CLAS Cherenkov detector. Nucl. Instr. and Meth. A, Vol 465, p 81-111, 2000

[27] E. Pasyuk. The CLAS ELOSS Package. Software available via the CLAS CVS repository under clas/packages/utilities/eloss.

[28] E. Smith et al. The time-of-flight system for CLAS. *Nucl Inst Meth.,* A432:265 1999.

[29] Y.G. Sharabian et al. A new highly segmented start counter for the CLAS detector. *Nucl. Phys.,* A556:246 2006.

[30] M.D. Mestayer et al. The CLAS drift chamber system. *Nucl Inst Meth.,* A449:81 2000.

[31] D.S. Carman et al. The Region One drift chamber for the CLAS spectrometer. *Nucl Inst Meth.,* A419:315 1998.

[32] M. Amarian, et al. “The clas forward electromagnetic calorimeter,” Nuclear Instruments and Methods in Physics Research Section A: Accelerators, Spectrometers, Detectors and Associated Equipment, vol. 460, no. 2, pp. 239 – 265, 2001.

[33] B. Mecking, et al. *The CEBAF Large Acceptance Spectrometer (CLAS)*, Nucl Inst Meth A 503, 513 (2003).

[34] M. Ungaro, R. De Vita, and L. Elouadrhiri. g11 Data Processing. CLAS-Note, 2005-004.

[35] V. Kubarovsky, http://www.jlab.org/Hall-B/secure/g11/valery/note/ valery note.ps.gz

[36] https://www.docker.com/resources/what-container

[37] Mike Williams, Measurement of Differential Cross Sections and Spin Density Matrix Elements along with a Partial Wave Analysis for $\gamma p \to p\omega$ using CLAS at Jefferson Lab, PhD thesis Carnegie Mellon University 2007

[38] D. Babusci, et al. Measurement of $\Gamma(\eta \to \pi^+\pi^-\gamma)/\Gamma(\eta \to \pi^+\pi^-\pi^0)$ with the KLOE Detector. *Phys. Lett.,* B718:910-914, 2013.

[39] P. Adlarson, et al. Exclusive Measurement of the $\eta \to \pi^+\pi^-\gamma$ Decay. *Phys. Rev. Lett.,* B707:243-249, 2013.

[40] Kubis, B., Plenter, J. Anomalous decay and scattering processes of the η meson Eur. Phys. J. C 75, 283 (2015)

[41] Seraydaryan, Heghine. ”Photoproduction of the $\phi(1020)$ Meson in Neutral Decay Mode $\gamma p \to \phi pto K_s K_L P$” (2011). Doctor of Philosophy (PhD), dissertation, Physics, Old Dominion University, DOI: 10.25777/8drz-bq08 https://digitalcommons.odu.edu/physics$_e tds/$90

APPENDIX A

SIMULATION SCRIPTS

A.1 GAMP2MC

The executable to run the gamp2MC script is located here:

```
/work/clas/clasg11/devita/gamp2MC/build/bin/gamp2MC
```

. The command used is

```
/work/clas/clasg11/devita/gamp2MC/build/bin/gamp2MC -m -r43582
-o<output file>-T -S-0.321,-0.254,0.378,0.407
-z-30,10 <input file>
```

A.2 GSIM

The command used to run gsim:

```
gsim_bat -ffread gsiman.input -kine 1 -mcin
<input bos file> -bosout
```

FFREAD card used for simulations:

```
CUTS   5.e-3 5.e-3 5.e-3 5.e-3 5.e-3
DCCUTS 1.e-4 1.e-4 1.e-4 1.e-4 1.e-4
ECCUTS 5.e-4 5.e-4 5.e-4 5.e-4 5.e-4
SCCUTS 1.e-4 1.e-4 1.e-4 1.e-4 1.e-4
STCUTS 5.e-5 5.e-5 5.e-5 5.e-5 5.e-5
AUTO 1
KINE 1
MAGTYPE 2
MAGSCALE 0.4974
FIELD 2
GEOM ’ALL’
NOGEOM ’EC1’ ’CC’  ’MINI’  ’PTG’
```

```
NOSEC  'OTHE'
TARGET 'g11a'
TGPOS 0.0 0.0 0.0
STZOFF  -10.0
STTYPE 1
RUNG   43582
TRIG 500000
STOP
```

A.3 GPP

Command line to run GPP:

```
gpp -P0x1f -oclas.centos6.gpp -R43582
-a1.0 -b1.0 -c1.0 -f1.0 -Y clas.centos6.evt
```

A.4 RECSIS

Command line for cooking:

```
user_ana -t new_recsis.tcl
```

RECSIS file used for cooking g11 data

```
source /group/clas/builds/test3/
src/clas6-trunk/reconstruction/recsis/recsis_proc.tcl;
turnoff ALL;
global_section off;
turnon seb trk tof egn user pid;
inputfile           clas.evt;
setc chist_filename ntuple.hbook;
setc log_file_name  logfile;
setc outbanknames(1) "all";
outputfile clas.out PROC 2047;
setc prlink_file_name  "prlink_g11_1920.bos";
setc bfield_file_name  "bgrid_T67to33.fpk";
set torus_current      1920;
set mini_torus_current 0;
```

```
set poltarget_current  0;
set TargetPos(3)       -10.;
set trk_maxiter 8;
set trk_minhits(1) 2;
set trk_lrambfit_chi2 50.;
set trk_tbtfit_chi2 70.;
set trk_prfit_chi2 70.;
set trk_statistics 3 ;
set dc_xvst_choice 0;
set def_adc -1;
set def_tdc -1;
set def_atten -1;
set def_geom -1;
set st_tagger_match 15.;
set lst_do          -1;
set lpid_make_trks   0;
set photon_trig_type  4;
set lseb_nt_do      -1;
set lall_nt_do      -1;
set lscr_nt_do      -1;
set lpart_nt_do     -1;
set lst_nt_do       -1;
set ltbt_nt_do      -1;
set lmvrt_nt_do     -1;
set lmctk_nt_do     -1;
set lgpid_do     -1;
fpack "timestop␣-9999999999"
setc rec_prompt "CLASCHEF_recsis>␣";
go 2000000;
exit_pend;
```

APPENDIX B

DOCKER CONTAINER

To run software interactively inside the Docker container:

```
module load singularity
```

then attach the following command ahead of the program you want to run:

```
singularity exec /work/clas/clase1/tylern/clas6.img
```

for example, to run GSIM:

```
singularity exec /work/clas/clase1/tylern/clas6.img gsim_bat -ffread <ffr
```

APPENDIX C

USEFUL DEFINITIONS

C.1 4-VECTORS

A 4-vector is a mathematical object with four components. It differs from a Euclidean 3 vector in how its magnitude is determined. The energy and 3-momentum of a particle form a 4-vector $P^{\mu} = (\vec{p}), E)$, when squared gives the squared mass of the particle, $P \cdot P = E^2 - |\vec{p}|^2 = m^2$. For this work, we use the following four vectors in calculations:

$$\begin{aligned} P_{beam} &= (0, 0, P_{beam}, E_{beam}) \\ P_{target} &= (0, 0, 0, M_P) \\ P_P &= (Px_P, Py_P, Pz_P, E_P) \\ P_{\pi^+} &= (Px_{\pi^+}, Py_{\pi^+}, Pz_{\pi^+}, E_{\pi^+}) \\ P_{\pi^-} &= (Px_{\pi^-}, Py_{\pi^-}, Pz_{\pi^-}, E_{\pi^-}) \\ P_{\gamma} &= (Px_{\gamma}, Py_{\gamma}, Pz_{\gamma}, E_{\gamma}), \end{aligned} \tag{3.1.60}$$

where the four vector represents the target at rest.

C.2 KINEMATIC DEFINITIONS

We define the missing mass of the proton, $m_x(P)$ from the reaction $\gamma p \to pX$ as

$$(P_{beam} + P_{target} - P_P)^2 = P_X^2 = m_X^2. \tag{3.2.61}$$

The missing mass of the proton, π^+, and π^-, $m_x^2(P\pi^+\pi^-)$ is calculated as

$$(P_{beam} + P_{target} - P_P - P_{\pi^+} - P_{\pi^-})^2 = P_X^2 = m_X^2, \tag{3.2.62}$$

where for our reaction, the missing particle could have been a photon or neutral pion. The missing energy, $me(P\pi^+\pi^-)$, is defined as

$$E_{beam} + E_{target} - E_P - E_{\pi^+} - E_{\pi^-} = E_X. \tag{3.2.63}$$

The invariant mass of π^+ and π^-, is calculated as the square root of the Mandelstan s variable

$$s = IM^2(\pi^+\pi^-) = (P_{\pi^+} + P_{\pi^-})^2 = M_{\pi^+}^2 + M_{\pi^-}^2 + 2(E_{\pi^+}E_{\pi^-} - \vec{p}_{\pi^+} \cdot \vec{p}_{\pi^-}). \tag{3.2.64}$$

In this work, the invariant mass ranges from $4m_{\pi}^2 < s(\pi^+\pi^-) < m_{\eta}^2$.

APPENDIX D

FITS TO DATA

This Appendix shows the fits to the $m_x(P)$ and $m_x^2(P\pi^+\pi^-)$ distributions in order to perform the sideband subtraction and extraction of the number of photons per bin of $IM(\pi^+\pi^-)$.

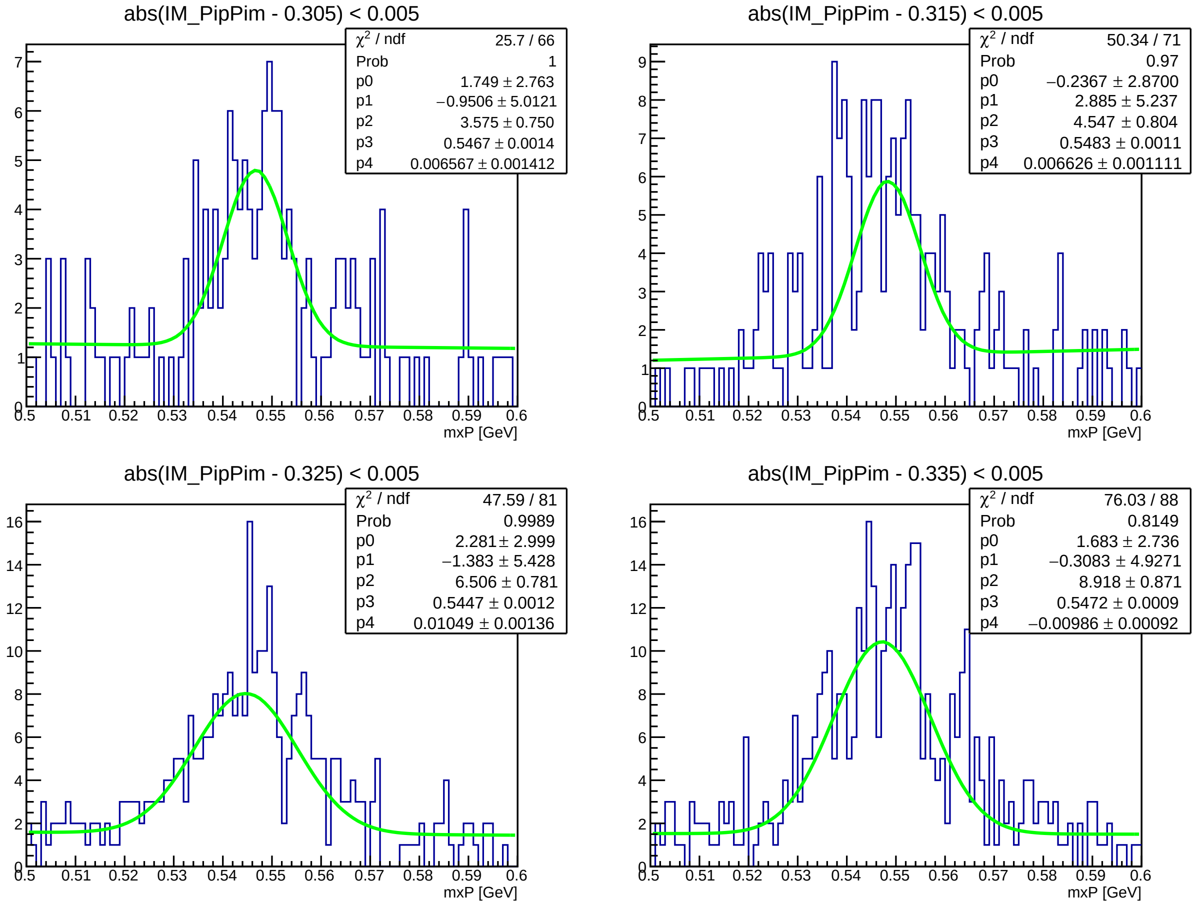

FIG. 62: Fit to η peak in the missing mass of the proton, $m_x(P)$. The invariant mass bin is specified at the top of each figure.

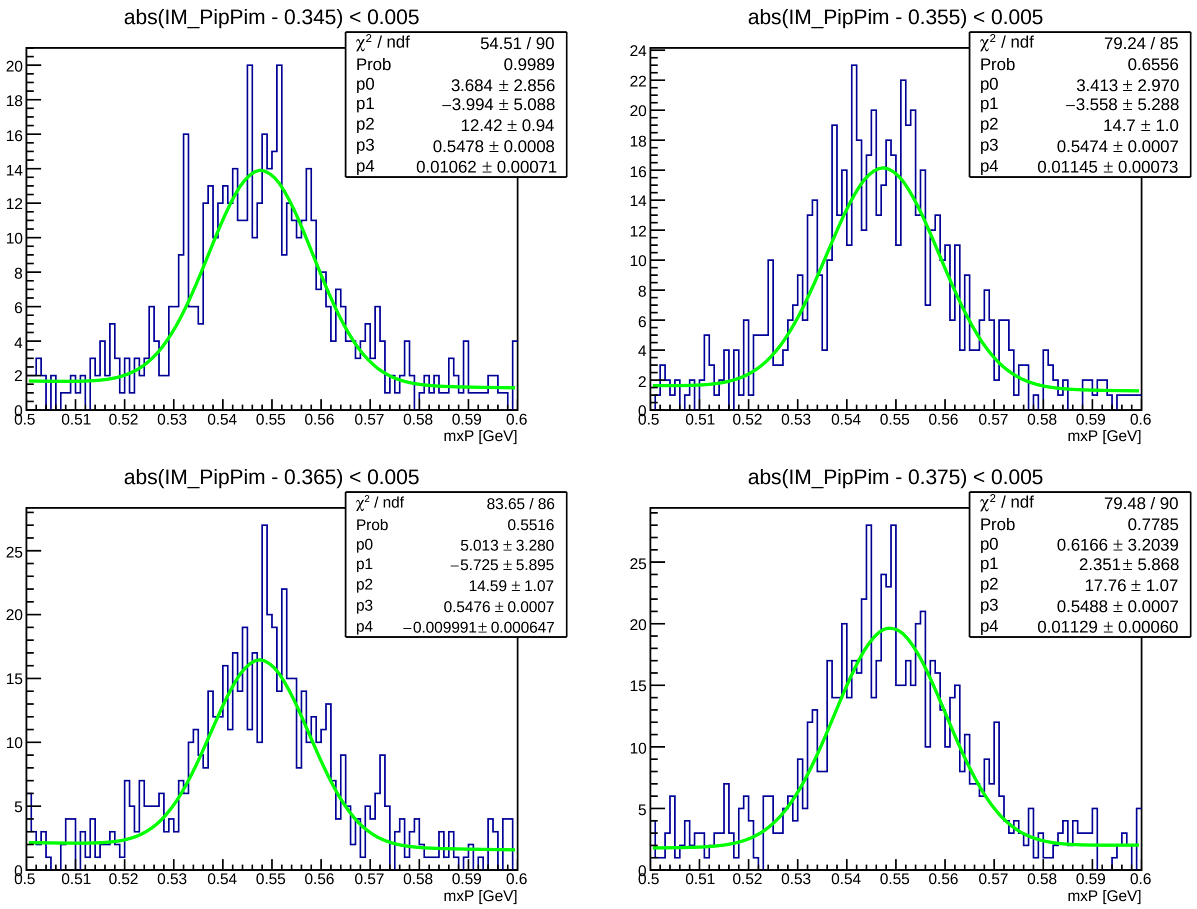

FIG. 63: Fit to η peak in the missing mass of the proton, $m_x(P)$. The invariant mass bin is specified at the top of each figure.

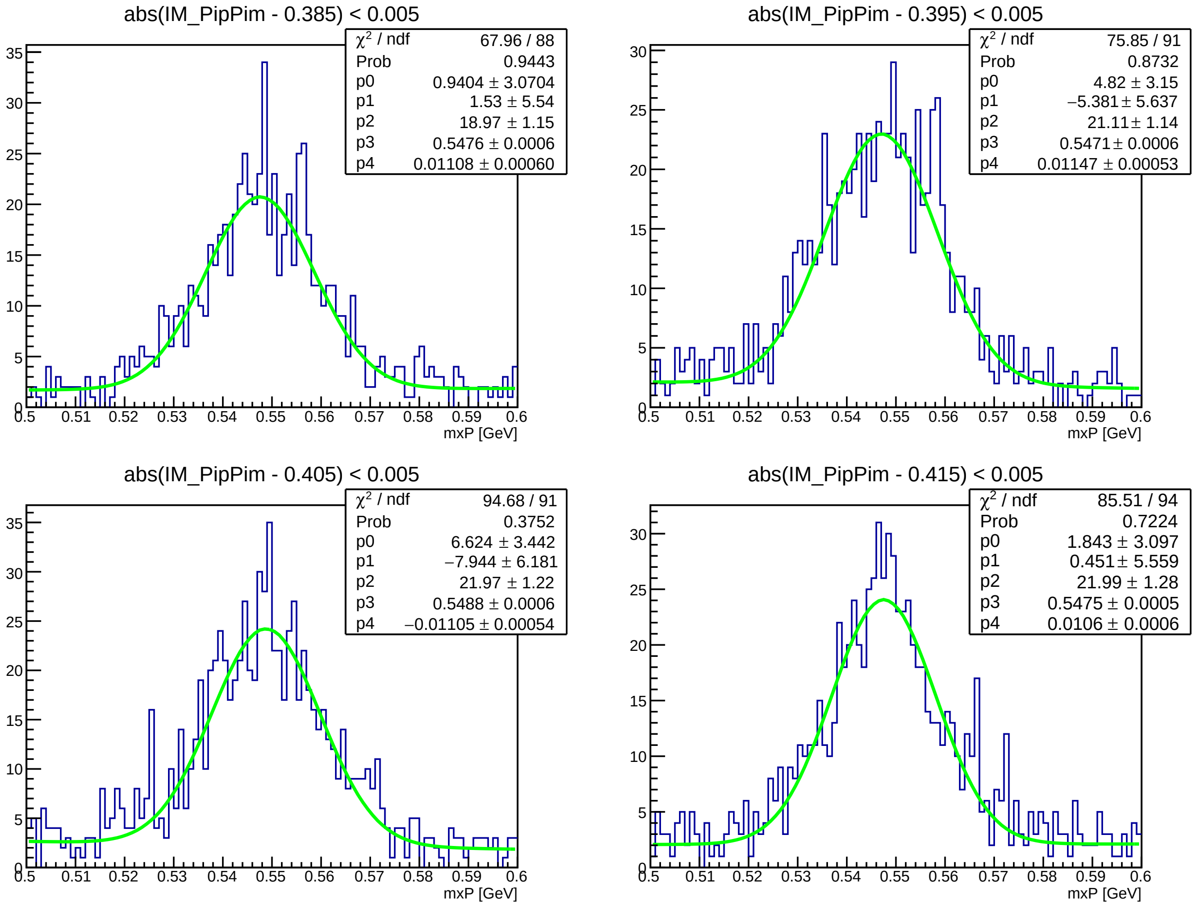

FIG. 64: Fit to η peak in the missing mass of the proton, $m_x(P)$. The invariant mass bin is specified at the top of each figure.

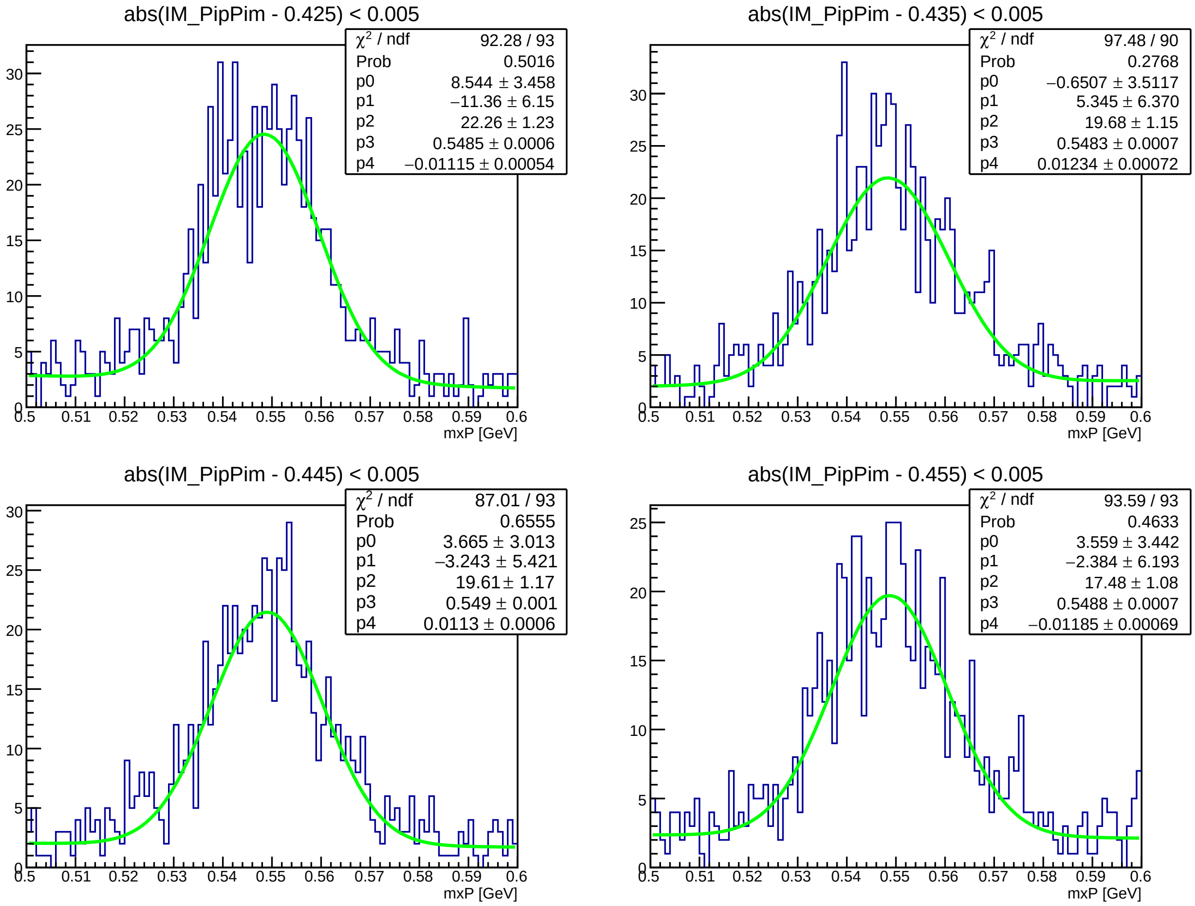

FIG. 65: Fit to η peak in the missing mass of the proton, $m_x(P)$. The invariant mass bin is specified at the top of each figure.

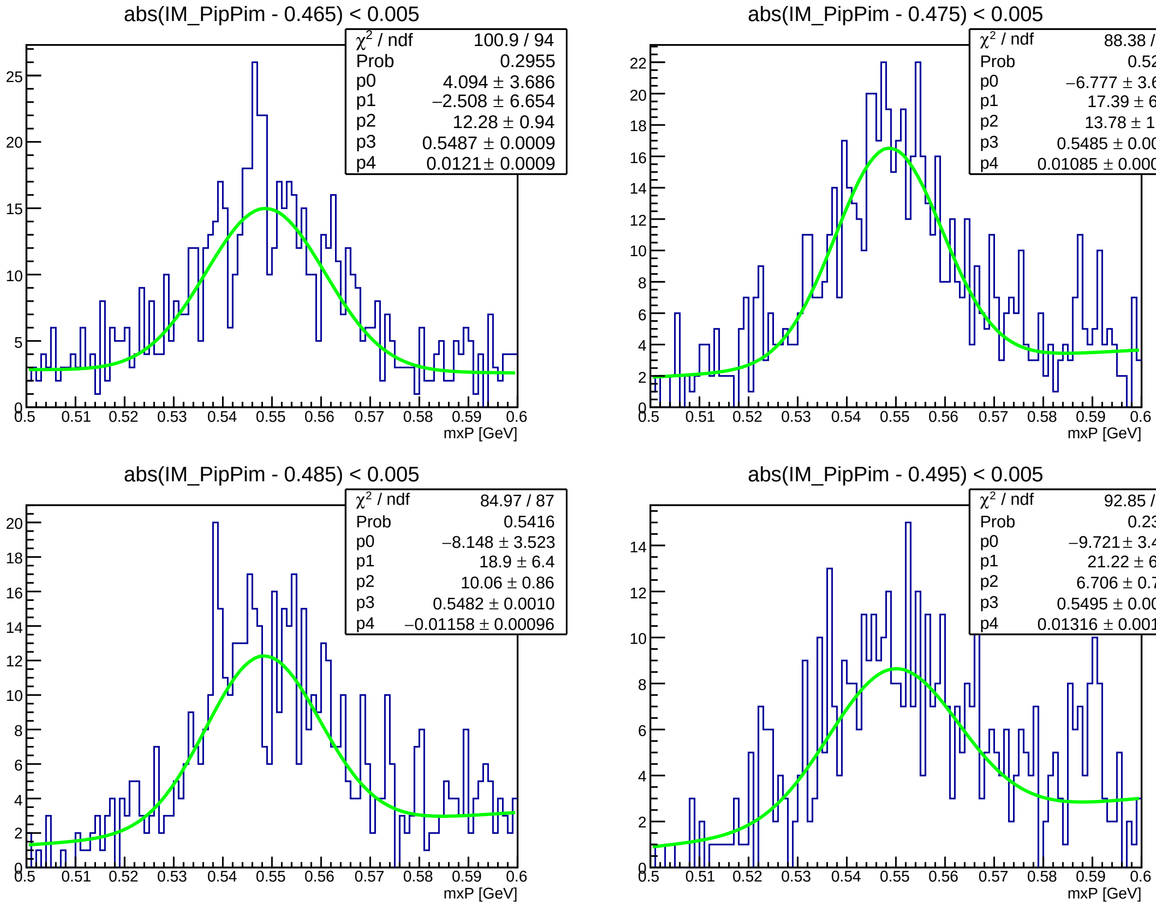

FIG. 66: Fit to η peak in the missing mass of the proton, $m_x(P)$. The invariant mass bin is specified at the top of each figure.

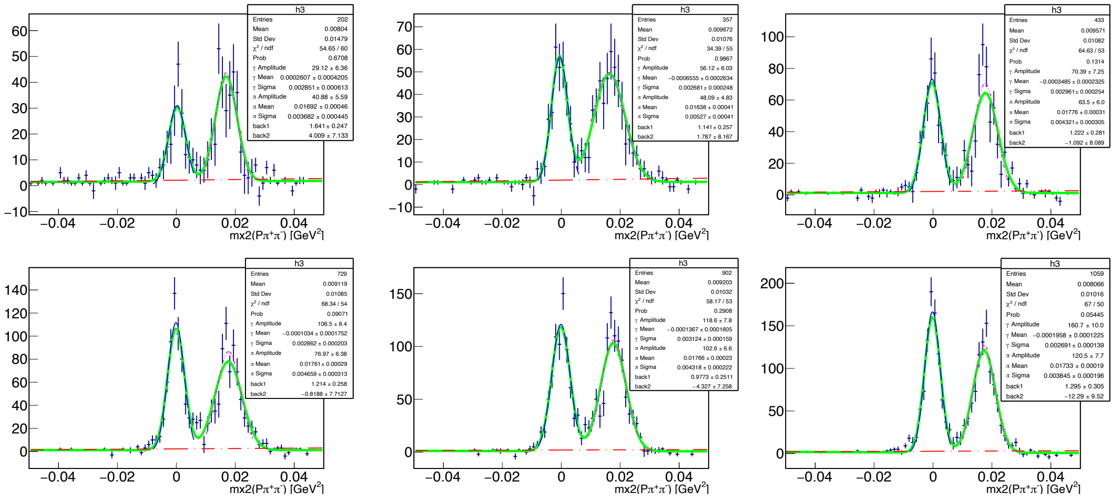

FIG. 67: Fit to $m_x^2(P\pi^+\pi^-)$ for $IM(\pi^+\pi^-) \in [0.305, 0.355]$. Red dash curve is linear background function. Green is total fit function: sum of 2 Gaussians and linear polynomial.

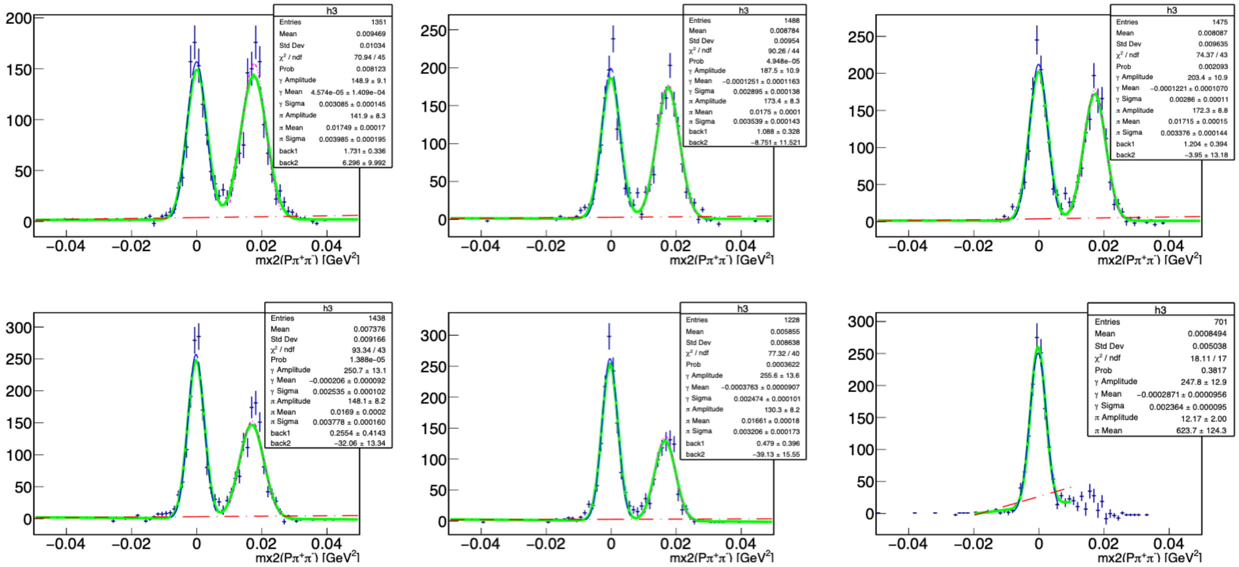

FIG. 68: Fit to $m_x^2(P\pi^+\pi^-)$ for $IM(\pi^+\pi^-) \in [0.365, 0.415]$. Red dash curve is linear background function. Green is total fit function: sum of 2 Gaussians and linear polynomial.

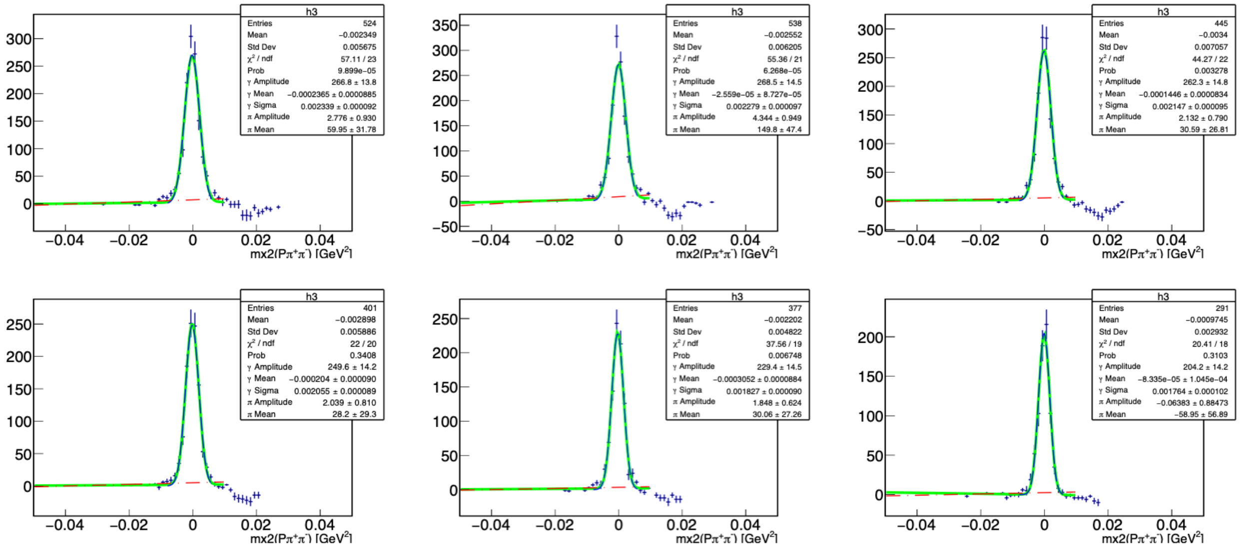

FIG. 69: Fit to $m_x^2(P\pi^+\pi^-)$ for $IM(\pi^+\pi^-) \in [0.425, 0.475]$. Red dash curve is linear background function. Green is total fit function: sum of 2 Gaussians and linear polynomial.

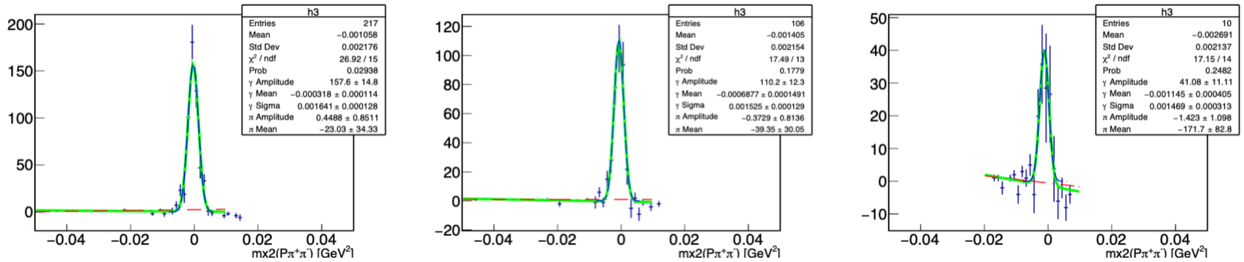

FIG. 70: Fit to $m_x^2(P\pi^+\pi^-)$ for $IM(\pi^+\pi^-) \in [0.485, 0.505]$. Red dash curve is linear background function. Green is total fit function: sum of Gaussian and linear polynomial.

VITA

Torri C. Jeske
Department of Physics
Old Dominion University
Norfolk, VA 23529

EDUCATION

Dec 2020 Ph.D., Physics, Old Dominion University

Aug 2016 M.S., Physics, Old Dominion University

May 2014 B.S., Indiana University-Purdue University, Indianapolis

EXPERIENCE

Dec 2016-2020 Graduate Research Assistant, Old Dominion University

Aug 2014-2016 Graduate Teaching Assistant, Old Dominion University

Aug 2015-2019 Jefferson Lab Graduate Student and Post-Doc Association President

PUBLICATIONS

Gurnev, P., Roark, T., Petrache, H., Sodt, A., and Bezrukov, S. (2017). Cation-Selective Channel Regulated by Anions According to Their Hofmeister Ranking. Angewandte Chemie International Edition. 56. 10.1002/anie.201611335.